UNIVERSITY OF CALIFORNIA, SAN DIEGO

Beyond Lithium:
Novel Electrode Materials for Room Temperature Na-ion Batteries

A dissertation submitted in partial satisfaction of the
requirements for the degree Doctor of Philosophy

in

NanoEngineering

by

Chuze Ma

Committee in charge:

Professor Ying Shirley Meng, Chair
Professor Eric E. Fullerton
Professor Jian Luo
Professor Michael J. Sailor
Professor Jan B. Talbot

2017

The Dissertation of Chuze Ma is approved, and it is acceptable in quality and form for publication on microfilm and electronically:

Chair

University of California, San Diego

2017

DEDICATION

To Jian Xiao and Fenglan Ma

TABLE OF CONTENTS

LIST OF FIGURES

LIST OF TABLES

ACKNOWLEDGEMENTS

First of all, I would like to thank my PhD advisor Dr. Ying Shirley Meng for her generous financial support and great mentoring. It was my honor to meet and work with her. I shall never forget her help and supports. I would also like to express my deepest gratitude to my other committee members: Dr. Eric E. Fullerton, Dr. Jian Luo, Dr. Michael J. Sailor, and Dr. Jan B. Talbot for their time and guidance.

Secondly, I would like to acknowledge my collaborators and co-authors in UCSD, Dr. Dae Hoe Lee, Dr. Jing Xu, Mrs. Judith Alvarado, and Dr. Haodong Liu, with whom I had many useful and stimulating discussions. I'm also grateful to all my group mates in Laboratory for Energy Storage and Conversion (LESC) who have helped and inspired me in many ways.

Finally, I would like to express my special thanks to my collaborators and co-authors, Dr. Mahalingam Balasubramanian at Argonne National Laboratory, Dr. Baihua Qu and Dr. Jim Yang Lee at National University of Singapore, and Dr. Clare P. Grey and Raphaele J. Clement at University of Cambridge for their invaluable help throughout the projects.

Chapter 4, in full, is a reprint of the material "$Na_2Ti_3O_7$ as an ultra-low voltage anode material for a Na-ion battery" as it appears in the Chemical Communications, J. Xu, C. Ma, M. Balasubramanian, Y. S. Meng, 2014, 50, 1256. The dissertation author was the co-primary investigator and author of this paper. All the experiment parts were performed by the author except for the computational part.

Chapter 5, in full, is a reprint of the material "Investigating the energy storage mechanism of SnS_2-rGO composite anode for advanced Na-ion batteries" as it appears in the Chemistry of Materials, C. Ma, J. Xu, J. Alvarado, B. Qu, J. Somerville, J. Y. Lee, Y. S. Meng, 2015, 27 (16), 563. The dissertation author was the primary investigator and author of this paper. All the experiment parts were performed by the author except for the Raman Spectra parts.

Chapter 6, in full, is a reprint of the material "Exploring Oxygen Activity in the High Energy P2-Type $Na_{0.78}Ni_{0.23}Mn_{0.69}O_2$ Cathode Material for Na-ion Batteries" as it appears in the Journal of the American Chemical Society, C. Ma, J. Alvarado, J. Xu, R. J. Clément, M. Kodur, W. Tong, C. P. Grey, Y. S. Meng, 2017, 139 (13), 4835. The dissertation author was the primary investigator and author of this paper. All the experiment parts were performed by the author except for the EIS, NMR and soft XAS parts.

Chapter 7, in full, is currently being prepared for submission for publication of the material "Improvement of the Cathode Electrolyte Interphase on P2-$Na_{2/3}Ni_{1/3}Mn_{2/3}O_2$ by Atomic Layer Deposition". The dissertation author was the co-primary investigator and author of this paper. The author conducted aluminium oxide ALD coating characterization and electrochemical test.

I would like to acknowledge the financial support from the National Science Foundation under Award Number 1057170 and Award Number 1608968.

For the last but not least, my deepest gratitude goes to my parents Jian Xiao and Fenglan Ma for their deep love and endless support.

VITA

2012 Bachelor of Science, University of Science and Technology Beijing

2014 Master of Science, University of California, San Diego

2017 Doctor of Philosophy, University of California, San Diego

PUBLICATIONS

1. D. Zhang, X. Xu, W. Wang, X. Zhang, H. Yang, Y. Wu, **C. Ma**, Y. Jiang, Electronic structures of new tunnel barrier spinel $MgAl_2O_4$: first-principles calculations, Rare Met., 2012, 31(2), 112

2. X. Xu, D. Zhang, **C. Ma**, Y. Jiang, Magnetic Properties of Boron-Doped Co_2FeSi : A First-Principles Study, IEEE, 2011, 47(10), 2912

3. J. Xu*****, **C. Ma***, M. Balasubramanian, Y. S. Meng, Understanding $Na_2Ti_3O_7$ as an ultra-low voltage anode material for a Na-ion battery, Chem. Comm., 2014, 50, 1256

4. B. Qu, **C. Ma**, G. Ji, C. Xu, J. Xu, Y. S. Meng, T. Wang, J. Y. Lee, Layered SnS_2-Reduced Graphene Oxide Composite – A High-Capacity, High-Rate, and Long-Cycle Life Sodium-Ion Battery Anode Material, Adv. Mater., 2014, 26(23), 3854

5. H. Liu, J. Xu, **C. Ma**, Y. S. Meng, A new O3-type layered oxide cathode with high energy/power density for rechargeable Na batteries, Chem. Commun., 2015, 51(22), 4693

6. Y. C. Lu, **C. Ma**, J. Alvarado, N. Dimov, Y. S. Meng, S. Okada, Improved Electrochemical Performance of Tin-sulfide Anodes for Sodium-ion Battery, J. Mater. Chem. A, 2015, 3, 16971

7. Y. C. Lu, **C. Ma**, J. Alvarado, T. Kidera, N. Dimov, Y. S. Meng, S. Okada, Electrochemical properties of tin oxide anodes for sodium-ion batteries, J. Power Sources, 2015, 284, 287

8. **C. Ma**, J. Xu, J. Alvarado, B. Qu, J. Somerville, J. Y. Lee, Y. S. Meng, Investigating the energy storage mechanism of SnS_2-rGO composite anode for advanced Na-Ion batteries, Chem. Mater., 2015, 27 (16), 5633

9. X. He, J. Wang, B. Qiu, E. Paillard, **C. Ma**, X. Cao, H. Liu, M. C. Stan, H. Liu, T. Gallash, Y. S. Meng, J. Li, Durable high-rate capability $Na_{0.44}MnO_2$ cathode material

for sodium-ion batteries, Nano Energy, 2016, 27, 602

10. R. J. Clément, J. Xu, D. Middlemiss, J. Alvarado, **C. Ma**, Y. S. Meng, C. P. Grey, Direct evidence for high Na^+ mobility and high voltage structural processes in P2-$Na_x[Li_yNi_zMn_{1-y-z}]O_2$ (x, y, z≤ 1) cathodes from solid-state NMR and DFT calculations, J. Mater. Chem. A, 2017, 5, 4129

11. **C. Ma**, J. Alvarado, J. Xu, R. J. Clément, M. Kodur, W. Tong, C. P. Grey, Y. S. Meng, Exploring Oxygen Activity in the High Energy P2-Type $Na_{0.78}Ni_{0.23}Mn_{0.69}O_2$ Cathode Material for Na-ion Batteries, J. Am. Chem. Soc., 2017, 139 (13), 4835

12. J. Alvarado*****, **C. Ma***, S. Wang, K. Nguyen, M. Kodur, Y. S. Meng, Improvement of the Cathode Electrolyte Interphase on P2-$Na_{2/3}Ni_{1/3}Mn_{2/3}O_2$ by Atomic Layer Deposition, (In preparation)

ABSTRACT OF THE DISSERTATION

Beyond Lithium:

Novel Electrode Materials for Room Temperature Na-ion Batteries

by

Chuze Ma

Doctor of Philosophy in NanoEngineering

University of California, San Diego, 2017

Professor Ying Shirley Meng, Chair

The Li-ion battery is one of the best rechargeable energy storage techniques due to its exceptional high energy density and long cycle life. It has dominated the portable electronic industry for the past 20 years and is going to be applied for large scale energy storage. However, concerns over limited lithium reserve and rising lithium costs have arisen, therefore Na-ion batteries are being considered as the alternative for grid storages.

In this thesis, $Na_2Ti_3O_7$ is first investigated as anode materials for Na-ion batteries. By carbon coating, the cyclability and coulombic efficiency are significantly enhanced for $Na_2Ti_3O_7$. The self-relaxation behaviour for fully intercalated phase, $Na_4Ti_3O_7$, is shown for the first time, which results from structural instability as suggested by first principles calculation. Another SnS_2-reduced Graphene Oxide (rGO) composite material is investigated as an advanced anode material for Na-ion batteries, which can deliver a reversible capacity of 630 mAh g^{-1} with negligible capacity loss and exhibits superb rate performance. The energy storage mechanism of it and the critical mechanistic role of rGO are revealed in detail.

On the cathode side, we introduce a novel layered oxide cathode material, $Na_{0.78}Ni_{0.23}Mn_{0.69}O_2$. This new compound provides remarkable rate and cycling performances owning to the elimination of the P2-O2 phase transition upon Na deintercalation. The first charge process yields an abnormally excess capacity which has yet to be observed in any other P2 layered oxides. It is proposed that part of the charge compensation mechanism during the first cycle takes place at the lattice oxygen site, resulting in a surface to bulk transition metal gradient. Atomic layer deposition (ALD) is known to improve the cycling performance, coulombic efficiency of batteries, and maintain electrode integrity for LIBs. Therefore we examine carefully the effect of Al_2O_3 ALD coating to P2 electrode materials. X-ray photoelectron spectroscopy (XPS) is used to elucidate the cathode electrolyte interphase (CEI) on ALD coated electrodes, which clearly reveal the effectiveness of the ALD coating. We believe that by optimizing and controlling the materials surface, Na layered oxide material with higher capacities can be designed.

Chapter 1. Motivation and Outline

Large-scale implementation of renewable energy requires development of inexpensive, efficient energy storage systems. Of the several technologies that are suitable for this purpose, pumped hydroelectric systems currently dominate, with compressed air being the second most utilized system. On the other hand, electrochemical energy storage (EES) technologies based on batteries are also being considered as a promising candidate given the rapid growth in the last two decades. EES technologies fulfill the demands for long cycle life, low cost and high round-trip efficiency, given their outstanding energy characteristics. The battery systems are well-suited for use at various circumstances because of their compact size, such as providing energy storage for local solar output, powering electric or hybrid electric vehicles, supplying energy for residential use, or enabling electrification of remote areas. With the adoption of EES technologies, the smart grid that includes a variety of energy generators and utilities will be realized. On-grid, batteries are utilized to store the excess energy generated from renewable sources and manage the intermittent outputs. The energy can then be used to power to the grid when consumption exceeds production, and/or be applied for off-peak utilization such as for EV charging. Li-ion batteries (LIBs), the most common type of rechargeable batteries found in almost all portable electronic devices, have been considered for grid-storage applications.[1]

Li-ion batteries possess several appealing attributes: lithium is the lightest metallic element and has the lowest redox potential ($E^0_{Li+ / Li}$ = -3.04 V versus standard hydrogen electrode), therefore enables cells with high voltage and high energy

density. Meanwhile, Li-ion has a small ionic radius, which is beneficial to diffuse in solids. LIBs are able to dominate the portable electronics market with their long cycle life and high rate capability.[2] In addition to the rapidly rising demands, they also become a prime candidate to power the next generation electric vehicles and plug-in electric vehicles. However, concerns over potentially issues with Li resources costs and availability have arisen. Most easily accessible global lithium reserves are in remote or in politically sensitive areas.[3] Even if extensive battery recycling programs were established, it is possible that recycling could not prevent this resource depletion in time.[2] Moreover, increasing lithium utilization will ultimately raise the price of lithium compounds, thereby making large-scale storage prohibitively expensive. The high cost and limited availability of the transition metals for cathode materials are also of concern, driving development towards more sustainable elements such as Fe and Mn.

The use of sodium instead of lithium for batteries could mitigate the feasible shortage of lithium in an economic way, owing to its high abundance and broad distribution of sodium sources. Sodium possesses suitable redox potential ($E^0_{Na+ / Na}$ = -2.71 V versus standard hydrogen electrode; only 0.3 V above that of lithium), thus rechargeable Na-ion batteries (NIBs) also hold much promise for energy storage applications. It has similar chemical approaches as lithium, including synthetic strategies, intercalation/alloying/conversion chemistries. Moreover, the characterization methods utilized in electrode materials for LIBs could be applied to develop electrode materials for NIBs more efficiently.[4] So far the development of NIBs is still at its early stage, therefore, my Ph. D research mainly focused on investigating the electrochemical mechanisms of the electrode materials for NIBs so as to design better materials.

The objectives of the first part of my thesis are to improve the capacity retention and rate capability of anode materials and unravel the fundamental mechanisms for their energy storage behaviors. The objectives of the second part of my thesis are to investigate the effects of transition metals and alkali ions on the phase stability and oxygen reaction upon cycling, as well as the surface enhancement of the materials. **Chapter 2** gives a general introduction of Na-ion batteries. **Chapter 3** briefly introduces advanced characterization tools I use in my research including synchrotron X-ray absorption and transmission electron microscopes. In **Chapter 4,** the capacity retention and rate capability of sodium titanates are improved and the fundamental reasons for their ultra low voltage and intrinsic problems are unraveled. **Chapter 5** introduces a great capacity, high rate, long cycle life SnS_2-reduced graphene oxide composite anode and its energy storage mechanisms are thoroughly studied. **Chapter 6** discusses the critical role of Na concentration in P2-$Na_{0.78}Ni_{0.23}Mn_{0.69}O_2$ to maintain the structural stability during cycling, and proposes the reaction of oxygen atoms for charge compensation. **Chapter 7** explains the improvement of the cathode electrolyte interphase on P2-$Na_{2/3}Ni_{1/3}Mn_{2/3}O_2$ by atomic layer deposition. **Chapter 8** summarizes the overall work and my ideas for the future research.

Chapter 2. Introduction of Sodium Ion Batteries

2.1. Na-ion Batteries (NIBs)

Na-based batteries are not new. Back to the 1970s, Na-ion and Li-ion batteries were investigated in parallel.[5,6] The investigation of Na-ion batteries significantly decreased after the successful commercialization of Li-ion batteries in the 1990s. Na-ion batteries have a very similar working principle as the Li-ion batteries. As shown in Figure 2.1, each electrochemical cell is basically composed of three main components: a positive electrode, a negative electrode, and a membrane separator which contains electrolyte. Active materials that allow Na-ions to be reversibly inserted or extracted are casted on the aluminum foil to form the electrodes. The electrolyte and separator are conductive to ions but resistant to electrons, allowing Na-ions but not electrons to pass between the two electrodes during the electrochemical cycling.

Recently, research interest in Na-ion batteries operated at room-temperature is renewed because of the abundance and low cost of Na. As the demands for and sizes of batteries have increased, the interest in NIBs has resurged particularly for grid-scale ESSs. As shown in Figure 2.2, a remarkable number of new materials have been introduced and evaluated as electrode materials for NIBs in the last few years. Similar to LIB chemistry, layered and polyanionic compounds have been extensively investigated as cathode materials, and carbon based materials, metal oxide compounds, and metals have been studied as anode materials (Figure 2.2 (b),(c)). Prussian blue and organic materials have also been recently examined as electrode materials for NIBs. As displayed in Figure 2.2, electrode materials with various redox potentials and capacities were discovered in only a

few years of research, and some of these materials are already comparable to those used in LIBs.

2.2. Anode Materials for NIBs

Despite the high specific capacity and low voltage potential, the formation of dendrites and the safety issues related to sodium metal currently prevent its use as a negative electrode for commercial applications. Therefore, successful development of safe and efficient anode materials is important for Na-ion batteries.

2.2.1. Carbons

Unless specific electrolyte is used, Na-ions do not intercalate in graphite, which is the most commonly used negative electrode in commercialized Li-ion batteries.[7,8] As the Na-ions has 50% larger ionic radius than the Li-ions, they are too big to intercalate into the carbon layers. Alternative carbons such as the hard carbons, are wildly studied given their low redox plateau and high reversible capacities ($300 mAhg^{-1}$).[9] Hard carbons are normally prepared by pyrolysis reactions of carbohydrate compounds, resulting in its amorphous nature and expanded carbon layers. The redox potential of Na insertion into hard carbon is close to 0.1 V comparing to the Na/Na^{+} redox potential, which indicates that there is very little charge transfer between carbon and sodium. A mechanism is therefore proposed that instead of intercalating into the graphitic sheets, Na-ions form clusters that fill the porous sites in the disordered carbon, instead of intercalating into the graphitic sheets. As the redox potential of hard carbons is very close to the sodium plating potential, it raises safety issues if operated at high current density and/or high

depth of discharge. Recently, it was shown expanded graphite could reversibly store and release Na-ions, with the d-spacing of the carbon layer largely influencing the reversible capacity.[10] The voltage profile of expanded graphite is a sloping curve from 1.5 V to 0 V. The higher voltage compared to hard carbon increases the safety but it sacrifice energy density.

2.2.2. Low Potential Transition-Metal Oxides and Phosphates

Transition metal oxides are of great interest to be explored as anode materials. The intercalation mechanism of Na-ions into the structure allows for high volumetric energy density as well as good safety features. NASICON-type $NaTi_2(PO_4)_3$ was first reported to have a redox plateau at 2.1 V, indicating a two-phase reaction mechanism during Na intercalation.[11] It exhibits high reversible capacity of 120 $mAhg^{-1}$ when tested in both non-aqueous and aqueous electrolytes, with a lower polarization observed in the latter. The obtained capacity is as high as 90% of the theoretical capacity, while the better electrochemical performance in aqueous electrolyte relies on its lower impedance and viscosity. The redox potential for Na-ion intercalation is the same with the lower limit of the electrochemical stability window of the aqueous Na_2SO_4 electrolyte, which makes $NaTi_2(PO_4)_3$ an attractive negative electrode for aqueous NIBs.[12] Another material, $Na_2Ti_3O_7$ exhibits an ultra low voltage plateau at around 0.3 V for the reversible storage of two sodium atoms.[13] The theoretical capacity of 177 $mAhg^{-1}$ could be achieved; however, up to 30% of super P carbon black additive and a slow cycling rate (C/25) are necessary. The large amount of carbon additive decreases the energy density and causes

large irreversible capacity, which is of the same order of magnitude as the reversible capacity observed at the first cycle.

2.2.3. Alloys

The potentials for several different alloy reactions have been predicted through computational study which shows promising results.[14] Meanwhile, these alloy reactions provide high specific capacity since multi-electron transfer is involved during the reactions. However, volume expansion of the alloys is the main issue, which causes quick capacity degradation for longer cycles. Tin metal is of great interests as it can alloy with Na-ions at an average voltage of 0.3 V and provide a high theoretical capacity of 790 mAh g^{-1}. The computational study has been proven by experimental results; composite electrodes of tin powder with a polyacrylate binder show a reversible capacity of 500 $mAhg^{-1}$ over 20 cycles at a slow cycling rate.[15] *In situ* techniques show that the Sn-Na alloying mechanism is dependent on the physical form of the anode: Sn nano-particles were able to accommodate the volume increase without cracking by forming amorphous/nanocrystalline phases, according to the *in situ* TEM results;[16] whereas Sn-Na alloy foils tend to show much higher crystallinity according to the *in situ* XRD study.[17] In both cases, kinetic effects are predominant and prevent the formation of the thermodynamically stable phases present in the Na-Sn phase diagram. Besides tin, antimony is another metal that can alloy with Na at low potential. Microcrystalline antimony exhibits a large reversible capacity of $600mAhg^{-1}$ over 160 cycles at a rate of C/10 with an average voltage of 0.8 V.[18] Moreover, amorphous phosphorus[19] demonstrates an extremely high capacity of $1500mAhg^{-1}$ when alloying with Na-ions at

0.6 V. As the large volume expansion causes cracks and strains for the alloy anodes during cycling, the passivation of the anode/electrolyte interphase is crucial. By adding fluorinated ethylene carbonate (FEC) to the electrolytes, the cycling performance of alloy anodes can be greatly enhanced.[15,18,19]

2.3. Cathode materials for NIBs

A large number of compounds are being studied as possible cathode materials for Na-ion batteries, most of which can be grouped into either layered metal oxides or polyanion compounds. Each family has its own advantages and disadvantages for their real application in energy storage systems.

2.3.1. Layered Metal Oxides

Layered oxides are composed of alternate Na layers and transition-metal (TM) layers in the oxygen framework. They can be easily synthesized in air with solid-state methods. O3-phase and P2-phase are the most studied layered oxides for NIBs cathode materials. As shown in Figure 2.3, the oxygen layers in the O3 phase pack closely in an ABCABC pattern, in which Na-ions and TM ions are located in the octahedral sites. On the other hand, the oxygen layers in P2-phase are stacked in the ABBA manner, so that the Na-ions locate in the trigonal prismatic sites. Na-ions can reversibly intercalate/deintercalate from the P2/O3 structure, but with lower activation energy for the P2 phase.

Na_xCoO_2 has been considered as the cathode of NIBs due to the success of $LiCoO_2$, however, Na_xCoO_2 shows inferior electrochemical performance due to poor

kinetics and multiple phase transformations.[20,21] Na_xMnO_2 is more competitive with higher theoretical capacity and lower cost of Mn. Meanwhile, the O2 phase and birnessite phase of Na_xMnO_2 also exhibit electrochemical activities for NIBs.[22] Despite providing high capacities, Na_xMnO_2 materials suffer from poor cycling performance because of the structural degradation induced by dislocations and defects.[23–25] Although $LiFeO_2$ is not active for LIBs, $NaFeO_2$ could provide reversible capacity in NIBs with highly active $Fe^{3+/4+}$ redox.[26–28]

Based on the various behaviors of single-TM oxides, such as the good ionic diffusivity of Na_xCoO_2, the high specific capacity of Na_xMnO_2, and the high redox potential of $NaFeO_2$; layered oxides with combinations of several different TMs are designed so as to improve the overall performance of the materials.. O3-$Na[Ni_{0.5}Mn_{0.5}]O_2$ can be regarded as a good example, in which Ni^{2+} ions are active and Mn^{4+} ions are inactive.[29] When cycled between 2.2-3.8 V, the material delivers a capacity of 125 mAh g^{-1}, with 75% of the capacity maintained at the 50^{th} cycle. If the cut-off potential is increased to 4.5 V, its capacity can further increase to 185 mAh g^{-1}. However, at the higher voltage, significant inter-slab expansion and phase transitions occur that the cycling performance is severely harmed.[30, 31] Another important multi-metal oxide, P2-$Na_{2/3}[Fe_{1/2}Mn_{1/2}]O_2$,first reported by Komaba's group, has attracted wide attention as it provides large reversible capacity but only consists earth abundant and environmental friendly elements.[32] Both Mn^{3+} / Mn^{4+} and Fe^{3+} / Fe^{4+} redox couples are highly active in this compound, therefore it can deliver a reversible capacity up to 190 mAh g^{-1} when cycled between 1.5–4.3 V. More surprisingly, up to 70% of the capacity can be achieved at 1 C without any further optimization to the active material. However, 20% capacity

fading was observed up to 30 cycles, indicating the cycling performance need to be improved. According to the XRD results, a series of complicated phase transitions from P2 phase ($P6_3/mmc$, pristine) to OP4 phase ($P6_3$, fully charged) to P2 phase ($P6_3/mmc$, 3.4–2.0 V) then to P'2 phase (Cmcm, 2.0–1.5 V) occur during the electrochemical cycling.[33] The cycling performance can be improved by lower the cut-off voltage to 4.0 V to avoid OP4 phase, but the reversible capacity is reduced.

To stabilize the structure, Li doping has been applied to P2-type layered oxides. The detrimental P2–O2 phase transformation can be effectively inhibited and the hexagonal P2 structure can be well maintained even the electrode is charged to 4.4 V.[34,35] As a result, the materials show enhanced rate and cycling performances. For instance, P2-$Na_{0.80}[Li_{0.12}Ni_{0.22}Mn_{0.66}]O_2$ deliver a reversible capacity of 118 mAh g^{-1} between 2.0–4.4 V with a capacity retention of 91% after 50 cycles.[35] In addition, O3-type layered oxides that contain Li can be obtained by Li/Na-exchange of Li-rich layered oxides through electrochemical methods, which demonstrate extremely high capacity.[36,37]

2.3.2. Polyanion Compounds

Due to the strong inductive effect of the anions, polyanion compounds have outstanding structural stability and therefore are being widely studied as cathode materials for NIBs. They are commonly characterized as high operating potentials and excellent cycling performances. However, poor electronic conductivity is a common issue for this group of material. Polyanion compounds exhibits high structure diversity which includes phosphates ($NaFePO_4$ and $Na_3V_2(PO_4)_3$), pyrophosphates ($Na_2MP_2O_7$ and $Na_4M_3(PO_4)_2P_2O_7$), fluorophosphates (Na_2MPO_4F, $Na_3(VO_x)_2(PO_4)_2F_{3-2x}$) (M = Fe, Co,

Mn), and sulphates ($Na_2Fe_2(SO_4)_3$, $Na_2Fe(SO_4)_2 \cdot 2H_2O$). In this thesis, $NaFePO_4$ and $Na_3V_2(PO_4)_3$ are briefly introduced.

In the olivine $NaFePO_4$ crystal, metal atoms (Na and Fe) occupy half of the octahedral sites and the P atoms occupy one-eighth of the tetrahedral sites of a hexagonal-close-packed oxygen array. It is not the most thermodynamically stable phase of $NaFePO_4$, which increases a lot of difficulties to obtain pure phase olivine $NaFePO_4$ experimentally.[38] Olivine $NaFePO_4$ is an attractive cathode as it shows a high theoretical capacity of 154 mAh g^{-1} and a high average voltage of 2.9 V based on the $Fe^{2+/3+}$ redox couple.[39] However, because of the large difference between the desodiated $FePO_4$ structure and the $NaFePO_4$ structure, the charge/discharge process for this material is not reversible. Two voltage plateaus could be observed during the charge, which correspond to the solid-solution reaction and two-phase reaction respectively, however, only one plateau could be found during the discharge, which results from the co-existence of three phases.[39] As mentioned above, $NaFePO_4$ also suffers from poor electron conductivity; therefore additional carbon should be used to optimize the performance. After all, the practical capacity of olivine $NaFePO_4$ is much lower than its theoretical capacity because of these drawbacks.[40] The electrochemical performance of $NaFePO_4$ can be enhanced by carbon coating and reducing particle size.

NASICON $Na_3V_2(PO_4)_3$ is another widely studied polyanion compound. In the $Na_3V_2(PO_4)_3$ crystal, corner-sharing PO_4 tetrahedra and VO_6 octahedra create a three-dimensional $[V_2P_3O_{12}]$ skeleton and Na-ions occupy two different Na(1) and Na(2) interstitial sites.[41] The open structure allows fast Na-ion diffusion through the 3D diffusion channels, but the PO_4 anion reduces the electronic conductivity of the material.

$Na_3V_2(PO_4)_3$ has a high voltage plateau at 3.4 V based on the V^{3+} / V^{4+} redox reaction. However, only two-thirds of the Na-ions can be extracted from the structure when used as cathode, resulting in a low theoretical capacity of 117 mAh g^{-1}.[41] $Na_3V_2(PO_4)_3$ has been studied by Plashnitsa et al. in a symmetric cell with an ionic-liquid electrolyte, but the electrochemical properties are unsatisfactory.[42] The addition of carbon to the material can significantly enhance the electrochemical performance. Various methods such as carbon coating or embedding were applied to increase the electronic conductive of the active material.[43–46] The composite electrode of $Na_3V_2(PO_4)_3$ dispersed on acetylene carbon nano-sphere exhibit reversible capacities of 117.5 mAh g^{-1} at 0.5 C and 97 mAh g^{-1} at 5 C, with excellent capacity retention of 96.4% for more than 200 cycles.[47] The electrochemical performance of $Na_3V_2(PO_4)_3$ can also be enhanced by doping. For instance, Fe doping has been demonstrated as an effective method to improve the electrochemical performance by increasing the valence state of vanadium.[48]

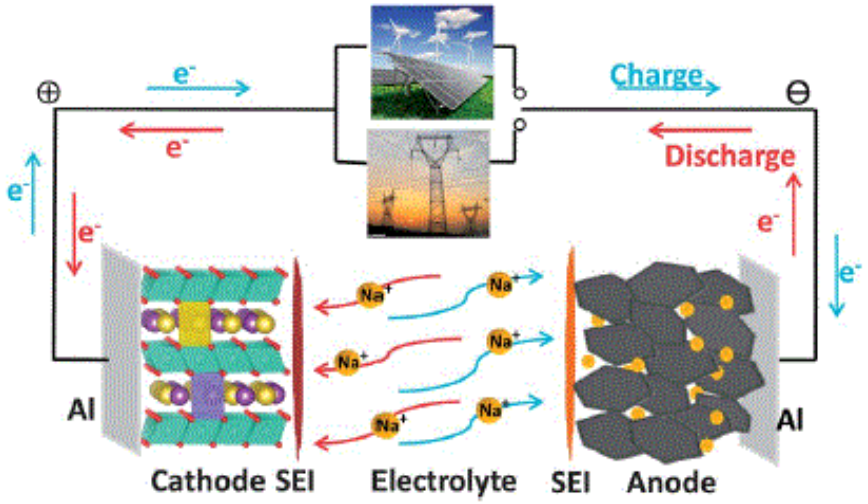

Figure 2.1. X-ray absorption spectroscopy spectra including XANES and EXAFS regions. Inset schemes illustrate the origins of the oscillation in the spectra.[49]

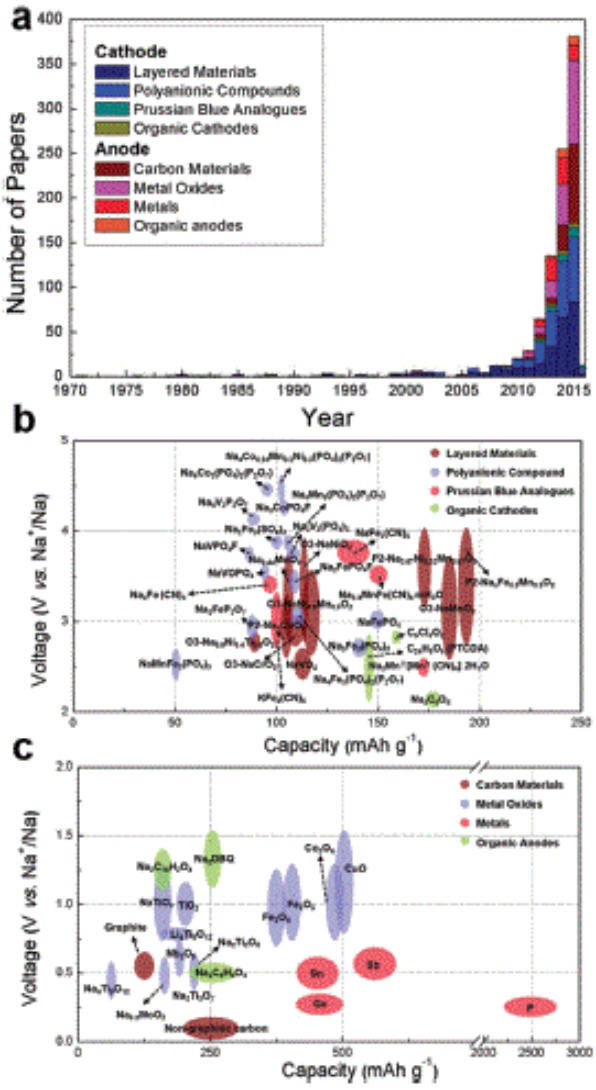

Figure 2.2. (a) The number of publications on NIB electrode materials over time. Voltage–capacity plots of representative: (b) positive and (c) negative electrode materials for NIBs.[50]

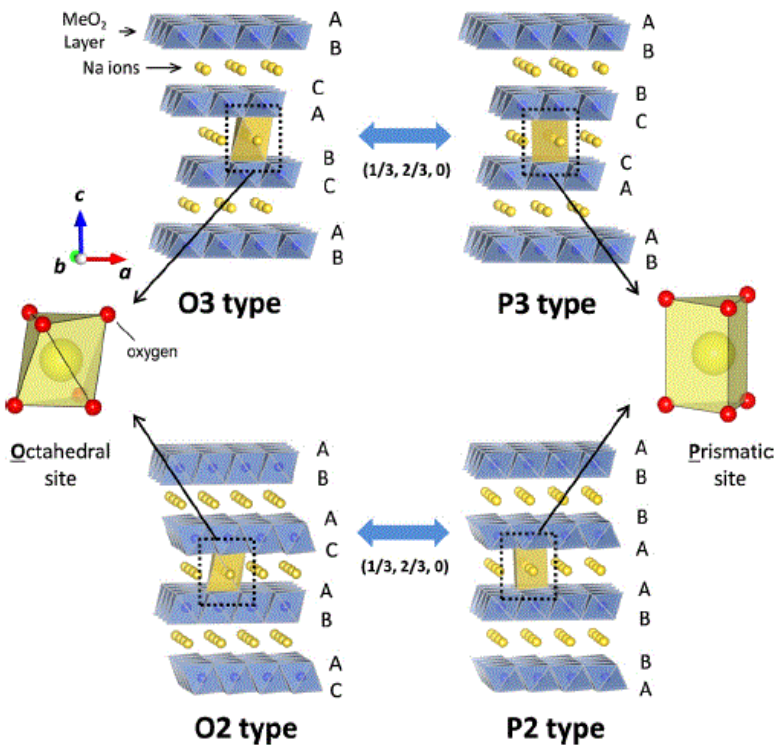

Figure 2.3. The classification of Na–Me–O layered materials with the sheets of edge-sharing MeO_6 octahedra and phase transition processes induced by sodium extraction.[51]

Chapter 3. Advanced Characterization Tools

3.1. X-ray Absorption Spectroscopy (XAS)

3.1.1. *In situ* XAS

The element-specific nature and high sensitivity to the local chemical environment of XAS technique make it an ideal tool to study the electronic structural properties and inter-atomic environment. The working principle is straightforward: when the X-ray hits a sample, the oscillating electric field of the electromagnetic radiation interacts with the electrons bound in an atom. The radiation will either be scattered by these electrons or part of its energy will be absorbed to excite the electrons. As a result, a narrow parallel monochromatic X-ray beam of intensity I_0 passing through a sample of thickness *x* will get a reduced intensity I according to the equation 3.1:

$$\ln\left(\frac{I_o}{I}\right) = \mu x \qquad \text{(eq. 3.1)}$$

Here μ is the linear absorption coefficient, which depends on the types of elements and the density of the material. The absorption by the electrons increases drastically at the characteristic energy for certain element and gives rise to an absorption edge. It only happens when the energy of the incident photons is just sufficient to cause excitation of a core electron of the absorbing atom to a continuum state. Meanwhile, a photoelectron is generated during this process. For certain element, it could possess various absorption edges corresponding to the different binding energies of electrons in the 1s ($2S_{1/2}$), 2s ($2S_{1/2}$), 2p ($2P_{1/2}$), 2p ($2P_{3/2}$) orbitals (states), which are labeled as K, L_I, L_{II}, L_{III} edges.

When the photoelectron leaves the absorbing atom, its wave is backscattered by the neighboring atoms. The photoelectron wave and the backscattered wave then generate constructive and destructive interference, resulting in maxima and minima after the edge. Figure 3.1 shows an example of a complete X-ray absorption spectroscopy spectrum. It is generally divided into 4 sections: (1) pre-edge ($E < E_0$); (2) X-ray absorption near edge structure (XANES) where the energy of the incident X-ray beam is within 10eV of the absorption edge; (3) near edge X-ray absorption fine structure (NEXAFS), which is in the region between 10 eV up to 50 eV above the edge; and (4) extended X-ray absorption fine structure (EXAFS), which locates from 50 eV to 1000 eV above the edge.

The pre-edge region contains information about ligand-field, centrosymmetry or spin-states, which is mainly due to the electron transitions from the core level to the higher unfilled or half-filled orbitals (e.g., $p \rightarrow d$). In the XANES region, transitions of core electrons to unoccupied higher energy states occur, which is the most likely absorption transition; therefore a large absorption edge is observed at the characteristic energies. In the NEXAFS region, the ejected photoelectrons have low kinetic energy since $E - E_0$ is small, therefore the multiple scattering by the atoms at first and even higher coordinating shells is very strong. In the EXAFS region, since $E - E_0$ is large, the photoelectrons have high kinetic energy and thus allow single scattering by the nearest neighboring atoms.

In situ XAS experiments could be conducted with the customized coin cells as shown in Figure 3.2. The X-ray could go through the Cirlex film window in the middle of the working cells and therefore characterize the materials during the electrochemical reaction process. In this thesis, *in situ* XAS has been adopted to the study of multiple

electrode materials, providing crucial information about the electronic structure and local chemical environment.

3.1.2. Soft XAS (sXAS)

Soft XAS (sXAS) is capable of probing chemical environment with excellent surface depth sensitivity by tuning the signal acquisition mode. Specifically, sXAS data can be collected simultaneously using three detection modes (Figure 3.3): (1) Auger electron yield (AEY), (2) Total electron yield (TEY), and (3) Fluorescence yield (FY). Electron yield modes vary in penetration depth and are extremely surface sensitive: TEY mode has a probing depth of 2-5 nm, whilst AEY has a probing depth of 1-2 nm. The FY mode probes the bulk of the material up to a depth of about 50 nm.[52] sXAS data were acquired under ultrahigh vacuum (10^{-9} Torr) in a single load at room temperature in total electron yield (TEY) mode via the drain current method, in Auger electron yield (AEY) mode using a cylindrical mirror analyzer, and in fluorescence yield (FY) mode using silicon photodiodes. Given its impressive capabilities, this characterization technique has been applied to investigate charge compensation mechanisms in LIB cathode materials, proving particularly useful in the exploration of redox reaction mechanisms involving oxygen anions in relation to those involving TM ions.[52,53]

X-ray absorption peaks corresponding to the metal L3- and L2-edges are relatively intense because the 2p-3d transition is electric dipole-allowed. In addition, these peaks are very sensitive to oxidation state, spin state, and bond covalence. The most salient electronic structure can be qualitatively obtained by deconvoluting the L3-edge into high-energy ($L3_{high}$) and low-energy ($L3_{low}$) features. It is noted that the ratio

between the $L3_{high}$ and $L3_{low}$ integrated peak intensities is in a positive relationship with the TM oxidation state.[54]

3.2. Transmission Electron Microscopy (TEM)

Transmission Electron Microscopy (TEM) can provide critical information about the crystal structure, chemical composition and electronic bonding structure of the materials, and is therefore being widely adopted by materials scientists for their research. In a TEM: a beam of electrons is emitted from an electron gun, accelerated by a high voltage electric field (200-300kV), and refined/bended by multiple electromagnetic lenses that focus the beam. Then the beam of electrons is passed through an ultra-thin sample (100 nm thickness) and interacts with the atoms in there. At last, the transmitted electron beam is magnified, and detected by the fluorescent screen or digital CCD cameras to form an image.

Optical microscopes have limited resolution because of the wavelength of visible light. In 1928, it is found by applying de Broglie's hypothesis of wave-matter duality, electrons would have a much smaller wavelength than visible light and could be used to enable resolving power capable of distinguishing atoms. The wavelength of an electron can be calculated with relativistic corrections by Equation 3.2. For an electron accelerated by a 200 kV field, its de Broglie wavelength is 2.5 picometers providing enough resolving power for atomic bonds.

$$\lambda_e \approx \frac{h}{\sqrt{2m_e \mathrm{E}(1+\frac{\mathrm{E}}{2m_e c^2})}} \qquad \text{(eq. 3.2)}$$

The transmission electron microscope is a highly complex instrument composed of multiple components. Generally, it includes (1) a column of vacuum system for which the electrons can travel; (2) an electron source; (3) a series of electromagnetic lenses to refine, shape, and magnify the electron image; and finally (4) detectors to capture the image.

The pressure in the electron beam column should be kept lower than 10^{-7} Torr in order to create an environment with minimal electron gas collisions and to prevent electrical arcs. The electron source consists of several components to produce a beam of highly energized electrons. Electrons can be generated through two types of mechanism, thermionic emission and field emission. In thermionic emission, a filament with a high melting point and low work function such as tungsten or lanthanum hexaboride is heated to a temperature where the thermal energy of the electrons is higher than its work function leading to emission. Then, the emitted electrons are converged by a negatively charged Wehnelt Cylinder, at the expense of fewer electrons emitted, and finally accelerated to a positively charged anode. In field emission, a strong electric field of 109 V/m is used to extract electrons from a metal filament and then accelerated further to the full potential. Field emission electrons produce a more intense electron beam, but require higher vacuum columns on the order of 10^{-10} Torr. After the electrons are generated and accelerated under a high applied voltage, they are focused by several electromagnetic lenses that act in the same principle as an optical convex lens. There are two condenser lenses right under the electron source which can shape and bend the electron beam before it interacts with the sample. Then the objective lens is put under the sample to create an inverted image, which is then magnified by an intermediate lens and two projector lenses.

Finally the transmitted beam hit the detector to form an image. Figure 3.4 shows a schematic of the TEM column with all the components.

In this thesis, the high resolution TEM coupled with selected area electron diffraction was applied to study the morphology and structures of the battery electrode materials. Some of the characterization and data analysis were also carried out in scanning transmission electron microscopy (STEM) mode, and electron energy loss spectroscopy (EELS) was used in STEM mode as well.

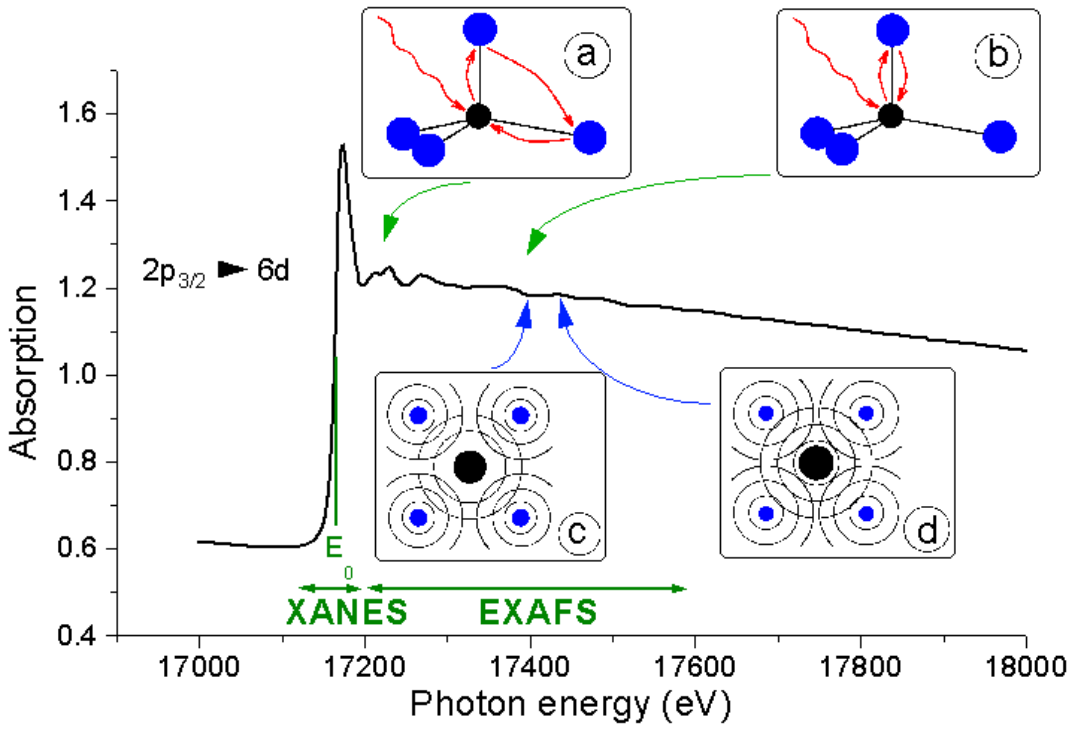

Figure 3.1. X-ray absorption spectroscopy spectra including XANES and EXAFS regions. Inset schemes illustrate the origins of the oscillation in the spectra.

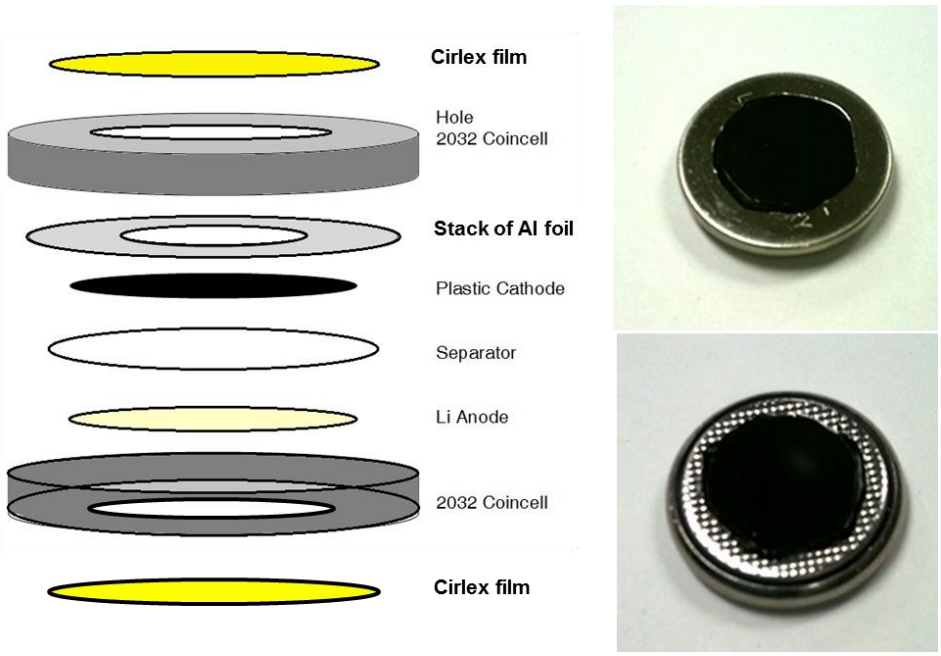

Figure 3.2. Customized coin cell design for *in situ* XAS measurement.

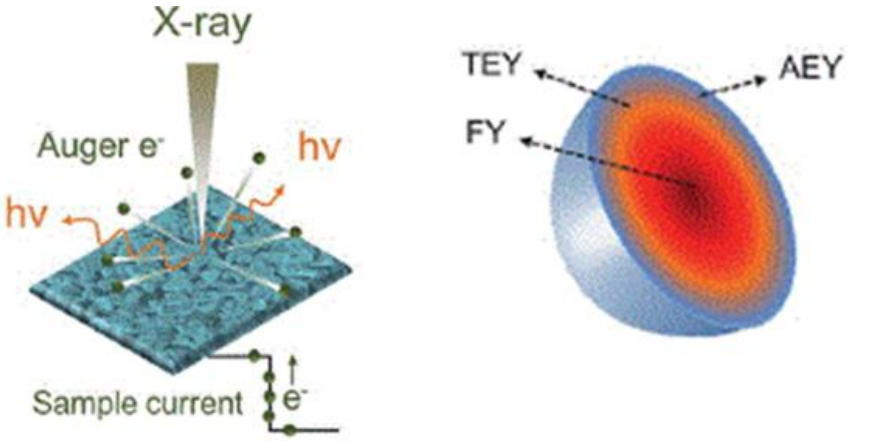

Figure 3.3. Schematic illustration of XAS data acquisition and the corresponding probing depth using three detection modes.

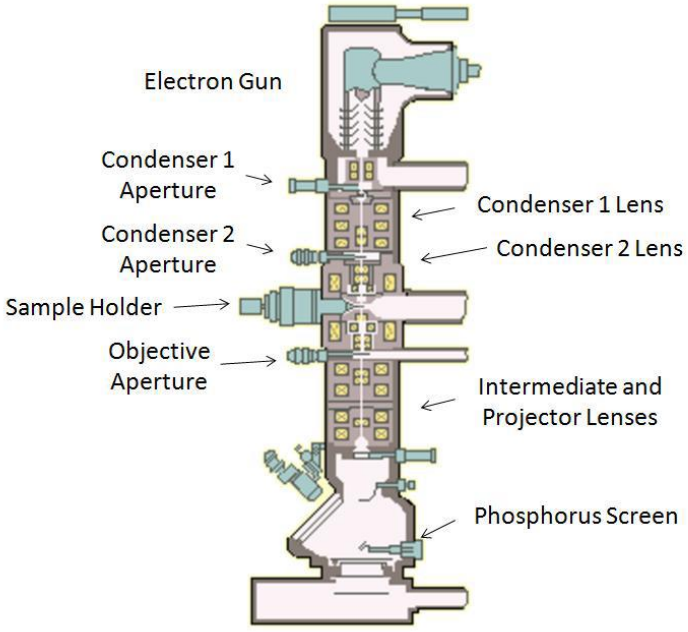

Figure 3.4. Schematic of the TEM column including all its components.

Chapter 4. Understanding $Na_2Ti_3O_7$ as an ultra-low voltage anode material for Na-ion batteries

An in-depth understanding of $Na_2Ti_3O_7$ as an anode for Na-ion batteries is reported. The electrochemical performance is significantly enhanced with carbon coating, as a result of increased electronic conductivity and reduced solid electrolyte interphase formation. Ti^{4+} reduction upon discharge is demonstrated by in-situ XAS. The self-relaxation behavior of fully intercalated phase is revealed, for the first time, due to its structural instability.

4.1. Introduction

Na-ion batteries have recently gained increased recognition as intriguing candidates for next-generation large scale energy storage systems, stemming from the natural abundance and broad distribution of Na resources. Although the energy density of Na-ion battery is not as high as that of Li-ion battery, which is one of the most dominating energy technologies in this decade, there are studies suggesting that Na-ion systems should not be discarded.[55,56] In particular, Na-ion batteries operating at room temperature could be suitable for applications where specific volumetric and gravimetric energy density requirements are not as stringent as in EVs, namely in electrical grid storage of intermittent energy produced via renewable sources.[2] This would also contribute to a significant reduction in the cost connected to the use of renewable sources, which could then penetrate the energy market more easily and make Na-ion technology

complementary to Li-ion batteries for stationary storage.[49,57,58]

For the past several years, a variety of novel materials have been explored as electrode materials for Na-ion batteries. Since Na-ion has a relatively larger ionic radius than Li-ion, materials with an open framework are preferred for facile Na-ion insertion / extraction. Following this strategy, many breakthroughs in cathode materials have been achieved, such as layered and polyanion compounds.[59,60] However, the development of suitable anode materials for Na-ion batteries remains a considerable challenge.[61,62] Graphite cannot be used as anode, since it is unable to intercalate Na-ion reversibly.[8,63] Metallic Na is also ruled out, because it forms dendrites easily and has an even lower melting point than Li. Hard carbons is shown to insert and de-insert Na-ions, delivering capacities about 200–300 mAh g^{-1}.[7,8,64] However, the reversibility for carbonaceous materials still requires further improvement.[9,65] Na-alloys are proposed as possible alternatives, as they can potentially provide higher specific capacities.[18,66–69] These alloys, however, suffer from large volume changes upon uptake / removal of Na, in analogy to Li-alloys.[58] Another emerging class of materials is transition metal oxides. For example, $NaVO_2$ is shown to yield a reversible capacity (e.g. <130 mAh g^{-1}) at C/100 current rate, but its operating voltage is at 1.5 V *vs.* Na^+/Na, leading to a low energy density.[70] Ti-based oxides are suggested to be an attractive alternative, considering that $Li_4Ti_5O_{12}$ is one of the few commercialized anode materials in Li-ion battery.[71,72] Several different sodium titanates have been explored as anodes for Na-ion battery.[73–77] Among them, a study by Palacín et. al. demonstrated that the layered oxide $Na_2Ti_3O_7$ could reversibly exchange Na-ions with the lowest voltage ever reported for an oxide insertion electrode.[76] The ultra low voltage and intrinsic high reversibility of this material make it a strong

anode candidate for Na-ion battery. Very recently, the same group identified the fully intercalated phase, $Na_4Ti_3O_7$, and provided additional insight on the low intercalation potential of this material, using DFT calculations.[77] However, more work is still required to closely connect the fundamental properties with the battery performance and to systematically evaluate whether it can be a viable anode for Na-ion battery. Herein, we report a comprehensive study in order to unveil the underlying relationship between its intercalation mechanism and practical battery performance for $Na_2Ti_3O_7$ anode.

4.2. Experimental

Pure $Na_2Ti_3O_7$ was prepared from anatase TiO_2 (>99.8%, Aldrich) and anhydrous Na_2CO_3 (>99.995%, Aldrich) mixtures with 10% excess of the latter based on stoichiometric amounts. These mixtures were milled and calcinated at 800°C for 40h. The carbon coating was applied according to previous report:[76] $Na_2Ti_3O_7$ particles was dispersed in distilled water and ethanol solution, and mixed with sucrose solution. Then, a heat treatment at 600°C was conducted after drying. The as-synthesized materials were characterized by a Philips XL30 environmental scanning electron microscope (ESEM) operating at 10 kV, and an FEI Tecnai G2 Sphera transmission electron microscopy (TEM) operating at 200 kV. XRD patterns were collected at ambient temperature on a Bruker D8 Advance diffractometer, using a LynxEye detector at 40 kV and 40 mA. Cu-anode (Kα, λ = 1.5418 Å) was used, with a scan speed 60 of 1 s/step, a step size of 0.02° in 2θ, and a 2θ range of 10−70°. XRD data analysis was carried out by utilizing Rietveld refinement using the FullProf software package. X-ray absorption spectroscopy measurements were performed at 20-BM-B beamline of Applied Photon Source (APS) at

Argonne National Laboratory. Customized coin cells were used to prevent the sample contamination. Measurements at the Ti K-edge were performed under transmission mode using gas ionization chamber to monitor the incident and transmitted X-ray intensities. A third ionization chamber was used in conjunction with a Ti-foil standard to provide internal calibration for the alignment of the edge positions. The incident beam was monochromatized using a Si (111) double-crystal fixed exit monochromator. Harmonic rejection was accomplished using a rhodium-coated mirror. The reference standard, Ti_2O_3, was prepared by spreading uniform layer of powders on Kapton. Each spectrum was normalized using data processing software package IFEFFIT.[78]

Electrodes were prepared by mixing 70 wt% active material, 10 wt% polyvinylidene fluoride (PVdF), and 20 wt% Super P carbon black. For the electrodes fabricated with bare $Na_2Ti_3O_7$ and carbon coated $Na_2Ti_3O_7$, same amount of external Super P carbon black (20 wt%) were added. A glass fiber GF/F (Whatman) filter was used as separator. 1 M NaPF6 in a 1:1 (v/v) mixture of ethylene carbonate (EC) and diethylene carbonate (DEC) solution was used as electrolyte. For half-cell test, the counter electrode was sodium metal foil (Sigma-Aldrich). For full cell tests, the counter electrode was $Na_{0.80}Li_{0.12}Ni_{0.22}Mn_{0.66}O_2$, reported in our previous work.[35] The cathode to anode weight ratio was around 2.36 : 1 in full cell. Both electrodes were directly assembled into the full cell without a pre-cycle with Na metal. All batteries were assembled in an MBraun glovebox (H_2O < 0.1ppm). Galvanostatic discharge and charge at various current densities were performed on an Arbin BT2000 battery cycler. The voltage windows for half cell and full cell were 0.01 - 2.5 V and 2.0 - 4.2 V respectively.

Density functional theory (DFT) calculations were performed in the spin-polarized GGA + U approximations to the Density Functional Theory (DFT). Core electron states were represented by the projector augmented-wave method[79] as implemented in the Vienna ab initio simulation package (VASP).[80] The Perdew-Burke-Ernzerhof exchange correlation[81] and a plane wave representation for the wave function with a cutoff energy of 400 eV were used. The Brillouin zone was sampled with a dense k-points mesh by Gamma packing. The supercell was composed of two formula units of $Na_2Ti_3O_7$. The atomic positions and cell parameters were fully relaxed to obtain total energy and optimized cell structure. The Hubbard U correction was introduced to describe the effect of localized d electrons of transition metal ions. Each transition metal ion has a unique effective U value applied in the rotationally invariant GGA + U approach. The applied effective U value given to Ti-ion was 3 eV, consistent with early work.[56]

4.3. Results and Discussion

$Na_2Ti_3O_7$ was prepared by a simple mechanical mixing of anatase TiO_2 and anhydrous Na_2CO_3, followed by calcination at 800 ℃ (for experimental details, see ESI). The as-synthesized material was well crystallized into P21/m space and adopted a pellet shape (Figure 4.1). The white color of the obtained powder suggested its intrinsic insulating property, which is undesired for battery application. Therefore, carbon coating by sucrose pyrolysis was applied to improve electronic conductivity.[82] The electrochemical properties were tested in Na half cell over a voltage window of 0.01–2.5 V (for experimental details, see ESI). Figure 4.2 presents the first cycle electrochemical

profile. The average intercalation potential is around 0.35 V, and a large amount of excess capacity in the first discharge is observed mainly due to irreversible Na intercalation into carbon additive (Super P) in the electrode, consistent with previous literature.[76] Starting from the first charge, the theoretical capacity of 177 mAh g^{-1} (corresponding to 2 Na insertion per formula unit) is fully delivered and more than 115 mAh g^{-1} capacity is well maintained after 100 cycles for the carbon-coated $Na_2Ti_3O_7$ (Figure 4.3 (a)). Besides the excellent cycling properties, good rate performance is achieved as a result of improved electronic conductivity as illustrated in Figure 4.4. Compared with carbon-coated $Na_2Ti_3O_7$, the as-synthesized (henceforth referred to as "bare $Na_2Ti_3O_7$") displays notably reduced capacity (Figure 4.3 (b)). Therefore, the coated carbon plays an important role in enhancing the battery performance.

To evaluate the practical application of $Na_2Ti_3O_7$, herein we demonstrate for the first time a full Na cell using $Na_2Ti_3O_7$ as anode material. Figure 4.3 (c) is the voltage profile of the $Na_2Ti_3O_7$ / P2 - $Na_{0.80}Li_{0.12}Ni_{0.22}Mn_{0.66}O_2$ full cell, in which the cathode material, P2 - $Na_{0.80}Li_{0.12}Ni_{0.22}Mn_{0.66}O_2$, has been reported by us previously.[35] Due to the ultralow voltage of $Na_2Ti_3O_7$ anode, the average voltage of this full cell is as high as 3.1 V, which is comparable to commercial Li-ion battery. As seen in Figure 4.3 (c) inset, the Na full cell can easily light up a 2.5 V LED bulb. The cycling of the full cell at C/10 rate is displayed in Figure 4.3 (d). The capacity is stabilized at 105 mAh g^{-1} after 25 cycles (capacity is determined by anode active material). At the same time, the coulombic efficiency is gradually increased to above 98% and maintained in the subsequent cycles. The overall energy density is 100 Wh kg^{-1}, based on the total weight of active materials from both cathode and anode. Although the energy density is lower than that of Li-ion

battery, it should be noted that Na does not alloy with Al, so that the Al current collector can be used for both cathode and anode. This will help to further improve energy density of Na-ion battery and reduce manufacturing cost.

High resolution transmission electron microscopy (HRTEM) images revealed the surface morphologies for bare and carbon-coated $Na_2Ti_3O_7$ samples. At pristine state (Figure 4.5 (a) and (b)), the lattice fringes are clearly observed, implying good crystallinity. The width (0.84 nm) of neighbouring fringe distance is corresponded to (0 0 1) plane. As suggested by Figure 4.5 (b), the carbon is uniformly coated on the surface of $Na_2Ti_3O_7$ with a thickness around 3 nm. After 1st discharge, an amorphous layer with a thickness of 30-50 nm is seen on the bare $Na_2Ti_3O_7$ particle (Figure 4.5 (c)), indicating a severe side reaction at the solid electrolyte interface (SEI). In contrast, the SEI layer is largely inhibited in the carbon-coated $Na_2Ti_3O_7$ (Figure 4.5 (d)). Consequently, it is noticed that the initial coulombic efficiency is increased by 11 % from bare to carbon-coated sample (Figure 4.2). This demonstrates that in addition to improving the electronic conductivity, the coated carbon on the surface could also serve as a protection layer to prohibit side reactions of the electrolyte and enhance battery performance. It should be noted that the carbon coating could only partially improve the inefficiency in the 1st cycle, since the main irreversible capacity is resulted from Na react with super P.[76]

In order to understand the structural evolution and the ultra low voltage for $Na_2Ti_3O_7$ upon cycling, the $Na_xTi_3O_7$ as well as its Li analogue $Li_xTi_3O_7$ ($2 \leq x \leq 4$) was investigated by first principles calculation. The fully intercalated phase, $Na_4Ti_3O_7$, is identified by our calculation, which is in agreement with Dr. Palacin et.al.'s recent report.[77] More details of the phase transformation can be revealed by closely examining

structural difference between $Na_2Ti_3O_7$ and $Na_4Ti_3O_7$. As shown in Figure 4.6 (a), although there is no bond broken in Ti-O frameworks, the Na sites experience drastic variations. The Na-ion coordination decreases from 9 and 7 at pristine state to 6 after fully intercalation. In addition, to accommodate more Na-ions in the structure, the lattice parameters are adjusted by shearing the Ti-O slabs. The c lattice parameter is considerably reduced due to better screening effect from high Na-ion concentration in Na layer. More interestingly, the dramatic Na site change is not just due to the shift of the Ti-O slab but also from contributions involving modifications within the Ti-O framework as well. After full intercalation, the joint angle between neighbouring Ti-O blocks is enlarged from 82.11 °to 93.25 ° (Figure 4.6 (b)). Therefore, it is fascinating to notice that this type of framework possesses structural flexibility to some degree, which is quite unique compared with traditional layered intercalation compounds, such as $LiCoO_2$. As for the intercalation voltage, the calculated values for both $Na_xTi_3O_7$ and $Li_xTi_3O_7$ are basically consistent with experimental results (Figure 4.6 (c)).[77] Based on Nernst equation, the battery voltage is directly related to the Gibbs free energy change during chemical reaction. Thus, the lower voltage for $Na_xTi_3O_7$ compared with $Li_xTi_3O_7$ is associated with the smaller change in Gibbs free energy in the Na case. In addition, we have studied the electrostatic interaction in the crystal structure using Ewald summation.[83] It is interesting to see that there is a bigger jump in electrostatic energy for $Na_xTi_3O_7$ from x=2 to x=4 than that for $Li_xTi_3O_7$, demonstrating a much stronger electrostatic repulsion in $Na_4Ti_3O_7$. Such large electrostatic repulsion leads to structural instability and consequently, increases the Gibbs free energy for $Na_4Ti_3O_7$. Therefore, the

overall change in Gibbs free energy upon intercalation is reduced in Na case and the voltage is lowered accordingly.

Owing to the strong electrostatic repulsion in the fully discharged phase, $Na_4Ti_3O_7$, a "self-relaxation" behaviour was observed. As shown in Figure 4.7 (a), the diffraction pattern for $Na_4Ti_3O_7$ phase is obtained right after the full discharge was completed. However, for the electrodes stored in the glovebox for 3 and 10 days after full discharge, the intensity of peaks from $Na_4Ti_3O_7$ phase, such as (-3 0 2) and (1 0 4) gradually and systematically diminishes. Concomitantly, the diffraction peaks from the $Na_2Ti_3O_7$ phase increases steadily. These observations suggest that the $Na_4Ti_3O_7$ structure undergoes self-relaxation progressively. This property is also captured electrochemically. Figure 4.8 compares the voltage profiles for $Na_2Ti_3O_7$ under cycling with and without interval rest (between charge and discharge) respectively. It is observed that the open circuit voltage for the cell with interval rest is increased gradually during the rest time, indicating the structural relaxation. Additionally, though the discharge performances are identical in the two cases, the cell with interval rest can only deliver 130 mAh g^{-1} capacity in the first charge and further decay is seen in the subsequent cycles (Figure 4.8 (c) and Figure 4.9). Considering that this self-relaxation in the anode material would lead to self-discharge in the actual full cell, it could be one of the main bottlenecks using $Na_2Ti_3O_7$ as anode for Na-ion battery in practice.

The electronic transition was detected by in-situ X-ray absorption spectroscopy (XAS). Customized coin cells were used to prevent the sample contamination. As Ti^{3+} is extremely sensitive to oxidization (Ti^{3+}->Ti^{4+}), any ex-situ characterization attempts to detect Ti reduction during lithiation process were not successful. It is important to make

sure that throughout the entire characterization process, the electrodes were never exposed to the ambient environment. In Figure 4.7 (b), the Ti-K edge is gradually shifted towards lower energy region from pristine state to 0.01 V. The shape and position of the pre-edge as well as the position of the main edge for the fully discharged sample approach those found for Ti_2O_3, demonstrating that Ti^{4+} is reduced upon Na-ion intercalation. The decrease in the pre-edge peak is ascribed to the reduced hybridization between Ti-3d and O-2p orbitals during Ti ion reduction.[84,85] In fact, this Ti reduction is similar to its Li counterparts.[84,86,87] Therefore, it is speculated that the ultra-low voltage for $Na_2Ti_3O_7$ material during intercalation could mainly originate from crystal structural perspective as discussed above, instead of electronic contribution.

4.4. Conclusion

In summary, a comprehensive study on $Na_2Ti_3O_7$ as an ultra-low voltage anode for Na-ion batteries is reported. The cyclability and coulombic efficiency are significantly enhanced, due to increased electronic conductivity and reduced SEI formation by carbon coating. Na full cell with high operating voltage is demonstrated by taking advantage of the ultra-low voltage of $Na_2Ti_3O_7$ anode. The self-relaxation behaviour for fully intercalated phase, $Na_4Ti_3O_7$, is shown for the first time, which results from structural instability as suggested by first principles calculation. Ti^{4+} / Ti^{3+} is the active redox couple upon cycling based on XANES characterization. These findings unravel the underlying relation between unique properties and battery performance of $Na_2Ti_3O_7$ anode, which should ultimately shed light on possible strategies for future improvement.

Chapter 4, in full, is a reprint of the material "$Na_2Ti_3O_7$ as an ultra-low voltage anode material for a Na-ion battery" as it appears in the Chemical Communications, J. Xu, C. Ma, M. Balasubramanian, Y. S. Meng, 2014, 50, 1256. The dissertation author was the co-primary investigator and author of this paper. All the experiment parts were performed by the author except for the computational part.

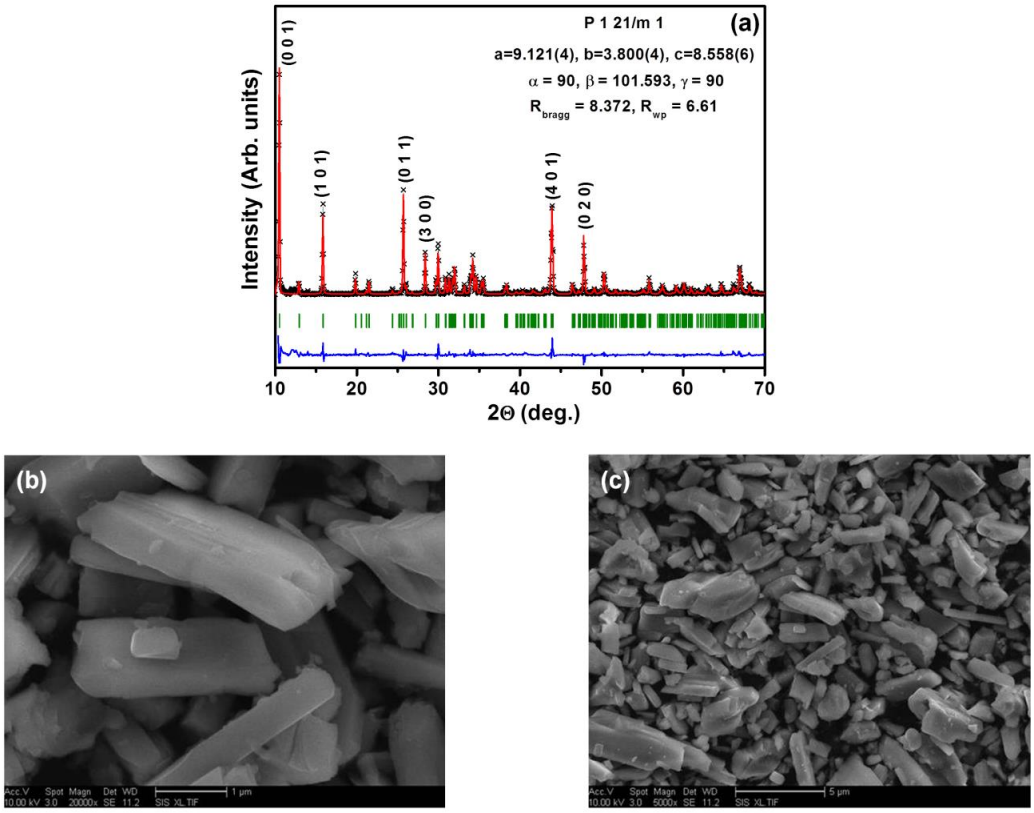

Figure 4.1. The (a) XRD and (b) (c) SEM images of as-synthesized $Na_2Ti_3O_7$ powder.

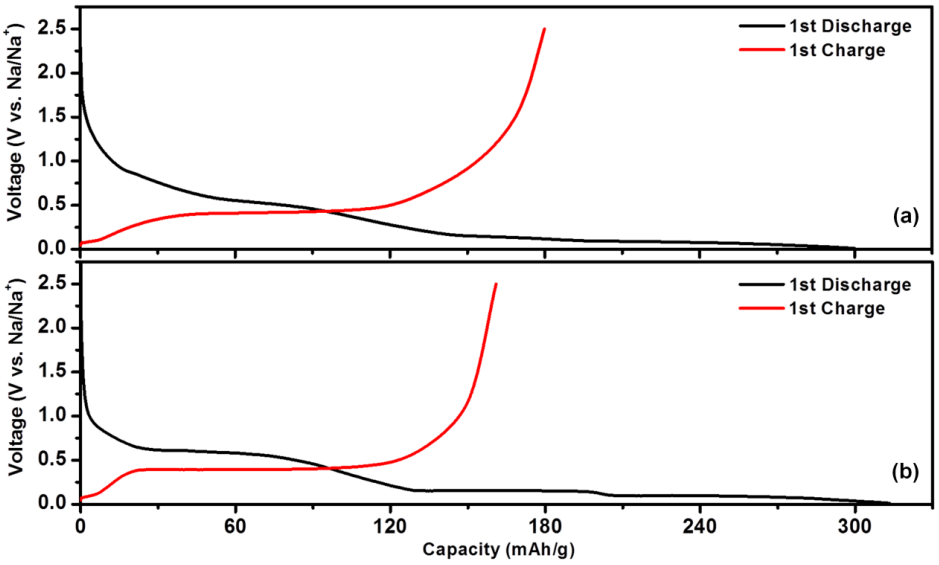

Figure 4.2. Electrochemical profiles at of (a) carbon-coated and (b) bare $Na_2Ti_3O_7$ at C/25.

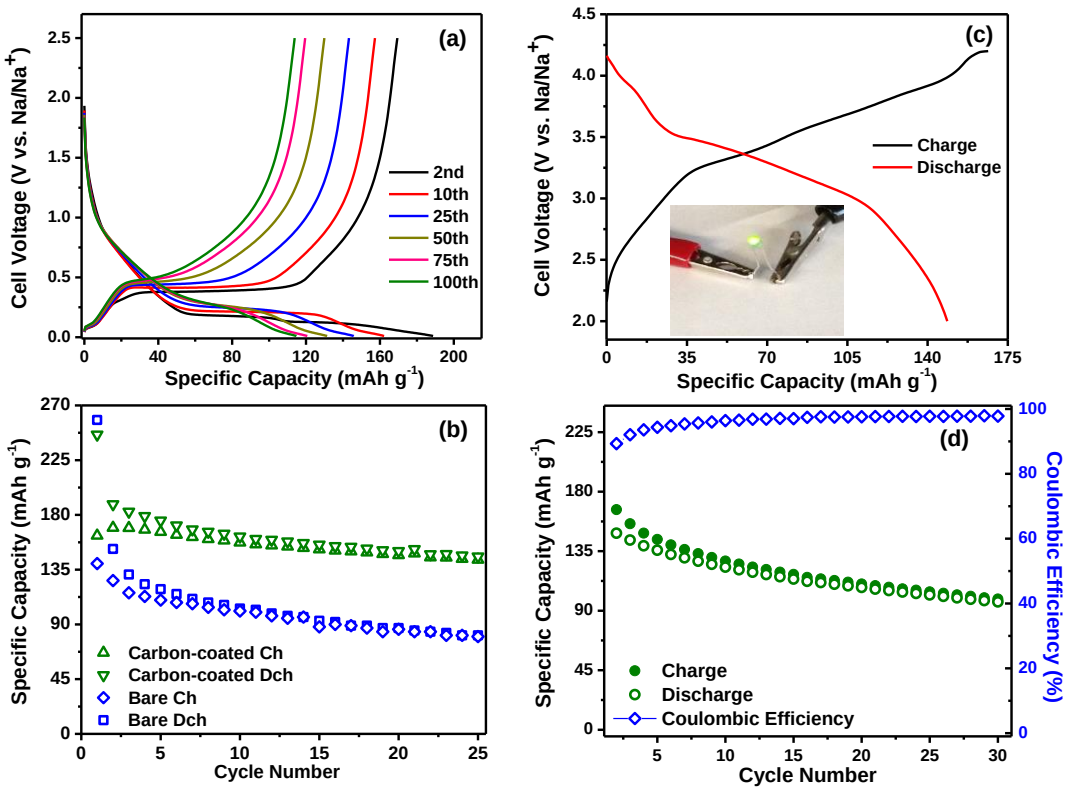

Figure 4.3. (a) Voltage profiles of carbon-coated $Na_2Ti_3O_7$ in the 2nd, 10th, 25th, 50th, 75th and 100th cycles at C/10 rate. (b) Cycling performance for carbon-coated and bare $Na_2Ti_3O_7$. (c) Voltage profiles and (d) Cycling performance for the Na full cell (the specific capacity is calculated based on anode materials).

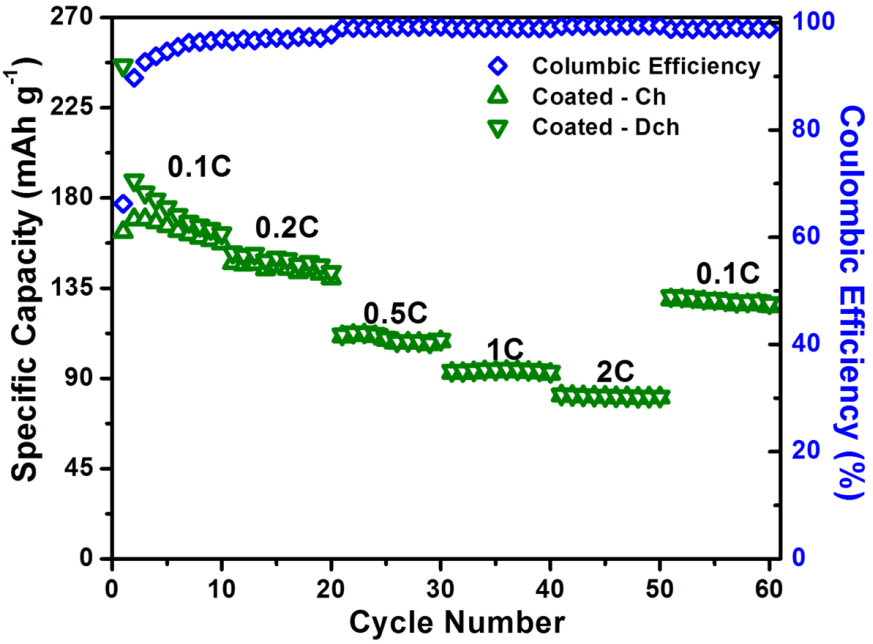

Figure 4.4. Rate performance of carbon-coated $Na_2Ti_3O_7$ electrode.

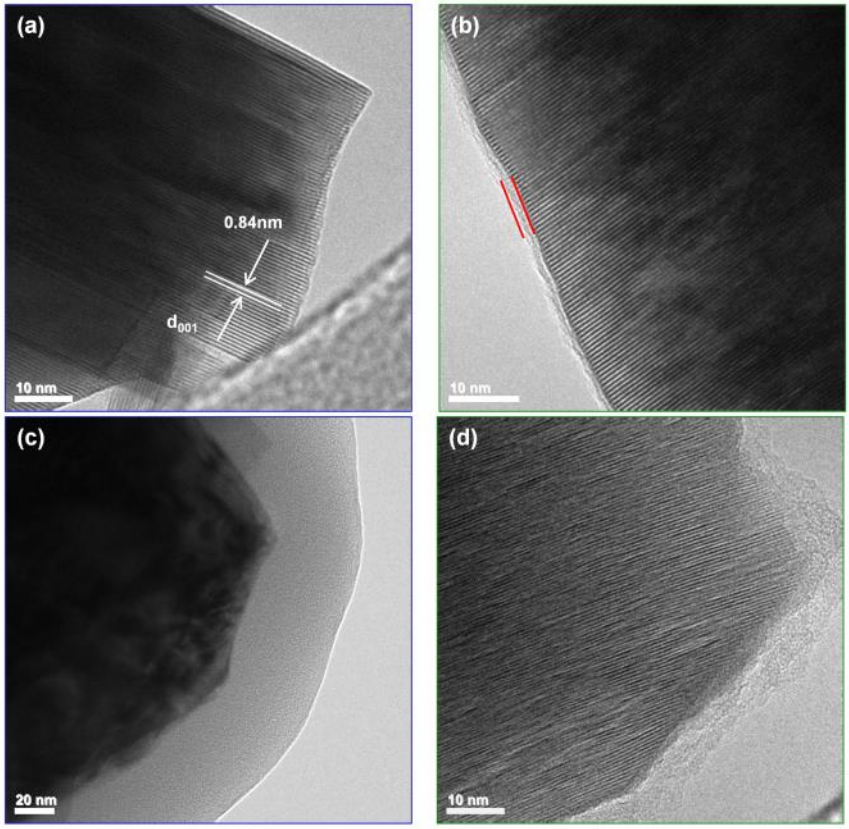

Figure 4.5. TEM images for (a) bare and (b) carbon-coated $Na_2Ti_3O_7$ at pristine state. TEM images for (c) bare and (d) carbon-coated $Na_2Ti_3O_7$ after 1st discharge.

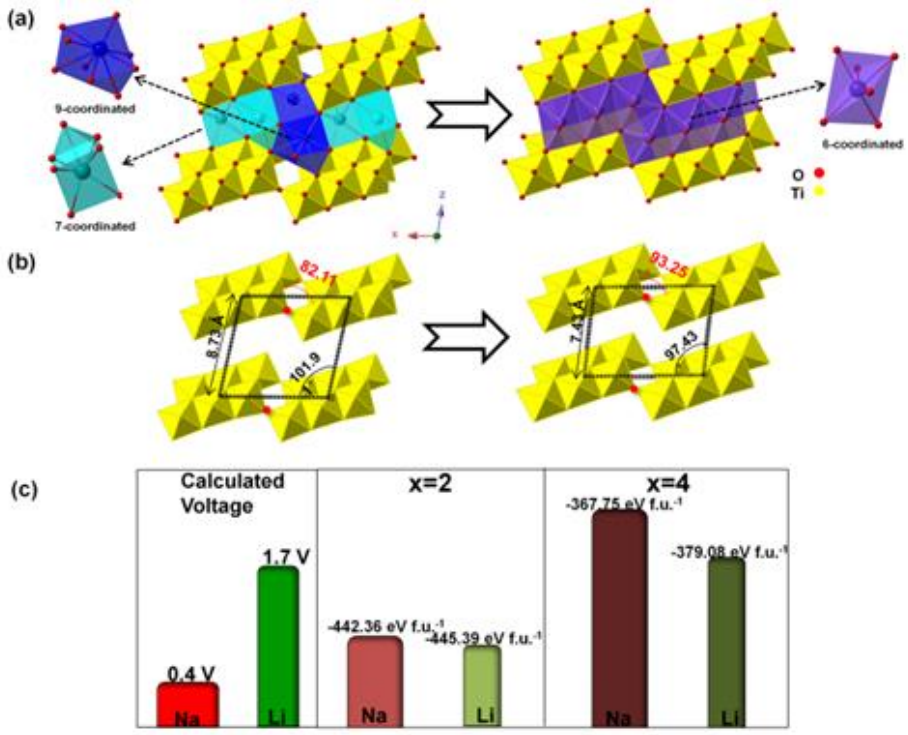

Figure 4.6. (a) The phase transformation (b) related structural change upon Na intercalation. (c) The calculated voltage and electrostatic energy at x=2 and x=4 for $Li_xTi_3O_7$ and $Na_xTi_3O_7$ respectively. The narrow bar is for $Li_xTi_3O_7$ and wide one for $Na_xTi_3O_7$.

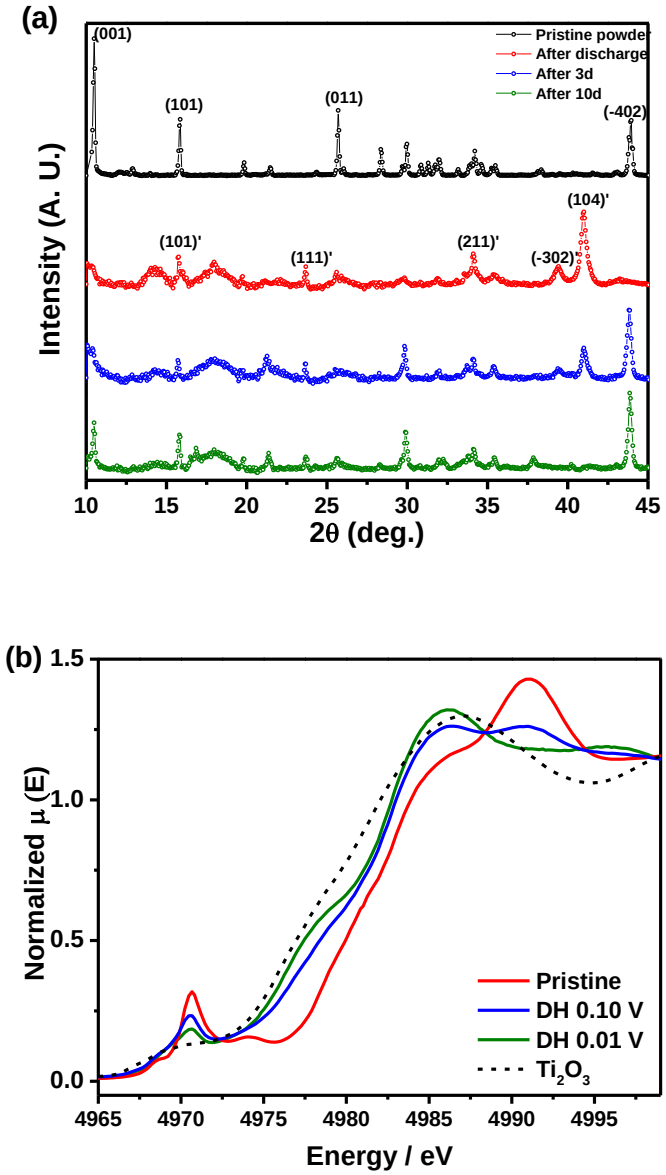

Figure 4.7. (a) Change in the XRD patterns with time for fully discharged electrodes. (b) Normalized Ti K-edge XANES for $Na_2Ti_3O_7$ at pristine state (red), after discharged to 0.10 V (blue), and after discharged to 0.01 V (green).

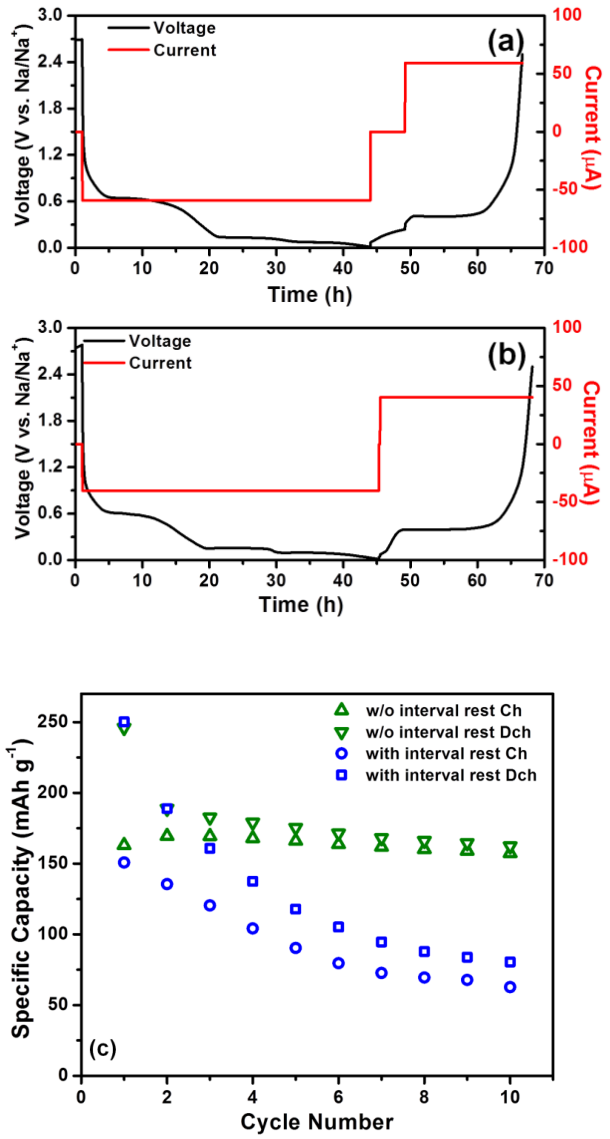

Figure 4.8. Voltage profiles for electrodes under cycling (a) with and (b) without interval rest (5 hour between charge and discharge). (c) Cycling performance for cell with (blue) and without (green) interval rest.

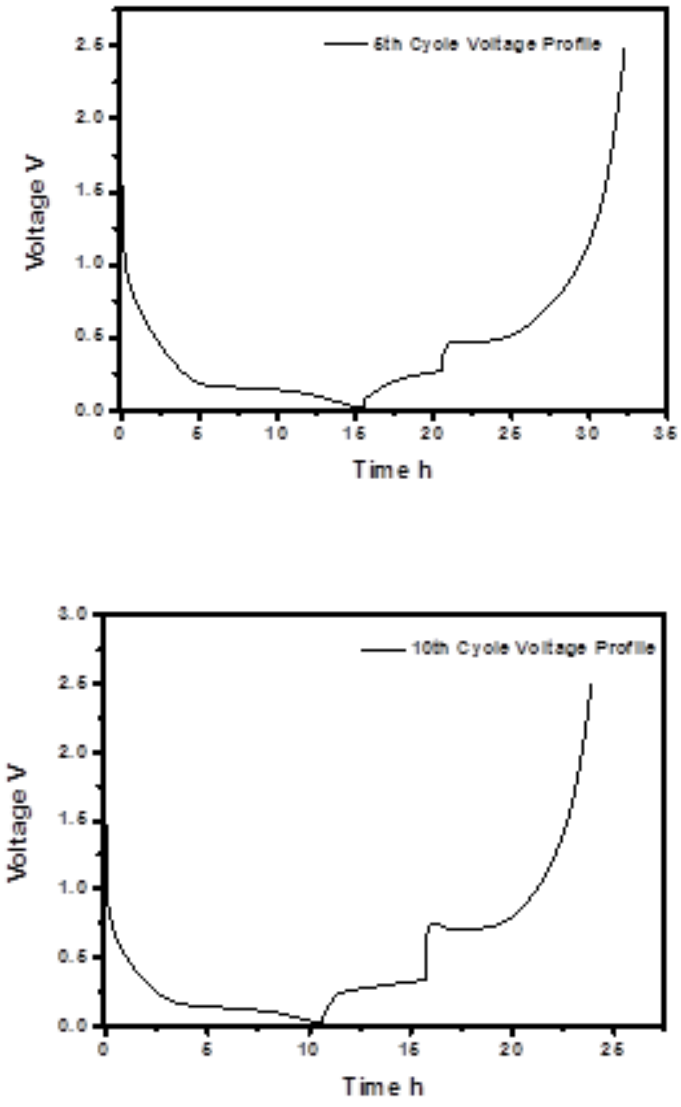

Figure 4.9. 5th and 10th Voltage profiles for electrodes with interval rest (5 hour between charge and discharge).

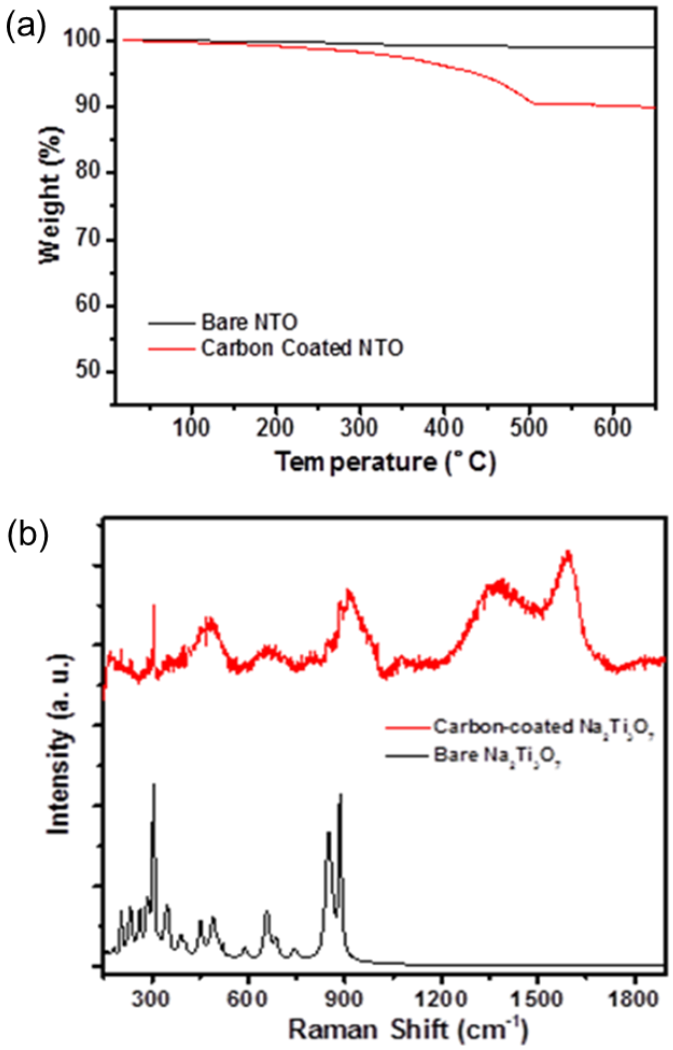

Figure 4.10. Thermogravimetric analysis and (b) Raman spectrum for bare (black) and carbon coated (red) $Na_2Ti_3O_7$ powder.

Chapter 5. Investigating the Energy Storage Mechanism of SnS_2-rGO Composite Anode for Advanced Na-Ion Batteries

Tin sulfide–reduced graphene oxide (SnS_2-rGO) composite material is investigated as an advanced anode material for Na-ion batteries. It can deliver a reversible capacity of 630 mAh g^{-1} with negligible capacity loss and exhibits superb rate performance. Here, the energy storage mechanism of this SnS_2-rGO anode and the critical mechanistic role of rGO will be revealed in detail. A synergistic mechanism involving conversion and alloying reactions is proposed based on our synchrotron X-ray diffraction (SXRD) and *in situ* X-ray absorption spectroscopy (XAS) results. Contrary to what has been proposed in the literature, we determined that Na_2S_2 forms instead of Na_2S at the fully discharge state. The as formed Na_2S_2 works as a matrix to relieve the strain from the huge volume expansion of the Na-Sn alloy reaction, shown in the high resolution transmission electron microscope (HRTEM). In addition, the Raman spectra results suggest that the rGO not only assists the material to have better electrochemical performance by preventing particle agglomeration of the active material, but also coordinates with Na-ions through electrostatic interaction during the first cycle. The unique reaction mechanism in SnS_2-rGO offers a well-balanced approach for sodium storage to deliver high capacity, long-cycle life, and superior rate capability.

5.1. Introduction

The pressing demand for economically accessible and environmentally benign energy storage technologies has strongly promoted the need for scientific study in this area. Alternative energy storage systems to lithium-ion technology are drawing more attention in the field of rechargeable batteries.[2,61] The large abundance of Na, low cost, and suitable redox potential of rechargeable Na-ion batteries (NIBs) show great promise for energy storage applications.[2] Research on NIBs can be traced back to the 1970s, when Delmas et al began to study the structure properties of Na_xTMO_2.[5,88] The major obstacle in realizing NIBs in practice was the absence of suitable negative electrodes. On the other hand, the research and commercialization of lithium-ion batteries (LIBs) gained huge success due to the discovery of the graphite anode in the 1990s.[89] As a result, limited efforts were devoted to NIBs in the last two decades.

Because the demand for large-scale batteries for electric energy storage system increased, the research interest in NIBs was revitalized in 2010. Although several breakthroughs were made on cathodes for NIBs, the anode remains as the main bottleneck.[32,35,59] Graphite gained massive attention because of LIBs; however, Na-ions are not able to intercalate unless diglyme-based electrolyte are used by adopting a co-intercalation mechanism.[90] Therefore, several non-graphitic carbon anodes have been studied.[8] Tin and tin-based compounds have drawn much attention as high-capacity NIB anodes because of the theoretical stoichiometry of $Na_{15}Sn_4$ (847 mAh g^{-1}) and low redox potential.[14] Various Sn-based materials were explored as potential high energy anodes for NIBs.[15,16,67,91–97] For instance, Komaba et al. demonstrated that Sn powder electrodes with polyacrylate binder delivers a capacity of 500 mAh g^{-1} in aprotic Na cells for 20

cycles.[15] Sn-SnS-C nanocomposites have demonstrated reversible capacities of 664 mAh g^{-1} at 20 mA g^{-1} and 350 mAh g^{-1} at 800 mA g^{-1}.[67] Kim and co-workers reported the use of Sn_4P_3 as a promising anode material, which delivers a reversible capacity of 718 mAh g^{-1} with stable cycle performance.[96] Very recently, we proposed a novel SnS_2-rGO composite anode with excellent electrochemical performance for NIBs.[98] The SnS_2-rGO electrode demonstrated a high reversible capacity (630 mAh g^{-1} at 0.2 A g^{-1}), good rate performance (544 mAh g^{-1} at 2 A g^{-1}), and long cycle-life (500 mAh g^{-1} at 1 A g^{-1} for 400 cycles). In this material, intuitively, the SnS_2 should first undergo a conversion reaction with Na to form Sn and Na_2S. Then Sn should further alloy with Na to form $Na_{15}Sn_4$ alloy phase. However, a more in-depth study of the SnS_2-rGO composite reveals a sophisticated reaction pathway.

A comprehensive study on the energy storage mechanism of SnS_2-rGO composite as the anode material in NIBs is reported. The structural evolution and phase transformation of the electrode upon discharge/charge are tracked by synchrotron X-ray diffraction (SXRD) and high-resolution transmission electron microscopy (HRTEM). It is found that Sn appears as an intermediate product which then turns into $Na_{15}Sn_4$ alloy during sodiation. Moreover, Na_2S_2 is confirmed as the final reaction product rather than Na_2S. The SnS_2 becomes amorphous upon insertion/removal of Na-ions after a full cycle. Meanwhile, *in situ* X-ray absorption spectroscopy (XAS) was utilized to elucidate the local structure evolution and reveal the detailed sodiation mechanism. We observed a synergistic mechanism which reveals the occurrence of simultaneous conversion and alloy reactions. The importance of this unique mechanism is discussed in terms of reaction kinetics and cycling performance. In order to determine the contribution of rGO

in the electrochemical performance, the charged/discharged samples were characterized by Raman spectroscopy. Here, rGO prevents particle agglomeration during the formation of SnS_2, which will be explained in further detail. These studies enable us to understand the underlying principles that allow SnS_2-rGO to achieve excellent electrochemical performance; therefore, providing guidelines to design advanced anode materials for high-energy NIBs.

5.2. Experimental

The materials were synthesized following previous published work.[98] Graphite oxide (GO) was prepared from graphite powder by a modified Hummers' method.[99] The typical synthesis of SnS_2-rGO composite is as follows: 0.7015 g $SnCl_4 \cdot 5H_2O$ (Alfa Aesar) and 0.6014 g thioacetamide (TAA) (Sigma-Aldrich) were added to 40 ml of 1.5 mg ml^{-1} GO suspension under stirring. The mixture was sonicated for 30 minutes before transferring it to a 50 ml Teflon-lined stainless steel autoclave and heated at 160 ℃ for 12 hours. After cooling to room temperature, the solid product was centrifuged, washed with deionized water and absolute alcohol (three times each), and then vacuum dried at 60 ℃ overnight. Pure SnS_2 was synthesized under the same conditions but without the presence of GO. The dried product was then heated in Ar at the rate of 5 ℃ $minutes^{-1}$ to 400 ℃ and maintained for 4 hours. The material was characterized by a Philips XL30 environmental scanning electron microscope (ESEM) operating at 10 kV, and an FEI Tecnai G2 Sphera transmission electron microscopy (TEM) operating at 200 kV. Powder X-ray diffractions (XRD) were recorded on a Bruker pXRD using Cu Kα radiation.

The samples characterized by XRD were obtained by disassembling the cycled batteries in an argon filled glovebox. The electrode materials were washed using battery grade dimethyl carbonate (DMC) three times, then stripped off from the aluminum current collectors. The powders from the cycled electrode were then mounted in the hermitically sealed capillary tubes for *ex situ* XRD. Powder diffractions of all samples were taken using synchrotron XRD at the Advanced Photon Source (APS) on beamline 11-BM (l = 0.459 Å). The beamline uses a sagittal focused X-ray beam with a high precision diffractometer circle and perfect Si (111) crystal analyzer detection for high sensitivity and resolution. XRD patterns were collected between 0.3° and 50.0° in 2θ angles.

X-ray absorption spectroscopy measurements were performed at 20-BM-B beamline of Applied Photon Source (APS) at Argonne National Laboratory. Customized coin cells were used to prevent the sample contamination. Measurements at the Sn K-edge were performed under transmission mode using gas ionization chamber to monitor the incident and transmitted X-ray intensities. A third ionization chamber was used in conjunction with a Sn-foil standard to provide internal calibration for the alignment of the edge positions. The incident beam was monochromatized using a Si (111) double-crystal fixed exit monochromator. Harmonic rejection was accomplished using a rhodium-coated mirror. Each spectrum was normalized using data processing software package IFEFFIT.[78]

The cycled electrodes were washed with battery grade DMC to remove any residual salt. In an argon filled glovebox, the electrodes were placed in a customized Raman sample holder to prevent air exposure during the analysis. Using a Renishaw

inVia Raman Microscope, the samples were exposed to a green laser (532nm wavelength) with a spot size of 5 μm in diameter for 20 seconds at one acquisition. The laser intensity was 10% in order to minimize sample damage. All of the samples were taken from 250-2000 cm^{-1} spectra range and with a 40x objective lens.

Electrodes were prepared from slurries containing 80 wt% of active material (based on the total mass of SnS_2-rGO composite), 10 wt% of Na- alginate as a binder, and 10 wt% Super P carbon black as a carbon additive in deionized water. The slurries were then casted on aluminum foil and dried in vacuum at 80 ℃. Typical loading of the active material was 2 mg cm^{-2}. A glass fiber GF/F (Whatman) filter was used as the separator and 1 M $NaPF_6$ in a 1:1 (v/v) mixture of ethylene carbonate (EC) and diethyl carbonate (DEC) was used as the electrolyte. Battery assembly was carried out in an MBraun glovebox (H_2O < 0.1ppm). Galvanostatic discharge and charge at various current densities were performed on an Arbin BT2000 battery cycler.

5.3. Results and Discussion

5.3.1. Electrochemical Performances of SnS_2-rGO

Figure 5.1 (a) shows the galvanostatic charge-discharge voltage profiles of the SnS_2-rGO composite electrode at the current density of 0.2 A g^{-1} at the 1st, 2nd, 20th, and 100th cycles. In the first cycle, the material exhibited a reversible capacity of 630 mAh g^{-1} with 75% coulombic efficiency. After 100 cycles, the anode maintained a capacity of 627 mAh g^{-1}, exhibiting excellent capacity retention. In our previous work, this material demonstrated superb performance at high current density, which is shown in Figure 5.2.[98] Although the voltage profiles look smooth without any voltage plateaus, the

corresponding dQ dV^{-1} curves for each cycle plotted in Figure 5.1 (b) indicate that multiple reactions occur during electrochemical cycling. In the first cycle, a reduction peak around 1.7 V is assigned to the intercalation of the Na-ions into SnS_2 (0 0 1) plane.[100] The major reduction peaks around 0.7 V is due to the combination of the synergetic conversion and alloying reactions as well as the irreversible formation of the solid electrolyte interphase (SEI). The peaks around 0.3 V and 0.01 V could be ascribed to the formation of Na-Sn and Na-S phases. During the charge state, the oxidation peaks around 0.3 V and 0.7 V originate from the desodiation of Na-Sn and Na-S phases. The broad peak from 1.0 V to 1.5 V is attributed to the desodiation of the Na-Sn alloy phases and the reformation of SnS_2. The peaks in the dQ dV^{-1} curves overlap over subsequent cycles, indicating good stability and reversibility after the first cycle.

5.3.2. Structure Evolution Characterized by SXRD and *In situ* XAS

To obtain direct evidence of the phase transformations during electrochemical cycling, we carried out *ex situ* SXRD analysis on the SnS_2-rGO electrode at different discharge and charge states. The XRD pattern at the pristine state confirmed the crystallinity of the as-synthesized SnS_2 and was indexed as trigonal space group P3m1 (Figure 5.3). As shown in Figure 5.4, the diffraction peaks of the SnS_2 phase gradually disappear during the discharge state while two broad peaks around 9.1 °and 13.2 °appear, indicating the formation of Sn phase. At 0.3 V, the XRD patterns of the discharged electrode matched well with the diffraction patterns of Sn. By applying the Scherrer Equation to the two most intense XRD peaks, the Sn particle size is less than 3 nm.[101] After further discharge, the Sn diffraction peaks disappeared, accompanied by the

appearance of two new broad peaks around 7.0 ° and 11.5 °. The newly observed peaks are resulted from the Na_2S_2 phase. From these observations, it clearly demonstrates that nano-sized Sn particles first nucleate from the conversion reaction of Na and SnS_2. Later, the increasing quantity of Na in Sn host structure results in the formation of amorphous Na-Sn alloys through a series of phase transitions, thus the crystalline Sn diffraction peaks disappeared.[16,91] In the Li-ion system, it is widely acknowledged SnS_2 reacts with Li-ions to form Li_2S. Therefore, previous publications assumed that Sn-S compounds react with Na-ions to produce Na_2S.[67,102] However, the observation of Na_2S_2 phase in this work is intrinsically different, as it could originate from the differences between Li-S and Na-S alloys.[103] After charging the electrode to 1.2 V, the Sn diffraction peaks began to appear and dominate at 1.5 V. This is the result of the dealloying reaction from the Na-Sn alloy. Simultaneously, the XRD peaks of the Na_2S_2 phase dwindled until it disappeared. When the electrode was charged to 2.5 V, there were no well-defined XRD peaks detected. This suggests that the Sn converted to a phase with low crystallinity or to an amorphous state, presumably SnS_2. It is interesting to note that the appearance/disappearance of Na_2S_2 occurred along with the Na-Sn alloying reaction, indicating that the conversion and alloying reactions happen simultaneously in the lower voltage region. This synergistic effect can accelerate the kinetics of the reactions and improve the structure stability of the material.[104] *In situ* X-ray absorption spectroscopy (XAS) was performed at the Sn K-edge for the active electrode material to reveal more time-resolved information and track the evolution of local structures.

Figure 5.5 represents Fourier transforms of the selected Sn K-edge EXAFS patterns as a function of cell voltage. The peaks around 1.9 Å and 3.4 Å in the pristine

sample are related to the Sn-S and Sn-Sn interactions, respectively. As the electrode was discharged, the intensity of both peaks decreased significantly due to the displacement of reactive species during the conversion reaction. Meanwhile, a peak around 2.77 Å began to appear and continued to grow upon discharge, belonging to the Sn-Sn interaction in the phase of Sn that nucleated from the conversion reaction.[105,106] The Sn-S peak was observed until the final discharge state, showing the depletion of SnS_2. The formation of Na-Sn alloy phases are determined by the decrease in interatomic distance of Sn-Sn shell from 2.77 Å to 2.74 Å at the fully discharged state.[106] Given the amorphous feature of Na-Sn phases and their similar Sn-Sn bond length to Sn metal; it is hard to determine the exact voltage at which they begin to form. However, previous reports claim that Na-Sn alloy reactions occur starting at 0.7 V.[14,91] Therefore, we propose that the Sn metal generated from the conversion reaction alloys with Na-ions before all the SnS_2 is converted. This is regarded as a synergistic mechanism since it takes advantage of both the conversion and the alloying reactions. The fast kinetics pertaining to the alloying reactions reduces the cell polarization and the Na_2S_2 matrix formed in the conversion reaction helps to accommodate the huge volume variations of Na-Sn alloys. During the first charge, consistent with XRD result, the Sn-S peaks appeared accompanied by the disappearance of the Sn-Sn peaks. At 1.2 V, we observed both the Sn-S interaction from SnS_2 and Sn-Sn interaction in the Na-Sn alloy phases, which indicates that SnS_2 phase was being reconstructed at this voltage. Comparing the XAS results to the XRD results (Figure 5.6) at 1.2 V, the Na-Sn de-alloying reactions were occurring as the SnS_2 were forming; therefore, the alloying and conversion reactions occurred simultaneously again during the charge. The Sn-S peak at the fully charged sample has smaller interatomic

distance and intensity compared to the peak of the pristine SnS_2-rGO sample. Meanwhile, the Sn-Sn interaction of the pristine sample did not regenerate at the fully charged state, demonstrating the formation of nano-clustered SnS_2 rather than crystalline SnS_2 phase (as in the pristine state).[96] Both of the EXAFS and XRD observations portray that the long range ordering decreases as Na-ions are inserted in SnS_2 structure, due to the transformation from crystalline to amorphous found in the active material. After all, the *in situ* XAS provides more evidence for the synergistic reaction mechanism for SnS_2.

5.3.3. TEM Studies of the Cycled Materials

In order to further confirm the proposed reaction mechanism, the cycled electrodes were characterized by HRTEM to obtain a direct image of the structure. Figure 5.6 (a) shows the SnS_2-rGO electrode after the first discharge where the nanoparticles (~10 nm) were embedded in an amorphous matrix. The nanoparticles are Na-Sn alloys that originated from the nano-crystalline Sn formed during conversion reaction. Comparing the size of the Na-Sn alloy to Sn metal (~3 nm), the volume of the nano-particles expands by more than 300%. Therefore, the amorphous Na_2S_2 matrix surrounding the nanoparticles relieves the strain from volume expansion. The co-existence of amorphous Na_2S_2 and $Na_{15}Sn_4$ phases are also identified by selected area electron diffraction (SAED) (Figure 5.6 (b)). The diffusive rings from the Na_2S_2 diffraction is more pronounced because it occupies the major space of the selected area, while the diffraction patterns from $Na_{15}Sn_4$ phase are relatively faint. Figure 5.6 (c) shows the TEM images from another area in the discharged electrode material. Here the lattice fringes could be observed from the nanoparticles because they were on the surface

or the edge of the amorphous matrix. The SAED diffraction patterns show the existence of $Na_{15}Sn_4$ phase with amorphous features. It is difficult to identify the $Na_{15}Sn_4$ phase by solely relying on the XRD patterns because of the lack of long range ordering and particle distribution within the Na2S2 and rGO matrix. Therefore, the HRTEM and SAED provided more information about samples after sodiation. The TEM image of the electrode material at the fully charged state is present in Figure 5.6 (e). Here, the material became completely amorphous and no clear grain boundaries were observed within the particle. Correspondingly, the SAED result demonstrates that the amorphous SnS_2 phase forms at charged state, which is also consistent with our XRD and XAS studies mentioned above.

Based on the characterizations thus far and considering the amount of Na storage capacity according to the electrochemical results, the overall reaction equation could be written as follows:

$SnS_2 + 2Na^+ + 2e^- \rightleftarrows Sn + Na_2S_2$ (theoretical capacity: 293 mAh g^{-1}) [eq. 1]

$Sn + 3.75Na^+ + 3.75e^- \rightleftarrows Na_{3.75}Sn$ (theoretical capacity: 549 mAh g^{-1}) [eq. 2]

The overall theoretical capacity for SnS_2 is 842 mAh g^{-1}. Considering there is 12% rGO in the composite material which delivers negligible reversible capacity,[98] the theoretical capacity for SnS_2-rGO is 740 mAh g^{-1}.

5.3.4. Study the Composite Material by Raman Spectra

Raman spectroscopy was used to characterize the pristine and cycled electrodes in order to determine the properties of rGO and SnS_2 (Figure 5.7). As previously stated, the

2H-SnS_2 nanoparticles used in this study correspond to the D^3_{3d}-P3m1 space group. The crystal structure contains three atoms per unit cell extending in a sandwich layer.

The irreducible representations of the D_{3d} point group are found at the center of the Brillouin zone, Γ:

$$\Gamma = A_{1g} + E_g + 2A_{2u} + 2E_u$$

These optic modes can be divided into three Raman-active modes (A_{1g}, E_g) and three infrared-active modes (A_{2u}, E_u).[107,108]

In black, the pristine electrode exhibits a sharp peak at 314.8 cm^{-1} which corresponds to the A_{1g} Raman active vibration mode.[100,107–111] Meanwhile, the rGO is characterized by the graphitic G band located at 1594.1 cm^{-1}, which is related to the vibration of the sp^2-bonded carbon atoms in a two dimensional lattice (Table 5.1). The disorder and defects in the hexagonal graphitic layer corresponds to the D band at 1350.3 cm^{-1}.[98,110,112,113] As shown in our previous work, the intensity ratio of the D band to the G band (I_D/I_G) was calculated as 1.2 (Table 5.1), which resulted from the decreased sp^2 domains and unrepaired defects during the reduction of GO.[110] The electrode discharged to 0.01 V (in red) shows the elimination of the A_{1g} peak for SnS_2 Raman vibration mode, which demonstrates the full consumption of SnS_2. Moreover, the I_D/I_G ratio drops to 1.02, suggesting that rGO is involved during the sodiation process. The change in intensity ratio (I_D/I_G) is an indication that the rGO sheets order themselves through an electrostatic interaction, which can occur between the rGO sheets and Na-ions.[113] Once the electrode is fully charged to 2.5 V (blue), the I_D/I_G ratio of the rGO sheets returns to 1.3, close to the pristine state. This is an indication that Na-ion could reversibly insert/remove from the rGO, presumably due to the increased distance of the carbon layers. The intensity

ratios and peak positions are summarized in Table 5.1. The appearance of A_{2u} peak in the Raman spectrum (blue) for fully charged electrode suggests the good reversibility of SnS_2. However, we observed a red shift in the broad A_{2u} infrared vibration mode, which is attributed to the formation of nanoparticles and is in agreement with the above mentioned results.[108]

5.3.5. The Effect of rGO

Not only does the rGO play a role in accommodating the Na_2S_2 alloy but more importantly, it also allows for the pristine SnS_2 to be fully consumed and prevents particle agglomeration. Figure 5.8 shows the Raman spectra taken for each electrode at three different spots. This was done to ensure proper reproducibility within the electrode, given that the Raman has a spot size of 5 μm in diameter. For SnS_2-rGO electrode, all three spots exhibit the disappearance of the A_{1g} peak at the fully discharge state and the occurrence of A_{2u} peak at charge state (Figure 5.8 (a) and (b)). This proves that the SnS_2 is fully consumed in discharge and reformed in charge state, as discussed in Figure 5.7. In contrast, the bare SnS_2 electrode showed varied results among different spots. In Figure 5.8 (c), the A_{2u} and E_g peaks from SnS_2 phase were present after the electrode was discharged to 0.01 V, demonstrating that not all of the SnS_2 is consumed in the bare SnS_2 electrode. At the fully charge state, Raman spectrum of each spot within Figure 5.8 (d) is significantly different, indicating that SnS_2 is not regenerated uniformly throughout the electrode. For instance, spot 3 shows that there is no Raman vibration mode for SnS_2 nanoparticles, while spot 1 displays a strong A_{2u} peak. These variations within the Raman results at different spot positions indicate that the formation of SnS_2 in the bare SnS_2

electrode is not fully reversible or uniformly distributed. Therefore, some SnS_2 particle agglomeration occurred during the charge process. Clearly the rGO plays a critical role in evenly dispersing the SnS_2 particles during electrochemical cycling. The rGO allows for a thorough depletion of SnS_2 at the fully discharged state and prevents particle agglomeration during the charged state, thus facilitating the reversibility in reactions.

5.3.6. Energy Storage Mechanism of SnS_2-rGO

The proposed energy storage mechanism according to the systematic characterizations above is summarized in Figure 5.9. During the discharge, the conversion reaction between SnS_2 and Na-ions is the major reaction that occurs above 0.8 V, which generates Sn nanoparticles and amorphous Na_2S_2. Before all the SnS_2 is consumed, the alloy reactions between the Sn metal and Na-ions begin, leading to Na-Sn alloy phases. Therefore, during this region the conversion and alloying reactions happen simultaneously, denoted as the 'conversion + alloying' region. Upon further discharging, the alloying reactions become more dominant below 0.3 V. At the final state of discharge, the nano-sized $Na_{15}Sn_4$ and Na_2S_2 matrix are the final reaction products. The specific capacity calculated based on this reaction is 842 mAh g^{-1} for SnS_2 and 740 mAh g^{-1} for SnS_2-rGO, which correlates well with our electrochemical results. During the charge, the whole reactions are reversed so that the $Na_{15}Sn_4$ first de-alloys and reforms Sn metal. Then the Sn metal further reacts with Na_2S_2 to reconstruct the SnS_2 phase. Once again, the alloying and conversion reactions happen concurrently between 1.0 V to 1.5 V. With all the Na-Sn alloy phases transferring to Sn, the conversion reaction becomes the major reaction again, similar with the beginning of discharge. However, the SnS_2 phase that

formed at the final state of charge is no longer crystalline and becomes amorphous. The Raman spectra results suggest that the rGO also reacts reversibly with the Na-ions during this process, reflected by the reversible carbon D band and G band intensity ratio change. Although the detailed rGO mechanism is yet to be determined and the electrochemical data for rGO cycled in half cell shows insignificant reversible capacity, we believe that it is still a very interesting phenomenon. This result may inspire us to conduct further research on graphite based anode material for NIBs. Meanwhile, it is clearly demonstrated that rGO largely prevents particle agglomeration during electrochemical cycling, which helps with a complete and uniform consumption of SnS_2. Overall, the excellent electrochemical performance of the composite material should be mainly attributed to the synergistic mechanism of SnS_2, since it is the major active material for Na-ions storage. The fast kinetics of the alloy reactions solves the long term criticized problem of high voltage hysteresis and poor rate performance from conversion reaction. In return, better cycling performance can be achieved with the Na_2S_2 matrix, which solves the volume expansion problem caused by the alloying reactions. With the assistance of rGO, the unique conversion-alloying mechanism in SnS_2-rGO offers a well-balanced approach for sodium storage to deliver high capacity, long-cycle life, and superior rate capability. We believe that the nanocomposite materials design principles from this study can also be applied to other systems that involve both conversion and alloy reactions, such as SnO, Sb_2O_3, or SnS.

5.4. Conclusion

An in-depth understanding of the underlying relation between Na insertion/extraction mechanisms and electrochemical performances is essential to improve the performances of Na-ion batteries. In this work, a novel Na anode material, SnS_2-rGO, has been comprehensively investigated using SXRD, XAS, TEM, and Raman spectroscopy. The material demonstrates a capacity of 630 mAh g^{-1} with excellent capacity retention and rate performance. Contrary to what has been proposed in the literature, Na_2S_2 instead of Na_2S forms during the synergistic reaction, as confirmed by the XRD and SAED results. The interatomic distance change of Sn-Sn interaction in the EXAFS results indicates that Na-Sn alloy phases form during the discharge, while the SAED observations identify the alloy phase to be amorphous $Na_{15}Sn_4$. Highly amorphous SnS_2 forms after one full cycle, presumably due to the breakdown of pristine SnS_2 into Sn nanoparticles during the discharge. The synergistic mechanism that takes advantages of both conversion and alloying reactions ensures the high specific capacity, long cycle life and fast kinetics. The rGO allows for effective dispersion of the pristine SnS_2 particles and prevents the agglomeration of the nano-sized reaction products. Besides serving as a matrix to mitigate the mechanical strain, the rGO also reversibly reacts with Na-ion in the first cycle. Benefited from both synergistic effect and the assistance of rGO, highly efficient and durable sodium storage is achieved by this SnS_2-rGO anode in NIBs.

Chapter 5, in full, is a reprint of the material “Investigating the energy storage mechanism of SnS_2-rGO composite anode for advanced Na-Ion batteries” as it appears in the Chemistry of Materials, C. Ma, J. Xu, J. Alvarado, B. Qu, J. Somerville, J. Y. Lee, Y.

S. Meng, 2015, 27 (16), 563. The dissertation author was the primary investigator and author of this paper. All the experiment parts were performed by the author except for the Raman Spectra parts.

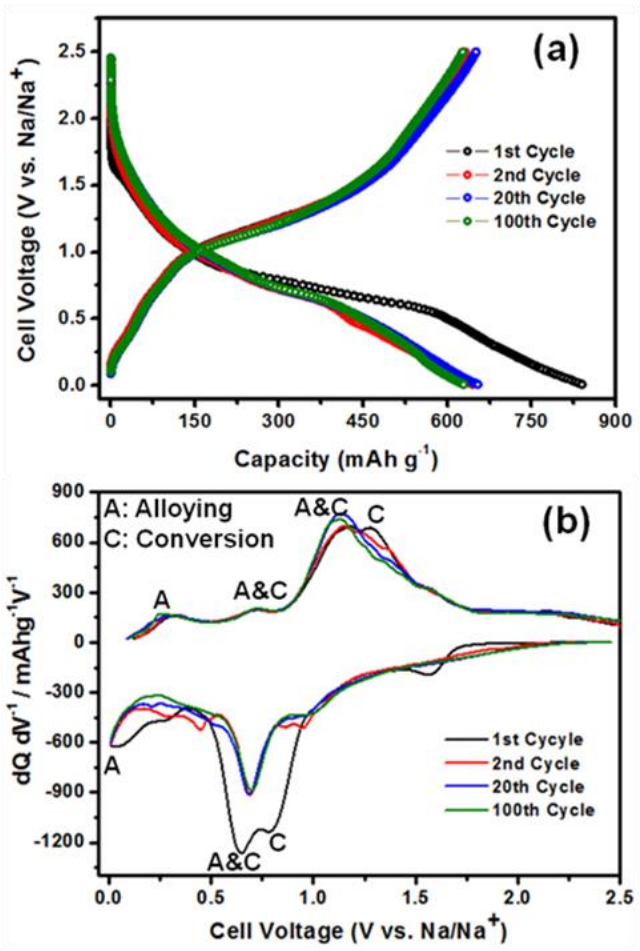

Figure 5.1. (a) Voltage profiles and (b) dQ dV^{-1} plots of SnS_2-rGO composite material.

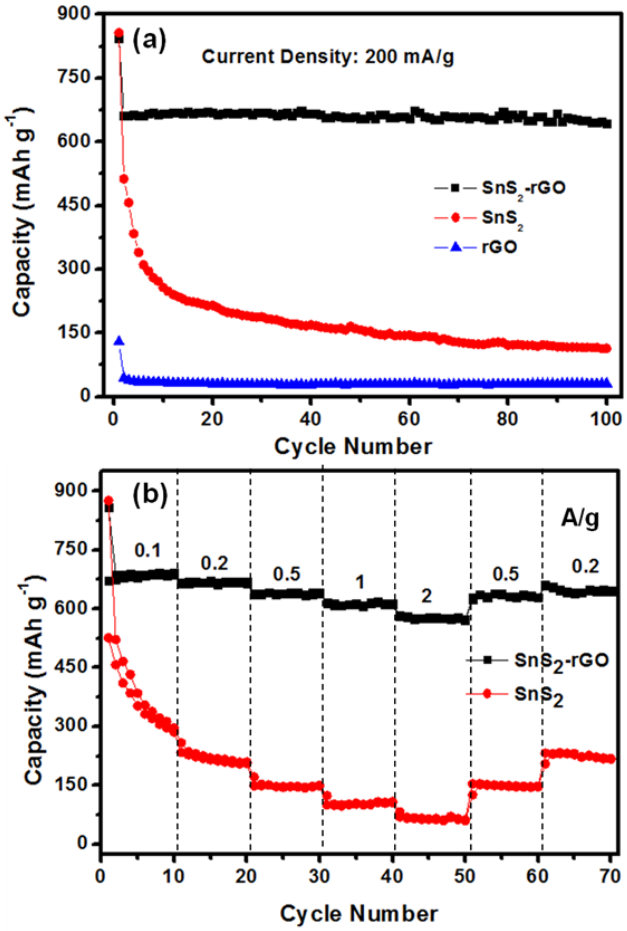

Figure 5.2. (a) Cycling performance of SnS_2-rGO, SnS_2 and rGO electrodes at 0.2 A g^{-1} for 100 cycles, respectively. (b) Rate performance of SnS_2-rGO and SnS_2 electrodes.

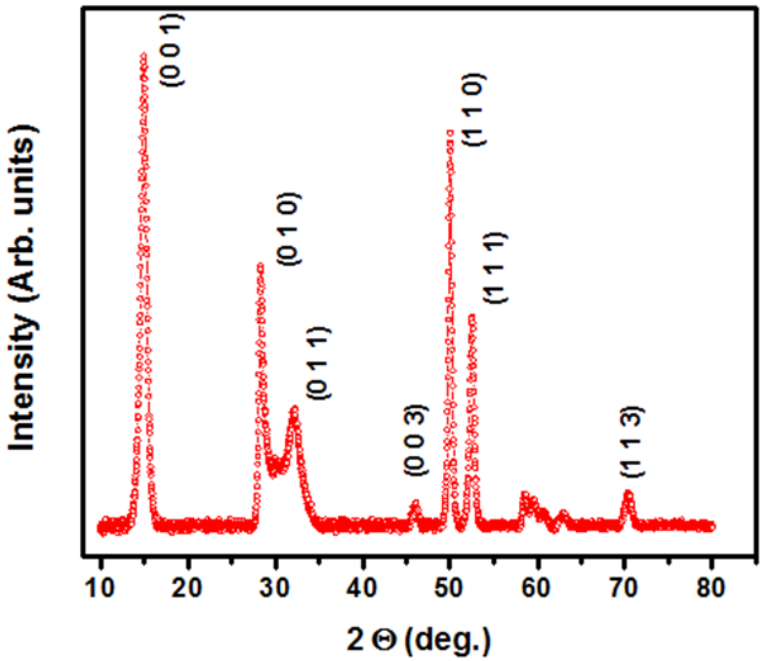

Figure 5.3. XRD for as-synthesized SnS_2-rGO.

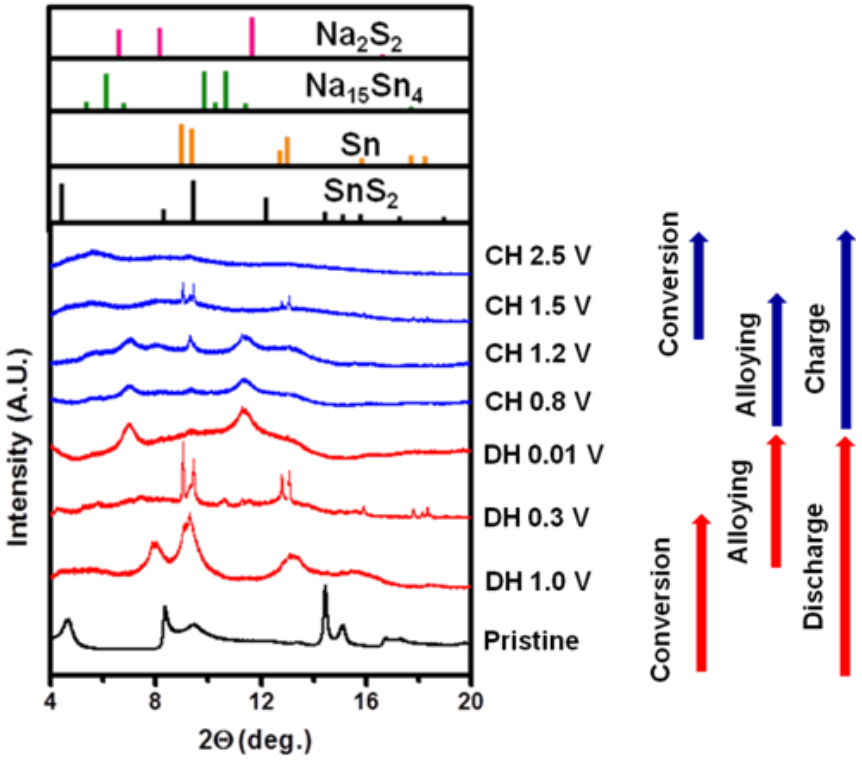

Figure 5.4. Synchrotron X-ray diffraction results of SnS_2-rGO electrodes at different discharge/charge states.

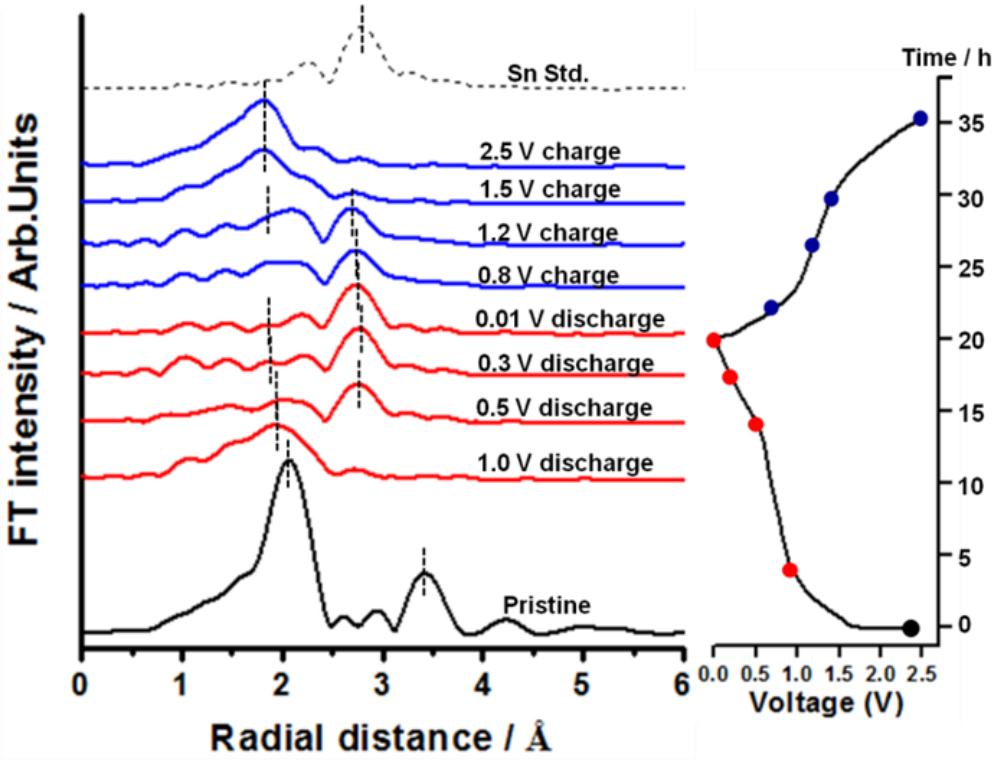

Figure 5.5. Sn K-edge EXAFS spectra of SnS_2-rGO electrodes at different voltages in the first cycle.

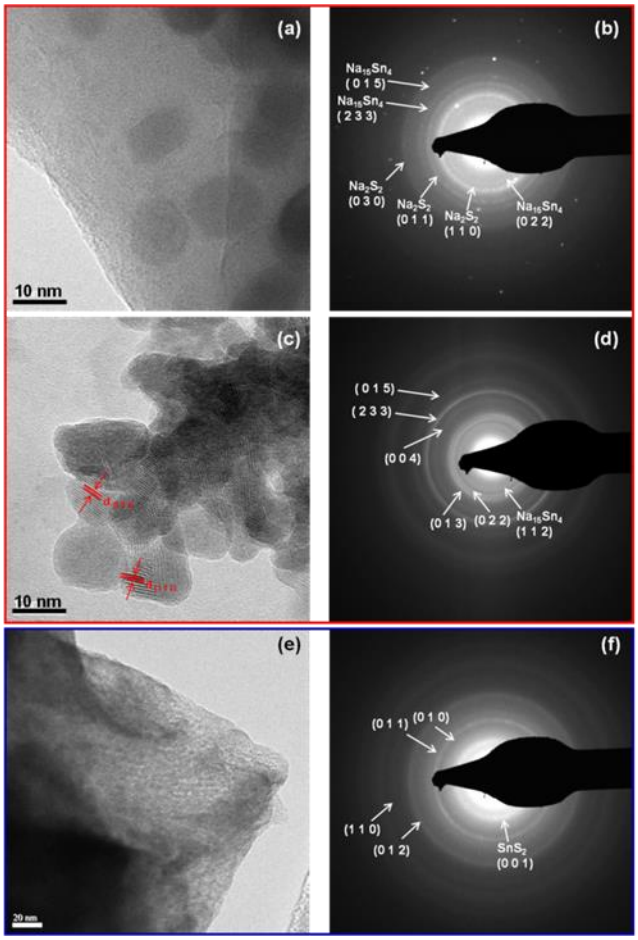

Figure 5.6. TEM and SAED results for (a)-(d) SnS_2-rGO electrode after 1st discharge (e)(f) SnS_2-rGO electrode after 1st charge.

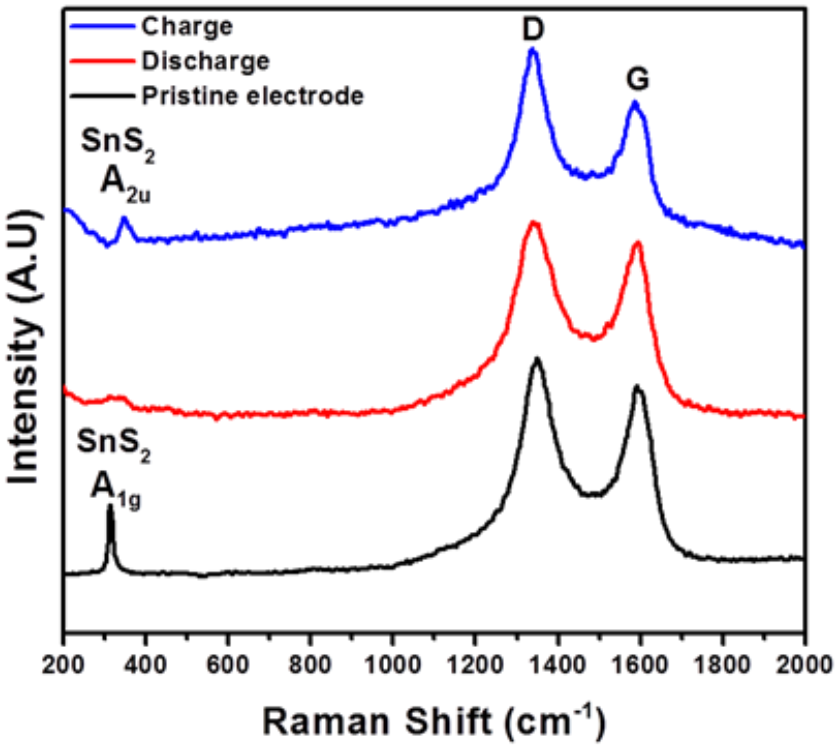

Figure 5.7. Raman spectra of SnS_2-rGO electrode at pristine state (black), after first discharge (red), and after charge to 2.5 V (blue).

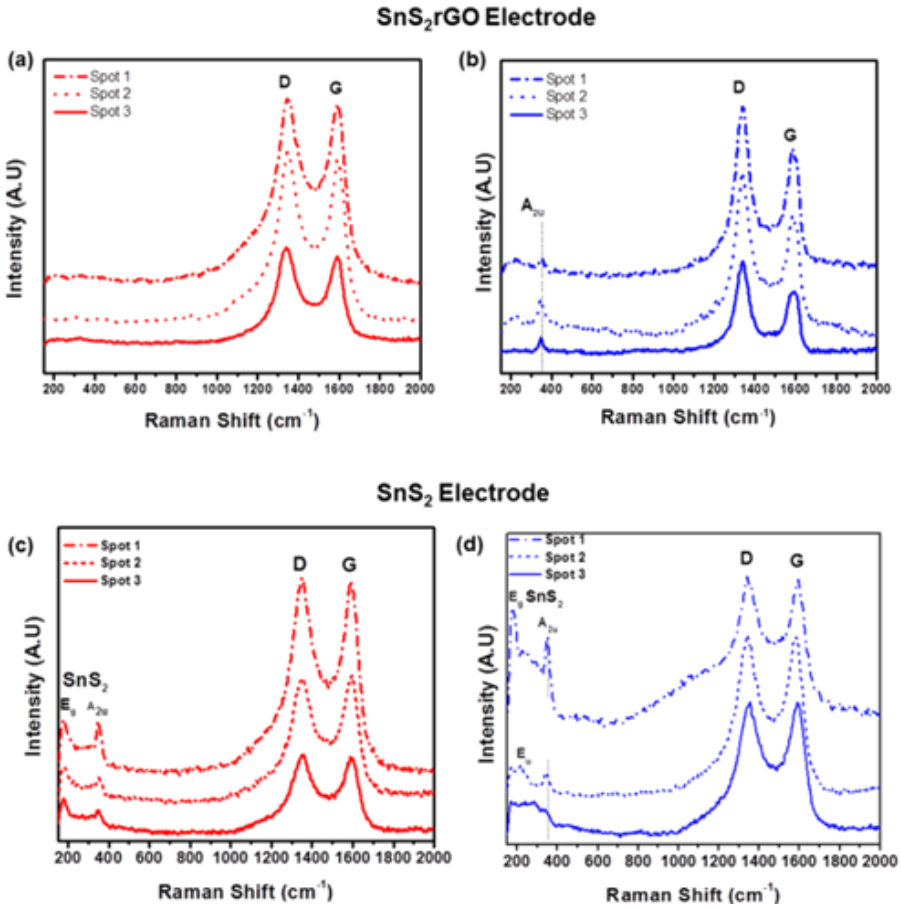

Figure 5.8. Raman spectra on different spots of SnS_2 electrodes with and without rGO. (a) SnS_2-rGO electrode at fully discharge. (b) SnS_2-rGO electrode at fully charge. (c) Bare SnS_2 electrode at fully discharge. (d) Bare SnS_2 electrode at fully charge.

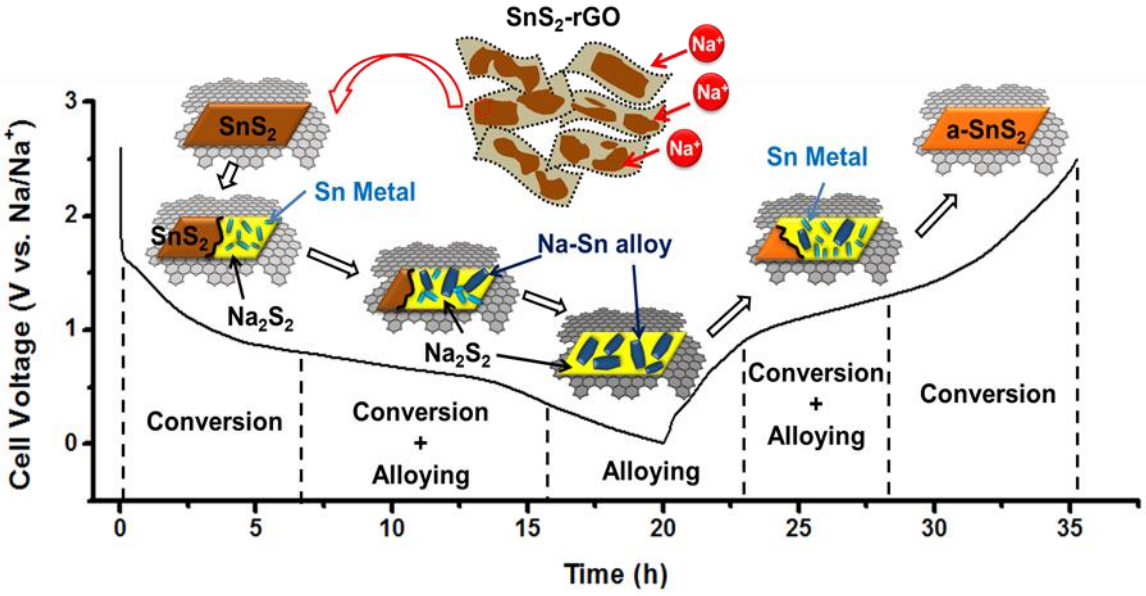

Figure 5.9. Schematic of the energy storage mechanism of SnS_2-rGO composite.

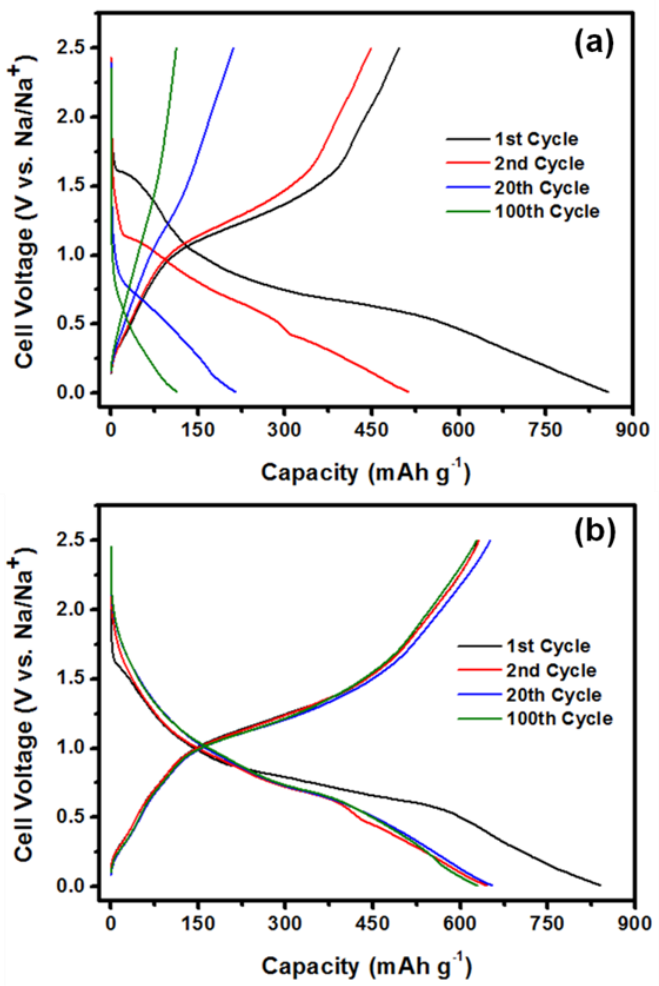

Figure 5.10. Voltage Profiles of (a) SnS_2 and (b) SnS_2-rGO.

Table 5.1. Raman vibration modes of peaks found in Figure 5.7

Sample	Vibration mode	SnS_2 (cm^{-1})	rGO (cm^{-1})	I_D/I_G
Pristine Electrode	D		1350.3	1.2
	G		1594.1	
	A_{1g}	314.8		
Discharge 0.01V	D		1343.2	1.02
	G		1594.1	
Charge 2.5 V	D		1351.6	1.3
	G		1598.1	
	A_{2u}	361.1		

Table 5.2. Raman vibration modes for SnS_2 found in Figure 5.8

Sample	Spot	Vibration mode	SnS_2 (cm^{-1})
Discharge 0.01 V	1-3	A_{2u}	348.5
		E_g	179.0
Charge 2.5 V	1	A_{2u}	349.8
		E_g	175.7
	2	A_{2u}	345.5
		E_u	221.2
		E_g	175.7
	3	-	-

Chapter 6. Exploring Oxygen Activity in the High Energy $Na_{0.78}Ni_{0.23}Mn_{0.69}O_2$ Cathode Material for Na-Ion Batteries

Large-scale electric energy storage is fundamental to the use of renewable energy. Recently, research and development efforts on room-temperature sodium-ion batteries (NIBs) have been revitalized, as NIBs are considered promising, low-cost alternatives to the current Li-ion battery technology for large-scale applications. Herein, we introduce a novel layered oxide cathode material, $Na_{0.78}Ni_{0.23}Mn_{0.69}O_2$. This new compound provides a high reversible capacity of 138 mAh g^{-1} and an average potential of 3.25 V vs. Na^+/Na with a single smooth voltage profile. Its remarkable rate and cycling performances are attributed to the elimination of the P2-O2 phase transition upon cycling to 4.5 V. The first charge process yields an abnormally excess capacity which has yet to be observed in other P2 layered oxides. Metal K-edge XANES results show that the major charge compensation at the metal site during Na-ion deintercalation is achieved via the oxidation of nickel (Ni^{2+}) ions, whereas, to a large extent, manganese (Mn) ions remain in their Mn^{4+} state. Interestingly, Electron Energy Loss Spectroscopy (EELS) and soft X-ray Absorption Spectroscopy (sXAS) results reveal differences in electronic structures in the bulk and at the surface of electrochemically-cycled particles. At the surface, transition metal ions (TM ions) are in a lower valence state than in the bulk, and the O K-edge pre-peak disappears. Based on previous reports on related Li-excess LIB cathodes, it is proposed that part of the charge compensation mechanism during the first cycle takes place at the lattice oxygen site, resulting in a surface to bulk transition metal gradient. We believe that by optimizing and controlling oxygen activity, Na layered oxide

material with higher capacities can be designed.

6.1. Introduction

The effective use of renewable energy is one of the most important issues that need to be addressed in order to achieve a sustainable society.[114] Renewable energy sources such as solar and wind energy do not produce electricity in a consistent manner, thus, a large-scale energy storage system is required to integrate the intermittent energy into a stable power supply that can meet consumption in real time. High-energy Li-ion batteries (LIBs) are expected to contribute to the solution; however, the expected increase in the cost of raw lithium, as compared to abundant and low-cost Na, has led to a resurgence of interest in room-temperature Na-ion batteries (NIBs) as potential, cheaper alternatives for large-scale applications. Furthermore, rechargeable NIBs share many similarities with LIBs, thus state-of-the-art LIB technologies can provide some direction and speed up progress in NIB research.

The easy synthesis of layered transition metal oxides, Na_xTMO_2 ($0 < x < 1$ and TM = transition metals), and their promising electrochemical properties, have resulted in a large number of recent reports on this family of NIB cathode materials.[37,115–127] In Na_xTMO_2, TM ions reside within layers of edge sharing metal-oxide (TMO_6) octahedra, while Na-ions are accommodated between the layers. The most common structures are O3- and P2-type, according to a classification devised by Delmas *et al.*, where Na-ions occupy octahedral (O) and trigonal prismatic (P) sites, respectively.[5] The number following the sodium coordination environment describes the number of TMO_2 layers in the unit cell. P2 and O3 structures differ in their oxygen stacking sequence, namely

ABCABC stacking for O3 and ABBA stacking for P2, leading to different electrochemical characteristics. On the one hand, O3-type materials are less structurally reversible when cycled above 4.0 V. Their rate performance is also lower because Na-ions need to diffuse through face-shared interstitial tetrahedral sites.[29,128] On the other hand, P2-type materials, as synthesized, contain Na-vacancies in the Na layers. Thus, when cycled vs. an Na metal anode (and a large Na-excess), an apparent first cycle coulombic efficiency of above 100% results, the discharged material containing fewer Na-vacancies. The large fraction of these unoccupied Na^+ ion sites in as-synthesized P2 materials leads to problems in terms of electrode balancing in full cells.[51] Moreover, P2-type materials undergo phase transitions at high voltage that result in shortened cycle life and poor rate capability.[129,130] Two approaches have been used to alleviate this issue, the first one being to limit the high voltage cutoff to 4.1 V to avoid the P2-O2 transition. In $Na_xMn_{2/3}Ni_{1/3}O_2$, this leads to an increase in capacity retention from 64% to over 95% after 10 cycles.[129] The second approach is to substitute Ni for an electrochemically inactive element, such as Li, to delay structural transitions at higher voltages. Li doping in this family of materials was first explored by Johnson and coworkers, who showed that the P2-$Na_{1.0}Li_{0.2}Ni_{0.25}Mn_{0.75}O_2$ cathode material displays a single smooth voltage profile up to 4.2 V, and excellent cycling and rate capabilities.[34] A following study from our group demonstrated that the Li-doped P2-$Na_{0.80}Li_{0.12}Ni_{0.22}Mn_{0.66}O_2$ maintains its structure up to 4.4 V and exhibits more than 95% of its initial capacity after 50 cycles.[35] The study determined that the presence of monovalent Li-ions in the TM layers allows more Na-ions to reside in the prismatic sites in the as-prepared material and upon charge. Thus, the phase transformation is delayed upon Na deintercalation, the P2 structure is retained in

the high voltage region, and the cycling performance is improved.

Despite a large number of recent studies on various Na layered oxide cathodes with different TM compositions, as discussed in a recent review paper,[131] there was rarely report on the redox activity of oxygen anions in NIB cathode materials. It is now widely accepted that the participation of both metal and oxygen ions in the redox reaction mechanism leads to high energy density in Li-excess LIB cathode materials.[132–137] This topic is of great relevance to the NIB community, as oxygen participation in the high voltage redox reactions could open up new perspectives for the design of high energy NIB cathodes. Only very few recent studies on Na_xTMO_2 materials have suggested the participation of oxide ions in the redox processes takes place upon Na electrochemical extraction, e.g., in P2-$Na_xM_yMn_{1-y}O_2$ (M = Li, Mg) cathode materials[138–140], and apart from Yamada and coworkers' work on $E(Ni^{3+}/Ni^{2+}) > E(Ni^{4+}/Ni^{3+})$ redox potential paradox,[141] little experimental evidence has been provided to confirm the contribution of O-based charge compensation phenomena to the observed capacity of the Na positive electrodes. Inspired by previous work by Dahn *et al.*, who showed that metal vacancies can facilitate oxygen atom reactivity in cathode materials,[142] we modified the stoichiometry of P2-$Na_xNi_yMn_zO_2$ to design a high Na content, TM-deficient, P2-$Na_{0.78}Ni_{0.23}Mn_{0.69}O_2$ compound. While the large Na-ion reservoir is expected to stabilize the P2 structure up to high voltage, the TM deficiency is expected to activate the oxygen anion redox in the Na layered oxide. The stoichiometry of the compound, $Na_{0.75}Ni_{0.24}Mn_{0.69}O_{1.99}$ (normalized to Mn), was determined by inductively coupled plasma-optical emission spectroscopy (ICP-OES) and confirmed by Ni/Mn K-edge XAS.

Herein, we report on the synthesis and characterization of the novel layered oxide

$Na_{0.78}Ni_{0.23}Mn_{0.69}O_2$. This material consists of a single P2 phase and performs very well as a high energy density rechargeable NIB cathode. The abnormally high capacity observed on first charge is thoroughly investigated. Long-range and short-range structural changes are monitored using *ex situ* XRD and solid-state Nuclear Magnetic Resonance (ssNMR). The participation of oxygen anions in the initial charge compensation mechanism is explored using EELS and XAS techniques.

6.2. Experimental

An appropriate amount of Na_2CO_3 (molar ratio of carbonate ions to transition metal ions is 1:1) was dissolved in 60 mL deionized water, then added dropwise to a 10 ml mixed solution of $Ni(NO_3)_2$ and $Mn(NO_3)_2$ (Ni : Mn = 1:3 in molar ratio) while stirring. Then the solution was transferred to a 100 mL Teflon-lined stainless steel autoclave and aged at 80 ℃ for 12 h, yielding $(Ni_{0.25}Mn_{0.75})CO_3$. The $(Ni_{0.25}Mn_{0.75})CO_3$ particles were mixed with a stoichiometric amount of Na_2CO_3 and the mixture was calcined at 900 ℃ for 12 h in a 50 ml porcelain crucible. The stoichiometry of the as-synthesized compound was determined by inductively coupled plasma-optical emission spectroscopy (ICP-OES), and the formula of $Na_{0.75}Ni_{0.24}Mn_{0.69}O_{1.99}$ (normalized to Mn) was confirmed. The morphology of the as-synthesized material was characterized by a Philips XL30 environmental scanning electron microscope (ESEM) operating at 10 kV.

Cathode electrodes were prepared by mixing 80 wt % active material with 10 wt % acetylene black and 10 wt % polyvinylidene fluoride (PVdF). A glass fiber GF/F (Whatman) filter was used as the separator and 1 M $NaPF_6$ in propylene carbonate (PC) was used as the electrolyte. Battery assembly was carried out in an MBraun glovebox

(H_2O < 0.1ppm). Galvanostatic discharge and charge at various current densities were performed on a Arbin BT2000 battery cycler. Additionally, electrochemical impedance spectroscopy (EIS) measurements were carried out with AC frequencies ranging from 0.01 to $1x10^6$ Hz on galvanostatically cycled electrodes stopped at various states of charge (open current voltage (OCV), 3.5 V, 4.1 V, 4.5 V) and discharge (3.5 V, 2.0 V). The electrodes were assembled in a three electrode Swagelok® cell, where the active material was the working electrode, Li metal served as the counter and reference electrode. The three electrode cells were then cycled as described earlier. The three-electrode configuration allows for proper isolation of the working electrode impedance. A Solatron 1287 Potentiostat was used to measure the impedance at different states of charge and discharge. An equivalent circuit model was fitted to the data to separate the impedance contributions from the various components of the cell using the Z view software (v. 3.4a, Scribner Associates, Inc.).

The samples characterized by XRD were obtained by disassembling the cycled batteries in an argon filled glovebox. The electrode materials were washed using battery grade dimethyl carbonate (DMC) three times, then stripped off from the aluminum current collectors. The powders from the cycled electrodes were then mounted in hermetically sealed capillary tubes for *ex situ* XRD measurements. Synchrotron powder diffraction patterns of all samples were collected at the Advanced Photon Source (APS) on beamline 11-BM (l = 0.459 Å). The beamline uses a sagittal focused X-ray beam with a high precision diffractometer circle and 12 independent analyzer sets, providing high sensitivity and resolution. XRD patterns were collected between -6.5° and 28.0° in 2θ angles.

^{23}Na ssNMR spectra were acquired at room temperature on a Bruker Avance III 200 wide-bore spectrometer (4.7 T external magnetic field) at a Larmor frequency of -53.0 MHz. All NMR experiments were performed under 60 kHz magic angle spinning (MAS) using a 1.3 mm double-resonance HX probe and a recycle delay of 30 ms. ^{23}Na NMR chemical shifts were referenced against solid ^{23}NaCl at 7.21 ppm. ^{23}Na spin echo NMR spectra were acquired using a 90 ° radiofrequency (RF) pulse of 1.03 μs and a 180° RF pulse of 2.06 μs at 25.04 W. Transverse (T_2') relaxation times were determined from an exponential fit of the decay of the signal intensity obtained as the echo delay was increased in an NMR spin echo pulse sequence. The NMR data were processed with a 1 kHz applied line broadening.

X-ray absorption spectroscopy measurements were performed on the 5-BM-D beamline at the Applied Photon Source (APS) at Argonne National Laboratory. Customized coin cells were used to prevent sample contamination. Measurements were performed at the Ni and Mn K-edge under transmission mode using a gas ionization chamber to monitor the incident and transmitted X-ray intensities. A third ionization chamber was used in conjunction with Ni and Mn foil standards to provide internal calibration for the alignment of the edge positions. The incident beam was monochromatized using a Si (111) double-crystal fixed exit monochromator. Harmonic rejection was achieved using a rhodium-coated mirror. Each spectrum was normalized using the data processing software package IFEFFIT. Soft XAS measurements were carried out on beamline 8-2 at the Stanford Synchrotron Radiation Laboratory. These measurements were conducted on powder samples pressed on Au foil to avoid contamination from the adhesive of the carbon tape. Data were acquired under ultrahigh

vacuum (10^{-9} Torr) in a single load at room temperature in total electron yield (TEY) mode via the drain current method, in Auger electron yield (AEY) mode using a cylindrical mirror analyzer, and in fluorescence yield (FY) mode using silicon photodiodes.

Electron Microscopy work was carried out on a Cs-corrected FEI Titan 80/300 kV TEM/STEM microscope equipped with a Gatan Image Filter Quantum-865. All STEM images and EELS spectra were acquired at 300 kV and with a beam size of ~0.7 Å. EELS spectra shown in this work were acquired from a square area of ~0.5*0.5 nm with an acquisition time of 3 s and a collection angle of 35 mrad. HAADF images were obtained with a convergence angle of 30 mrad and a large inner collection angle of 65 mrad. To minimize possible electron beam irradiation effects, EELS and HAADF figures presented in this work were acquired from areas without prebeam irradiation. Mn L3 to L2 intensity ratio analysis was performed using the method described by Wang et al.[143]

6.3. Results and Discussion

6.3.1. Electrochemical Properties of $Na_{0.78}Ni_{0.23}Mn_{0.69}O_2$

The morphology of the as-synthesized $Na_{0.78}Ni_{0.23}Mn_{0.69}O_2$ particles was characterized by scanning electron microscopy (SEM), as shown in Figure 6.1. The primary particle size is around 3 μm. Electrochemical tests were conducted without further material optimization. The electrode active material load was approximately 3 mg/cm^2. Figure 6.2 (a) shows the galvanostatic charge/discharge voltage profiles of the $Na_{0.78}Ni_{0.23}Mn_{0.69}O_2$ electrode during the 1st, 2nd, 3rd, 4th, 5th, 10th, and 20th cycles, at 0.1 C cycling rate. The material delivers a reversible first cycle capacity of 138 mAh g^{-1}

when cycled between 2 - 4.5 V, with a low coulombic efficiency of 75%. In subsequent cycles, the plateau above 4.1 V vanishes and the coulombic efficiency increases to 97%. The differential capacity ($dQ\ dV^{-1}$) vs. voltage plots shown in Figure 6.2 (b) clearly reveal that the long high voltage plateau is irreversible upon cycling. Of note, the 180 mAh g^{-1} first charge capacity (equivalent to the removal of 0.66 Na per formula unit) is significantly higher than the theoretical value of 121 mAh g^{-1} calculated on the basis of the Ni^{2+}/Ni^{4+} redox change. In addition, the long plateau between 4.1 and 4.5 V indicates a high voltage reaction pathway different from the one observed in the low voltage region (2.0 - 4.1 V). As shown in Figure 6.3, the behavior in the low voltage region remains unchanged over a large range of applied current densities (12 to 300 mA g^{-1}); on the other hand, the high voltage plateau shortens significantly at higher charging currents, indicating that this high voltage reaction is kinetically slow. Figure 6.2 (c) shows the voltage profiles of the $Na_{0.78}Ni_{0.23}Mn_{0.69}O_2$ electrode discharged at different current rates, ranging from 0.1 C to 5 C. The material still provides a high reversible capacity of 120 mAh g^{-1} at a 5 C discharge rate, corresponding to approximately 87% of the capacity observed when cycled at a lower rate of 0.1 C. This performance is among the best reported thus far for Na layered oxide materials.[131] Figure 6.2 (d) shows the cycling performance of the $Na_{0.78}Ni_{0.23}Mn_{0.69}O_2$ cathode when charged and discharged at various current rates. A 0.1 C cycling (charge/discharge) rate was initially applied and progressively increased, as indicated on the figure. The discharge capacity is close to 125 mAh g^{-1} after ten cycles. An increase in the current density from 0.2 C to 0.5 C, and then to 1.0 C, results in negligible capacity decrease. Even after a 100-fold current density increase (10 C), the discharge capacity is still 75 mAh g^{-1}, which is 60% of the total

capacity cycled at 0.1 C. After setting the current density back to 0.1 C, the material exhibits a capacity of 124 mAh g^{-1}, exceptionally close to the initial capacity. The high capacity retention discussed above attests to the resilience of the P2-$Na_{0.78}Ni_{0.23}Mn_{0.69}O_2$ material to harsh cycling conditions, and to fast Na-ion diffusion in the structure.

To investigate the origins of the first charge excess capacity further, electrochemical impedance spectroscopy (EIS) experiments were conducted on the P2-$Na_{0.78}Ni_{0.23}Mn_{0.69}O_2$ electrode using a three electrode Swagelok T-cell®. This configuration allows for proper impedance isolation of the working electrode, while eliminating the effects of the Na metal counter electrode.[144] The material was cycled to a specific state of charge (SOC) and allowed to reach equilibrium (2 hr rest) before the acquisition of impedance data. After each impedance measurement, the cell was cycled to the next voltage step and the process was repeated. Figure 6.4 (a) shows the Nyquist plots of the working electrode at 3.5 V, 4.1 V, 4.5 V, and after a second charge to 4.5 V. Upon electrochemical cycling, the electrode experiences a series of processes in the bulk and at the surface, resulting in different suppressed semicircles in the Nyquist plots shown in Figure 6.4. An equivalent circuit is required to fit the data at different SOCs and deconvolute the impedance response into the various components of the electrochemical cell. The model accounts for the ohmic resistance of the electrolyte (R_Ω), the double layer capacitance of the electrode/electrolyte interface (CPE_f), the resistance due to irreversible side reactions (R_f), the charge transfer resistance (R_{ct}), and the solid state diffusion impedance also known as the Warburg impedance (Z_w).[144–147] Electrochemical parameters associated with the equivalent circuit are summarized in Table 6.1. As expected, R_Ω does not change significantly upon electrochemical cycling. Below the

plateau region (< 3.5 V), the combined resistance of the two suppressed semicircles is 184.5 Ω. At 4.1 V, there is a slight increase in R_f due to electrolyte decomposition. Over the long voltage plateau, between 4.1 to 4.5 V, the charge transfer resistance increases significantly as a result of the formation of a solid electrolyte interphase (SEI) layer and properties of the particle surface (140.4 Ω to 260 Ω, respectively). A similar increase was observed in a number of Li-excess cathode materials[146,147] As mentioned earlier, the long high voltage plateau contributes to the excess capacity in the first cycle but does not persist in the following cycles (see Figure 6.2). The EIS spectra obtained on first and second charge are also very different: the total cell resistance upon second charge is significantly lower (165.7 Ω) than the resistance observed upon first charge (290.1 Ω), the latter resulting from irreversible surface reactions and structural reorganization during the initial charging process.

6.3.2. Structural Evolution of the $Na_{0.78}Ni_{0.23}Mn_{0.69}O_2$ Electrode upon Cycling

As reported in earlier work, Ni- and Mn-containing layered oxide cathode materials are prone to P2/O2 phase transformations upon charge above 4.2 V. The P2 phase is reversibly generated upon subsequent discharge to 2.5 V.[119,129] Although fast Na-ion diffusion can be achieved in the initial P2 phase, the high voltage phase transformation is detrimental to the electrochemical performance of the cathode and inevitably leads to poor rate and cycling capabilities. By limiting the cutoff voltage to 4.1 V the cycling performance can be largely improved, yet at the expense of more than 40% of the total capacity.[129] The excellent electrochemical properties of the

$Na_{0.78}Ni_{0.23}Mn_{0.69}O_2$ electrode suggest that the bulk structure stays P2 and exhibits good Na-ion diffusion properties upon removal of 0.66 Na per formula unit.

Structural changes in the $Na_xNi_{0.23}Mn_{0.69}O_2$ electrode during electrochemical cycling were monitored by analyzing samples stopped at different states of charge (SOCs) using *ex situ* synchrotron XRD. Lattice parameters were obtained from Rietveld refinements of the XRD patterns. As shown in Figure 6.5 (a), the XRD pattern of the pristine sample is well indexed in the hexagonal space group $P6_3/mmc$, confirming that the as-synthesized material is P2-type and phase pure. Besides, as observed in similar layered materials,[35,148] a small concentration of stacking faults is expected in this compound, causing unconventional peak profiles which will be discussed in detail later. The XRD patterns of the partially charged (4.1 V) and fully charged (4.5 V) samples can also be fitted in the $P6_3/mmc$ space group (Figure 6.6), demonstrating that the overall P2 crystal structure is maintained upon Na extraction. The a lattice parameter, dominated by the TM-TM distance, decreases upon charge, as expected from the increase in the average Ni oxidation state, resulting in a shift of the (1 0 0) peak to higher angles. On the other hand, the c lattice parameter increases significantly, as demonstrated by clear shifts of the (0 0 2) and (0 0 4) peaks (see Figure 6.5 (a)), and of the (1 0 *l*) and (1 1 *l*) peaks (see Figure 6.5 (b) & (c)), to lower angles. The screening effect of Na-ions in the interlayer space becomes less effective, and Coulombic repulsion between successive O layers increase upon Na deintercalation. However, electrostatic effects are not sufficient to account for the drastic increase in c lattice parameter upon charge, from 11.128 Å to 14.224 Å. Previous studies on Na_xTMO_2 cathodes have speculated that solvent molecules, as well as salt ions, can insert between the TMO_2 layers upon Na removal.[29,148–150]The

interlayer distance at 4.5 V charge, around 7 Å, is close to the values obtained for the high voltage phases in these previous reports, suggesting that Na-ion removal from P2-$Na_{0.78}Ni_{0.23}Mn_{0.69}O_2$ leaves the crystal structure vulnerable to the insertion of solvent molecules. Lower XRD peak intensities are observed upon Na deintercalation, especially for the fully charged (4.5 V) sample. Moreover, the patterns shown in Figure 6.5 (b) & (c) reveal a broadening of the XRD peaks at high voltage, which may indicate that O2 stacking faults are formed in the electrode material.[35] The XRD pattern and lattice parameters obtained for the fully discharged sample are very similar to those obtained for the pristine material, indicating good structural reversibility upon Na reinsertion. Based on these observations, it is speculated that the larger Na content of x = 0.78 in the as-synthesized material, as compared with conventional P2-type materials with a Na content of x = 2/3, prevents oxygen layer shifts and stabilizes the P2 framework, leading to the excellent performance shown in Figure 6.2.

While XRD probes long-range structural order, NMR gives insight into local structural changes in the material upon cycling. ^{23}Na NMR spectra were acquired on as-synthesized $Na_{0.78}Ni_{0.23}Mn_{0.69}O_2$ and at different SOCs during the first cycle (Figure 6.7). The major resonance at ca. 1400 ppm in the pristine spectrum is an average signal resulting from fast Na-ion motion (on the NMR timescale) between edge and face sharing prismatic sites in the structure, as reported in our recent NMR study on related P2-$Na_x[Li_yNi_zMn_{1-y-z}]O_2$ ($0 \leq x, y, z \leq 1$) materials.[148] This average Na resonant frequency gradually decreases to ca. 1200 ppm at 4.1 V SOC, and to ca. 1000 ppm at 4.5 V SOC, as expected from Ni oxidation, and the reduction of the number of unpaired electrons centered on the nickel ions (from two for Ni^{2+} to none for Ni^{4+}).[148] An additional NMR

peak is present at ca. 300 ppm at 4.1 V, and at ca. 200 ppm at 4.5 V. These Na signals are attributed to Na environments created upon water intercalation into the Na deficient layers, on the basis of prior work on related materials.[148] The low resonant frequencies resulting from the expanded layers, longer TM-O-Na bonds, and weaker TM-Na interactions.[148] The integrated area under the low frequency peaks reveals that Na-ions in hydrated layers represent less than $1/10^{th}$ of all 0.1 Na left in the material at 4.5 V; this is a much lower proportion than what was previously observed in similar materials,[148] suggesting little water uptake in the *ex situ* (charged) samples. The NMR signal assigned to the average prismatic Na environment remains highest in intensity throughout cycling, which testifies of a highly stable P2 structure upon Na extraction and is consistent with XRD results. The major peak shifts back to ca. 1400 ppm in the fully discharged state, clearly demonstrating the reversibility of the P2 structure upon Na extraction and reinsertion. Overall, XRD and ^{23}Na NMR results demonstrate that the long-range P2 structure of the $Na_{0.78}Ni_{0.23}Mn_{0.69}O_2$ cathode material is stable and that local structural order is recovered upon cycling. As calculated from the first charge capacity, the amount of Na left in the structure at 4.5 V is around 0.12 Na per formula unit. The residual Na-ions are critical to maintain structural stability. The changes observed in the long- and short-range structure upon electrochemical cycling do not account for the large excess capacity observed during the first charge. Therefore, redox reactions taking place in the material were examined in more detail using *in situ* XAS.

6.3.3. Bulk Electronic Structure Study using *in situ* XAS

The evolution of the electronic structure and variations in the nickel and manganese local environments during the first cycle were investigated with *in situ* X-ray absorption spectroscopy (XAS) (Ni, 8333 eV; Mn, 6539 eV). In particular, time-resolved information on the Ni valence state is crucial to unveil the redox reaction mechanisms taking place upon electrochemically cycling the material. Comparing the standard references, NiO and MnO_2, to XAS data obtained for as-synthesized $Na_{0.78}Ni_{0.23}Mn_{0.69}O_2$, it is evident that the pristine material predominantly consists of Ni^{2+} and Mn^{4+} ions (Figure 6.8 (a) and (d)). The Ni K-edge shifts to a higher energy region upon charge, indicating that Ni^{2+} is oxidized. The energy shift at 4.5 V is ~4 eV, which is much larger than the shift expected for the Ni^{2+}/Ni^{3+} redox change (~2 eV, Figure 6.9), suggesting that the oxidation state of Ni is close to Ni^{4+}.[148,151] The inset of Figure 6.8 (a) reveals that most of the energy shift of the Ni K-edge takes place below 4.1 V, while a minor energy shift is observed between 4.1 V and 4.5 V. These results indicate that, to a large extent, the Ni charge transfer reaction takes place in the lower voltage region. Upon subsequent discharge to 2.0 V, Ni ions are reduced back to their divalent state, demonstrating that the Ni redox reaction is completely reversible.

Ni EXAFS results are shown in Figure 6.8 (c), where the two shells at 1.4 Å and 2.6 Å represent the Ni-O interaction and Ni-TM interaction, respectively. As Ni^{2+} is oxidized to Ni^{4+}, both the Ni-O and Ni-TM interatomic distances decrease. These changes account for the a lattice parameter decrease observed in the XRD patterns upon charge. The variations in Ni-O and Ni-TM bond lengths are fully reversible upon subsequent discharge, and the interatomic distances ultimately return to their original values.

In contrast, Mn ions show only a minor participation in the electrochemical charge transfer reaction and remain essentially all Mn^{4+} (Figure 6.8 (d) and (e)). Figure 6.8 (f) reveals a slight change in the Mn-TM bond distance in the fully charged state, presumably resulting from the shorter bond lengths around the Ni^{4+} ions. Trace amounts of Mn^{3+} are present in the fully discharged sample, as evidenced by the slight shift of the Mn K-edge towards lower energies, as compared with the pristine state. This phenomenon will be discussed in a later section. Overall, it is clear that tetravalent Mn ions are electrochemically inactive and their main function is to stabilize the layered structure. On the other hand, Ni^{2+} / Ni^{4+} is the major redox active couple. Given that most of the Ni^{2+} / Ni^{4+} redox occurs below 4.1 V on charge, a different charge transfer mechanism must contribute to the capacity in the high voltage plateau region, between 4.1 and 4.5 V. The tetravalent Mn-ions are inactive, giving rise to the hypothesis that the lattice oxygen participates in the high voltage charge compensation process; these observations are similar to those previously observed in lithium-excess cathode materials for LIB systems,[132,152] where considerable work has been performed to test this hypothesis. To explore this further, the EELS and soft XAS techniques are used here to investigate the electronic structure of the TM-O ligand in the material.

6.3.4. Surface and Bulk Characterization by EELS and Soft XAS

STEM coupled with EELS was employed to study the evolution of the surface structure of electrochemically-cycled $Na_xNi_{0.23}Mn_{0.69}O_2$ particles. Electron microscopy data obtained on the as-synthesized material and on samples after initial charge are shown in Figure 6.10. The layered structure of the P2 material is clearly observed along

the [0 1 0] zone axis of the pristine particle (Figure 6.10 (a)). The bright dots indicate the lighter element (here Na), while the dark dots represent the heavier TM ions. Stacking faults and defects, indicated with red circles, are also observed in the pristine material. The presence of structural defects makes it difficult to acquire high resolution STEM images, because atoms are not perfectly aligned along a single direction (Figure 6.10 (c)). The HRTEM image shown in Figure 6.10 (b) was obtained on a cycled particle along the [0 0 1] zone axis. An amorphous SEI layer around 3-5 nm thick is observed at the surface of the particles. A large number of defects are also present in the bulk of the cycled particles, resulting in blurry high resolution STEM images.

Figure 6.11 (a) & (b) compare the EELS spectra obtained at the O K-edge and at the Mn L-edge for pristine and cycled particles. The evolution of the fine structure and energy position of the O-K and Mn-L edges gives insight into electronic structure changes taking place in the material upon cycling. The Mn L-edge energy positions and fine structures are nearly identical at the surface and in the bulk of pristine particles, as well as in the bulk of cycled particles. At the surface of cycled particles, however, the Mn-L edge moves to slightly lower energy, suggesting a decrease in the average Mn oxidation state. In addition, the higher L3/L2 ratio, indicative of the TM oxidation state, is further evidence for a lower Mn oxidation state at the particles' surface.[143] Differences in the O K-edge fine structure are observed between the spectra obtained at the surface of cycled particles and those collected on pristine particles. The first peak at an energy loss of 532 eV (indicated with a dashed line) almost vanishes in the spectra obtained at the surface of cycled particles. This oxygen pre-peak can be attributed to the electronic transition from the 1s core state to the O 2p - TM 3d hybridized states. The decrease in

intensity of this peak at the surface of cycled particles indicates fewer holes in the 2p-3d hybridized orbitals, meaning that surface TMs are in a lower valence state. Moreover, EELS spectra obtained from a single particle at different surface depths (from surface to bulk) reveal a gradient of TM valence states, as depicted in Figure 6.12.

Similar distributions of TM oxidation states across particles, oxygen vacancies formed at or near the surface of the particles, and variations between bulk and surface electronic structures, have been extensively reported in Li-excess LIB cathodes.[147,153,154] Different models have been proposed to describe the electronic and structural phenomena upon charge, such as the transition state theory model and the metal densification model.[153,155] Although the exact reaction mechanisms are still under debate, it has been widely recognized that these transitions are associated with lattice oxygen evolution occurring at high voltage charge compensation. Here, the similar electronic structure changes observed on the cycled $Na_xNi_{0.23}Mn_{0.69}O_2$ particles, as in Li-excess cathodes, strongly suggest that lattice oxygen in the P2 material participates in the charge compensation mechanism at high voltage. While the details of interactions between TMs and oxygen vacancy are still unclear for Na P2-type structures, the present study proves that oxygen-based redox processes can contribute to the observed capacity in NIB layered oxide cathodes. The ensemble-averaged sXAS technique is employed to confirm this statistically.

Soft XAS (sXAS) is capable of probing chemical environments with excellent surface depth sensitivities by tuning the signal acquisition mode. Specifically, sXAS data can be collected simultaneously using three detection modes: (1) Auger electron yield (AEY), (2) Total electron yield (TEY), and (3) Fluorescence yield (FY). Electron yield

modes vary in penetration depth and are extremely surface sensitive: TEY mode has a probing depth of 2-5 nm, whilst AEY has a probing depth of 1-2 nm. The FY mode probes the bulk of the material up to a depth of about 50 nm.[52] Given its impressive capabilities, this characterization technique has been applied to investigate charge compensation mechanisms in LIB cathode materials, proving particularly useful in the exploration of redox reaction mechanisms involving oxygen anions in relation to those involving TM ions.[52,53] Here, it was used to further test the hypothesis of oxygen activity in our NIB cathode material.

X-ray absorption peaks corresponding to the metal L3- and L2-edges are relatively intense because the 2p-3d transition is electric dipole-allowed. In addition, these peaks are very sensitive to oxidation state, spin state, and bond covalence. The most salient electronic structure can be qualitatively obtained by deconvoluting the L3-edge into high-energy ($L3_{high}$) and low-energy ($L3_{low}$) features. Of note, the ratio between the $L3_{high}$ and $L3_{low}$ integrated peak intensities is in a positive relationship with the TM oxidation state.[54]

The Ni L-edge spectra obtained in FY mode for the *ex situ* samples collected during the first cycle are shown in Figure 6.13 (a). The pristine spectrum clearly demonstrates that Ni is in its divalent state, the split L3-edge feature being consistent with previous reports.[37,156,157] The bulk Ni oxidation state increases and decreases upon charge and discharge, respectively, in good agreement with the *in situ* XAS data discussed earlier. The average Ni oxidation is close to Ni^{4+} at the end of charge, though a slightly self-discharge might happen given the high voltage of the ex-situ cell.[158] Ni L-edge data collected on the fully charged electrode using the three different detection modes are

compared in Figure 6.13 (b). A clear decrease in the nickel oxidation state is observed from the bulk to the surface of the charged $Na_xNi_{0.23}Mn_{0.69}O_2$ particles, as evidenced by the gradual decrease in the $L3_{high}$ to $L3_{low}$ ratio when going from FY to TEY, to AEY mode.[157] As discussed earlier, a number of reports on lithium-excess cathode materials have shown that surface structural changes and TM redistribution give rise to TM oxidation state gradients within the particles.[52,159,160]

Pre-edge peak positions and intensities in the ligand K-edge XAS spectra provide important structural information on the chemical bonding between ligand and metal atomic species. The O K-edge XAS of electrochemically-cycled $Na_xNi_{0.23}Mn_{0.69}O_2$ is shown in Figure 6.13 (c). The pristine O K-edge XAS spectra can be divided into two regions. Pre-edge peaks below 535 eV are attributed to electronic transitions from the O 1s state to the O 2p - TM 3d hybridized state. On the other hand, the broad peaks above 535 eV correspond to transitions to O 2p - TM 4sp hybridized states.[161] In general, the 2p - 3d hybridized band can be further divided into a lower energy peak around 529.8 eV, corresponding to the t_{2g} band, and a higher peak around 532.2 eV, corresponding to the e_g band. The peak around 534.0 eV is associated with some sodium oxides or carbonaceous components that exist on the surface of the active material particles.[162] Since the density of the empty bound state in the molecular energy level is related to the hybridization of the O 2p - TM 3d orbitals, the integrated pre-edge peak intensity gives key information on the average hole state distribution and the average effective charge on oxygen anions.[53,160] The increase in the pre-peak intensity observed upon charge is consistent with Ni L-edge FY results: Ni oxidization creates more holes in the 2p - 3d hybrid orbitals, resulting in an increase in the O pre-peak in FY mode. On the other hand, the

smaller pre-peak in the O TEY spectra demonstrates that 2p - 3d orbitals on the particles' surface have more electrons, especially in the antibonding e_g orbital. This is a clear indication that TM ions are in a lower valence state at the surface, in agreement with the Ni TEY and AEY results.

As observed for Li-excess cathode materials, TM oxidation state gradients associated with lattice oxygen charge compensation processes are expected to take place concurrently with structural and electronic phenomena at the surface of the particles.[147,153] For the fully discharged sample, the intensity of the O pre-peak is lower in TEY mode than in FY mode, presumably due to irreversible structural changes at the surface of electrode particles during the charging process. Although O K-edge spectra were also acquired in AEY mode, the peaks assigned to the active material were largely masked by peaks from O-containing residual electrolyte and SEI components. Mn L-edge TEY results are shown in Figure 6.13 (d). A slight decrease in the Mn oxidation state is observed upon cycling. In fact, the Mn L-edge spectra collected on charge and discharge are similar to those obtained for Mn in Li spinel structures, where Mn was shown to be reduced at the surface[160].

Overall, the sXAS results presented in this section are complementary to the EELS results presented earlier. The bulk to surface TM valence state gradient observed for electrochemically-cycled particles suggests that lattice oxygen redox processes take place upon charge. In addition, sXAS data provide clear evidence for electronic and structural changes at the surface of the particles. The excess capacity and high surface resistance observed during the initial charge process presumably result from a reaction mechanism comparable to that reported for Li-excess LIB cathodes.

6.3.5. Exploring Oxygen Activity in a Na Cathode Material

In Li-excess oxide cathode materials, the participation of oxygen anions in the charge compensation mechanisms upon electrochemical cycling results in a remarkably high capacity, and this family of compounds is currently under intense scrutiny for the development of next generation Li batteries.[132] The similar physicochemical properties of Na and Li have encouraged us to design a Na layered TM oxide that displays oxygen anion redox activity comparable to that observed for Li-excess LIB cathodes. In this study, we showed that the $Na_{0.78}Ni_{0.23}Mn_{0.69}O_2$ cathode delivers a first charge capacity of 180 mAh g^{-1} and discharge capacity of 138 mAh g^{-1}, which are both higher than the theoretical capacity of 121 mAh g^{-1}. The charge compensation mechanism was carefully studied using a number of advanced characterization techniques. As shown in Figure 6.14, the Ni^{2+} to Ni^{4+} redox couple is active over the potential slope region, extending from the open current potential (OCV) to 4.1 V during the first charge, while oxygen anions are involved in the charge compensation mechanism over the high voltage plateau. The plateau region accounts for 60 mAh g^{-1} of excess capacity on first charge. The lattice oxygen reaction is concurrent with the formation of a surface to bulk TM oxidation state gradient, as well as with structural transformations at the surface of the cycled particles. Yet the high voltage oxygen redox processes in this material are not as reversible as in Li-excess compounds; the present work clearly proves that oxygen charge compensation can take place in P2-type Na cathodes.

It is speculated that the particular Na to TM ratio in the cathode material of interest to the present study is the cause for oxygen reactions. The stoichiometry of the compound, $Na_{0.75}Ni_{0.24}Mn_{0.69}O_{1.99}$ (normalized to Mn), was determined by ICP-OES and

confirmed by Ni/Mn K-edge XAS. In addition, ^{23}Na NMR indicated that all Na-ions are located in the prismatic layers. Therefore, seven percent of vacancies per formula unit are expected in the transition metal layer, introducing defects in the pristine material. As shown in Figure 6.15 (a)(b), the (1 0 *l*) XRD peaks are much broader than the (*h* 0 0) and (0 0 *l*) peaks, the latter two being normal and parallel to the metal planes, respectively, suggesting the existence of through-plane stacking faults in the pristine material;[32] this is also supported by HRTEM data in Figure 6.10 (a). The effect of TM vacancies is reflected by the Ni/Mn K-edge EXAFS (Figure 6.15 (c)(d)). Comparing with a previous sample ($Na_{0.8}Li_{0.12}Ni_{0.22}Mn_{0.66}O_2$), in which the TM sites are fully occupied,[35] the relative intensity of the peak resulting from the TM-TM interaction is slightly smaller for the current compound indicating fewer TM ions in the 1st cation coordination shell surrounding both Ni and Mn. Fitting of EXAFS spectra is complicated by the presence of these through-plane stacking faults in the pristine $Na_{0.75}Ni_{0.24}Mn_{0.69}O_{1.99}$ material, resulting in large σ^2 and E_0 values (Table 6.2).

Previous work by Dahn *et al.* on a lithium layered oxide containing TM vacancies showed that high irreversible capacity was associated with oxygen release. At the time, no clear mechanism was proposed to explain this phenomenon. Two more recent studies by Bruce *et al.*[136] and Ceder *et al.*[137] provided insights into the potential mechanisms leading to O participation in the redox processes which may also apply to the present study. In Li-excess materials, part of the Li^+ removed upon charge can be compensated by the formation of localized electron holes on the O atoms. The requirement for O redox is to have an essentially unhybridized 2p orbital on O, which is only possible in the case of highly ionic bonding (e.g. in Li-O-Li configurations). Extending the above argument

to compounds featuring vacancies in the TM layer, either a Li-O-Vacancy or Na-O-Vacancy configurations can potentially also fulfill this requirement. We tentatively suggest that electrons from O atoms in these ionic environments can participate in the charge compensation during delithiation/desodiation and contribute to the excess capacity observed during the charge process. As noted, the localized electron holes on oxygen render the oxygen unstable and susceptible to elimination from the lattice. Whether oxygen loss or oxygen redox chemistry dominates relies on the stability of the oxidized lattice O atoms in the crystal structure. In this particular P2 structure, due to the larger interlayer repulsion of AA stacking, it is likely that oxygen vacancies form in the high voltage plateau region, causing irreversible capacity during the first cycle. Work is ongoing to understand the detailed oxygen reaction mechanism in layered TM oxide NIB cathodes and to identify new material design principles to improve the reversibility of the oxygen-based redox processes (e.g. different TMs, different oxygen stacking); the results will be discussed in a future publication.

6.4. Conclusion

In summary, a new $Na_{0.78}Ni_{0.23}Mn_{0.69}O_2$ cathode shows outstanding electrochemical performance for rechargeable sodium-ion battery applications. The P2 structure of this material is stabilized over a wide voltage window, from 2.0 to 4.5 V. The stable framework facilitates Na intercalation/deintercalation during the electrochemical cycling process and ensures excellent rate performance. The electrochemical reaction is mainly based on the Ni^{2+} / Ni^{4+} redox couple, while Mn is electrochemically inactive and is stabilized as Mn^{4+} in the bulk of the material. An irreversible reaction taking place

upon initial charge and resulting in capacity degradation in the first cycle was carefully studied. It is found that the excess capacity during the first charge mainly comes from the high voltage region and is strongly affected by kinetic factors. EELS and sXAS results indicate a gradient distribution of TM oxidation states from the surface to the bulk of the electrochemically cycled particles. This gradient is closely related to the formation of oxygen vacancies at the surface of material. Therefore, it is proposed that oxygen anions get involved in the charge compensation process upon initial charge, leading to an additional plateau at high voltage. This is the first time that compelling evidence is provided for oxygen vacancies in Na-ion layered oxide materials. We believe that the Na to TM ratio has a strong influence on the behavior and structural stability of layered oxide materials. Further work is required to improve the reversibility of oxygen-based redox processes on extended cycling.

Chapter 6, in full, is a reprint of the material “Exploring Oxygen Activity in the High Energy P2-Type $Na_{0.78}Ni_{0.23}Mn_{0.69}O_2$ Cathode Material for Na-ion Batteries” as it appears in the Journal of the American Chemical Society, C. Ma, J. Alvarado, J. Xu, R. J. Clément, M. Kodur, W. Tong, C. P. Grey, Y. S. Meng, 2017, 139 (13), 4835. The dissertation author was the primary investigator and author of this paper. All the experiment parts were performed by the author except for the EIS, NMR and soft XAS parts.

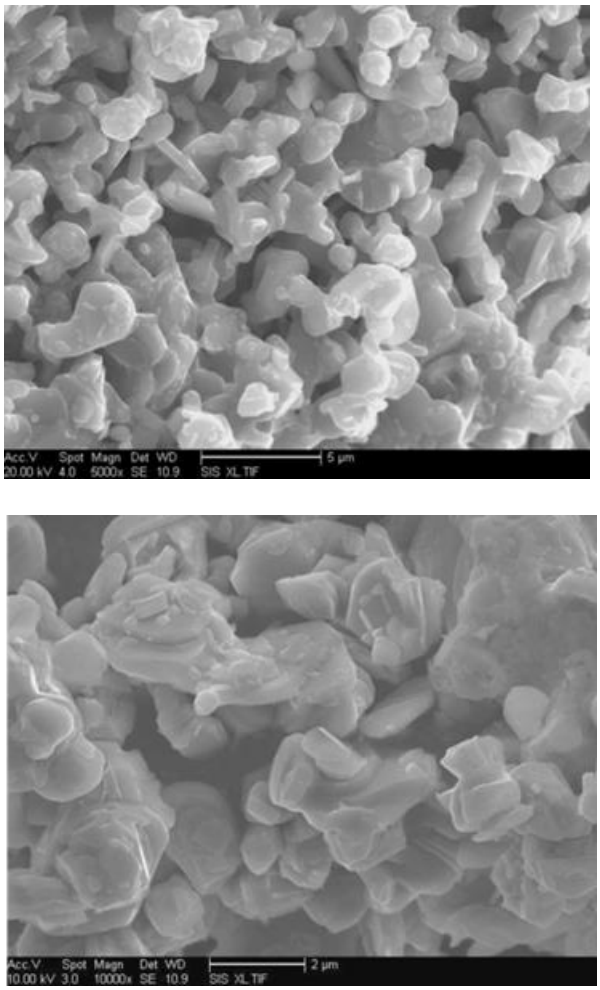

Figure 6.1. SEM images of as-synthesized $Na_{0.78}Ni_{0.23}Mn_{0.69}O_2$.

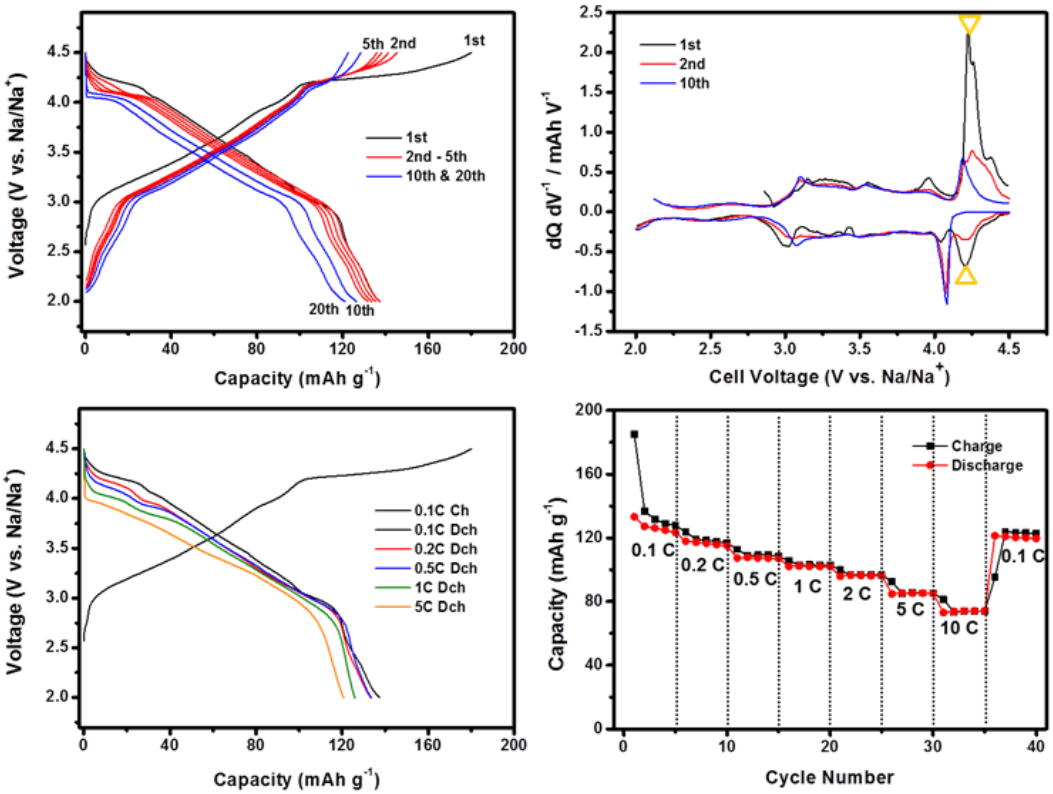

Figure 6.2. Electrochemical characterization of $Na_{0.78}Ni_{0.23}Mn_{0.69}O_2$: (a) Electrochemical profiles during the 1st, 2nd, 3rd, 4th, 5th, 10th, and 20th cycles at 0.1 C, (b) differential capacity ($dQ\ dV^{-1}$) vs. voltage plots at various cycles, (c) voltage profiles at different current densities, and (d) rate and cycling capabilities at different current densities from 0.1 C to 10 C (1 C = 121 mA g^{-1}).

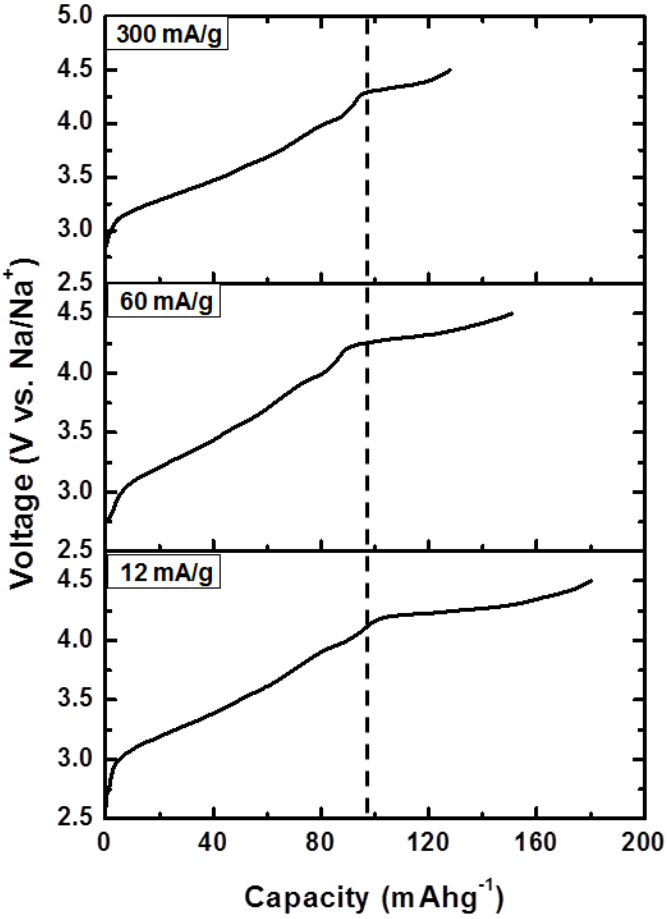

Figure 6.3. Voltage profiles on 1st charge using different current densities.

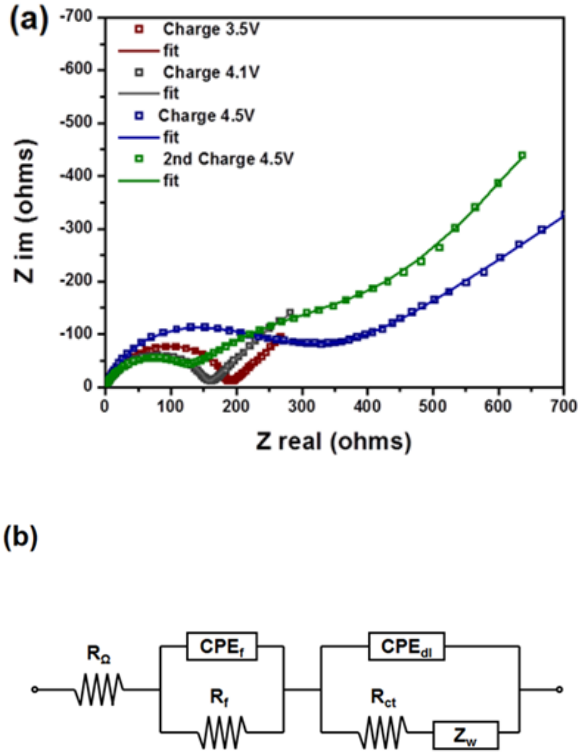

Figure 6.4. (a) Impedance spectra obtained at different states of charge (SOCs) during the first and second electrochemical cycles using a three electrode cell. (b) The equivalent circuit used to fit (straight line) the experimental impedance (squares) and extract the values for the various contributions at different SOCs.

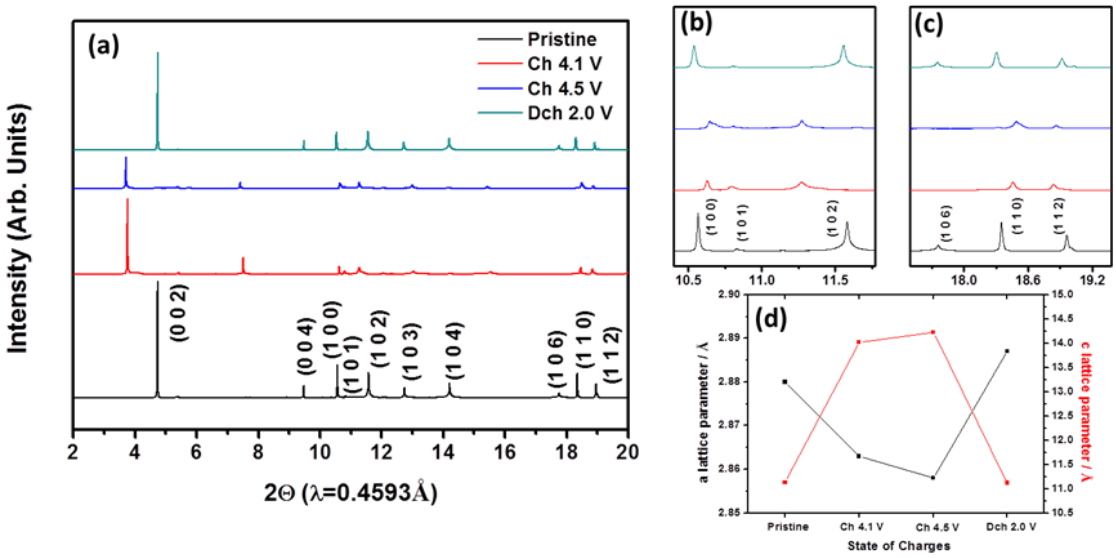

Figure 6.5. Synchrotron X-ray diffraction patterns of $Na_{0.78}Ni_{0.23}Mn_{0.69}O_2$ electrodes stopped at different states of charge (SOCs) during the first electrochemical cycle, (b) (c) enlarged regions of the XRD patterns containing the (1 0 0), (1 0 1), (1 0 2), (1 0 6), (1 1 0) and (1 1 2) peaks, and (d) evolution of the a and c lattice parameters during the first charging process, as determined from Rietveld refinements.

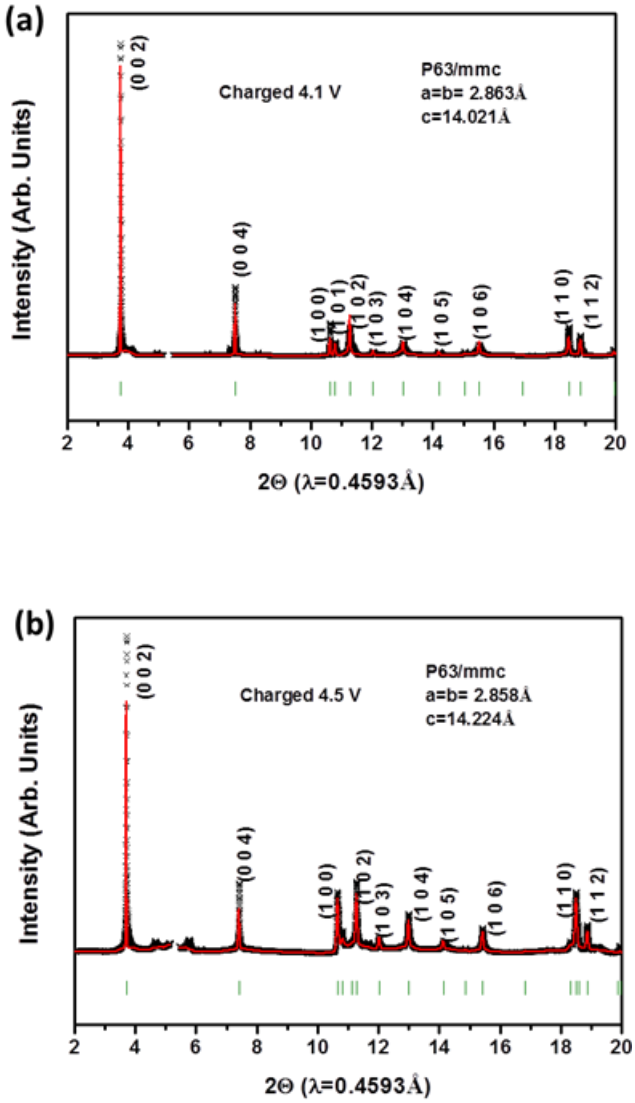

Figure 6.6. SXRD profiles of P2-$Na_{0.78}Ni_{0.23}Mn_{0.69}O_2$ samples (a) charged to 4.1 V and (b) charged to 4.5 V fitted in the $P6_3/mmc$ space group. (Black: raw data, Red: fitted profile).

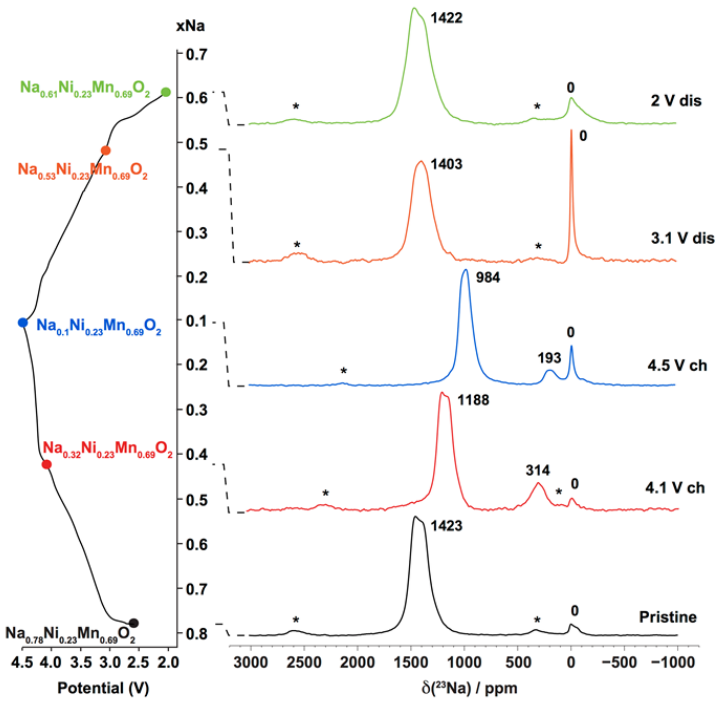

Figure 6.7. ^{23}Na NMR spectra acquired on as-synthesized P2−$Na_{0.78}Ni_{0.23}Mn_{0.69}O_2$ and on electrodes stopped at four different SOCs along the first electrochemical cycle. The spectra were collected at room temperature, 60 kHz MAS (Magic Angle Spinning), and at an external field of 4.7 T. Spinning sidebands are denoted with (∗). The diamagnetic signal at 0 ppm is presumably due to residual Na_2CO_3 starting material in the spectrum obtained on the as-prepared sample, and to electrolyte decomposition products formed upon cycling in the spectra collected upon charge and discharge.

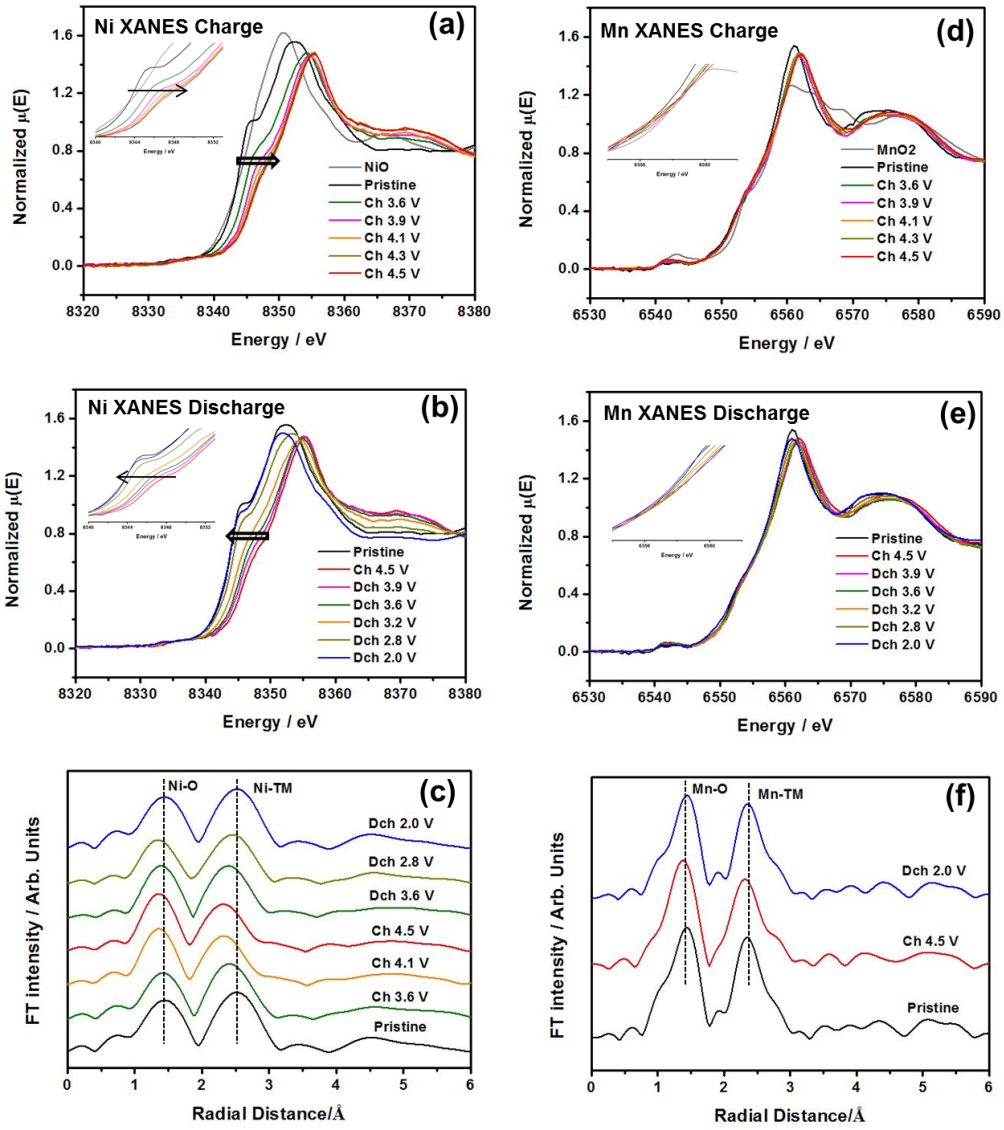

Figure 6.8. In-situ XAS analysis of $Na_{0.78}Ni_{0.23}Mn_{0.69}O_2$ electrodes at different SOCs during the first electrochemical cycle: (a) (b) XANES spectra at Ni K-edge, (d) (e) XANES spectra at Mn K-edge, and (c) (f) corresponding EXAFS spectra.

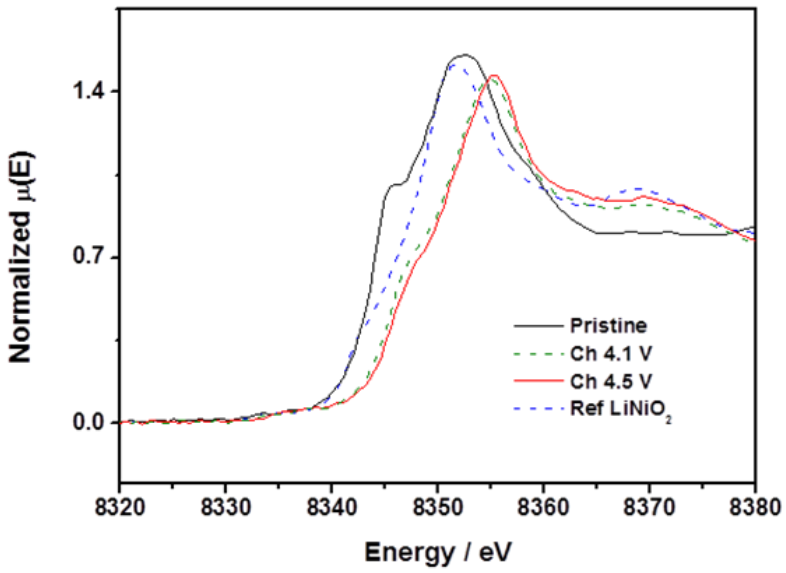

Figure 6.9. Comparison of Ni K-edge XANES spectra obtained on P2-$Na_xNi_{0.23}Mn_{0.69}O_2$ samples with that obtained on a pristine $LiNiO_2$ sample (Ni^{3+} standard).

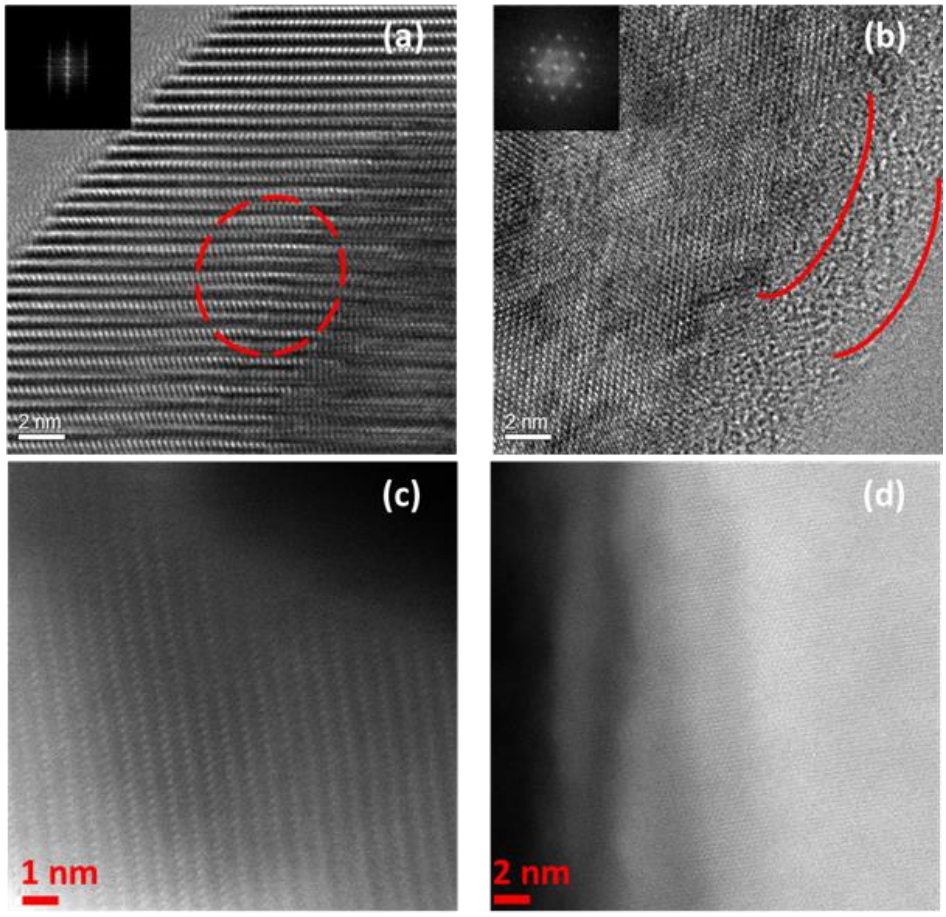

Figure 6.10. (a) High resolution TEM images and (c) corresponding HAADF image of pristine $Na_{0.78}Ni_{0.23}Mn_{0.69}O_2$ along [0 1 0]. (b) High resolution TEM images and (d) corresponding HAADF image of electrochemically-cycled $Na_xNi_{0.23}Mn_{0.69}O_2$ along [0 0 1].

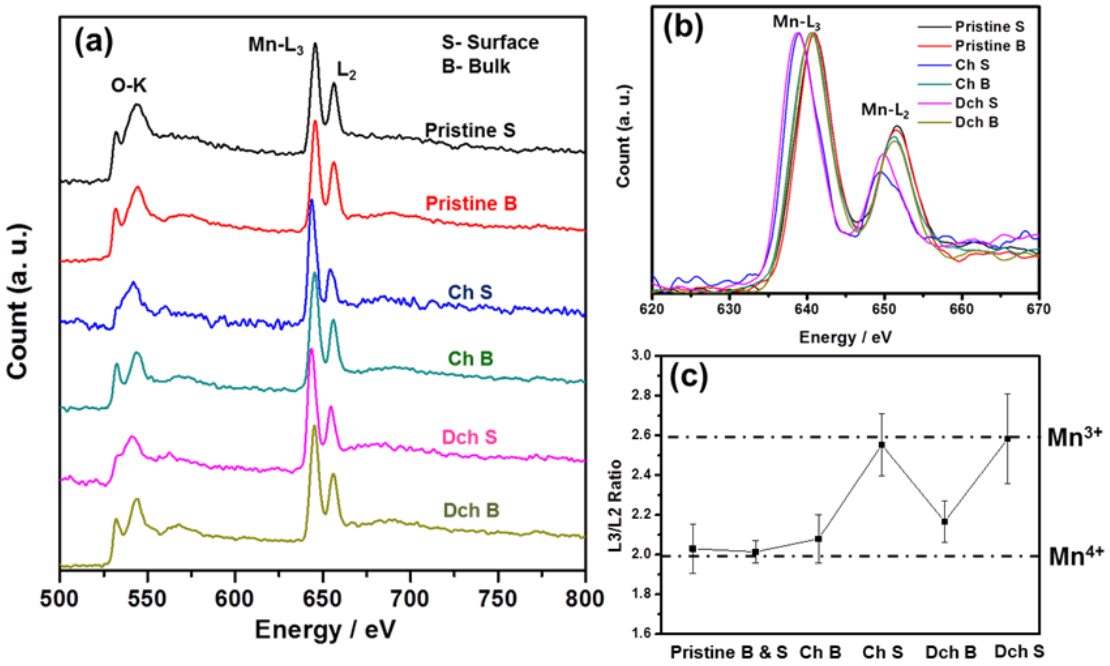

Figure 6.11. EELS spectra of the (a) O K-edge and (a&b) Mn L-edge measured at the surface (S) and in the bulk (B) of pristine and electrochemically cycled $Na_xNi_{0.23}Mn_{0.69}O_2$ particles. (c) The corresponding Mn L_3/L_2 ratio.

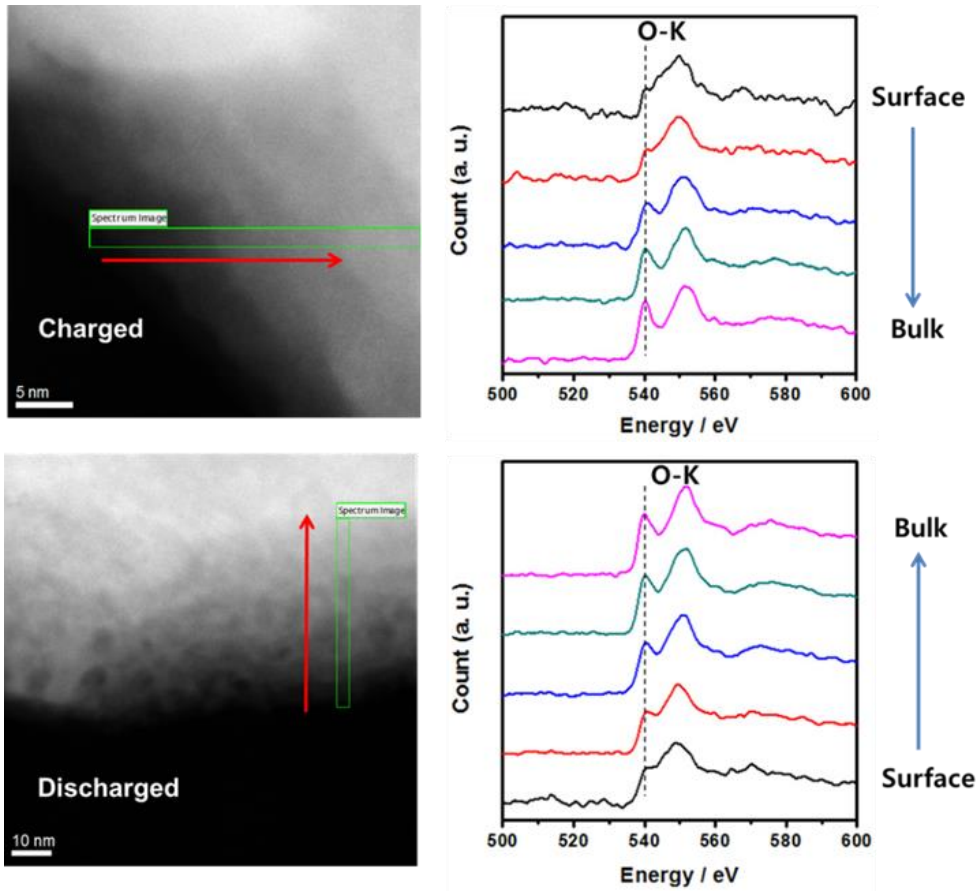

Figure 6.12. Stepwise EELS scan obtained from the surface to the bulk of electrochemically-cycled particles.

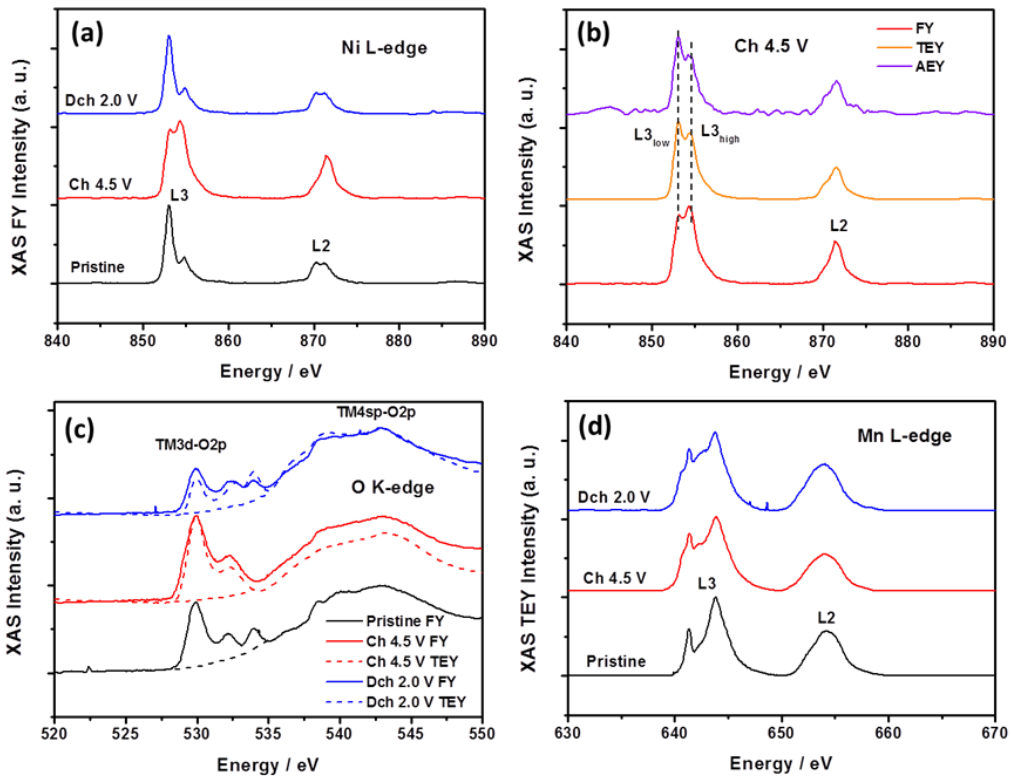

Figure 6.13. (a) Ni L-edge XAS spectra of electrochemically cycled $Na_{0.78}Ni_{0.23}Mn_{0.69}O_2$ electrodes in FY mode (b) Ni XAS L-edge spectra of the fully charged electrode using AEY (purple), TEY (yellow) and FY (red) modes, (c) O K-edge XAS spectra in FY and TEY modes, and (d) Mn L-edge XAS spectra of electrodes cycled to different SOCs using TEY mode.

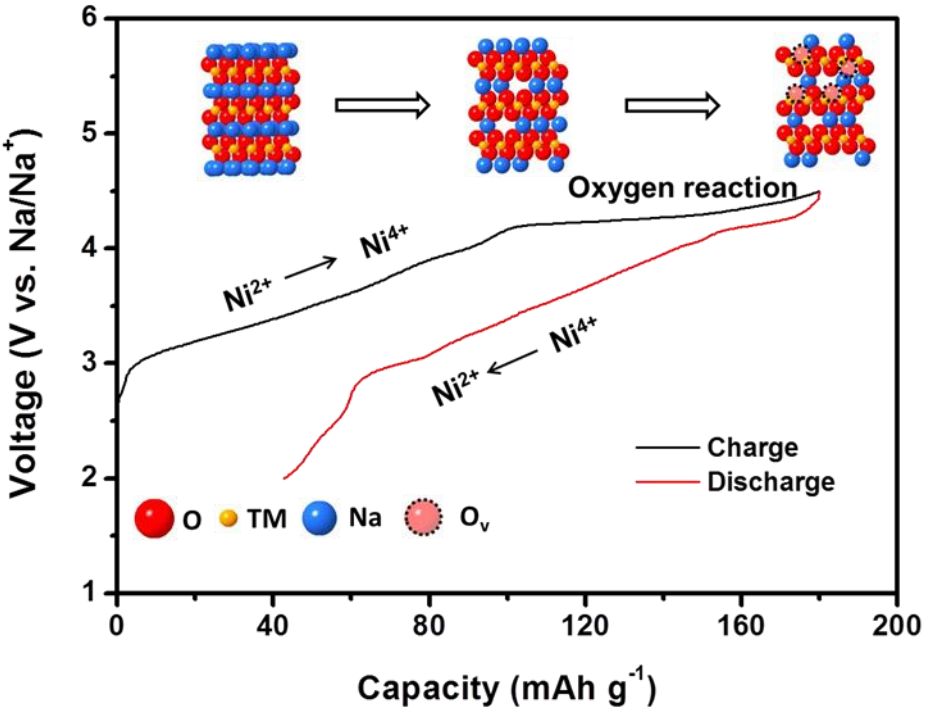

Figure 6.14. Charge compensation mechanisms in the P2-$Na_{0.78}Ni_{0.23}Mn_{0.69}O_2$ cathode.

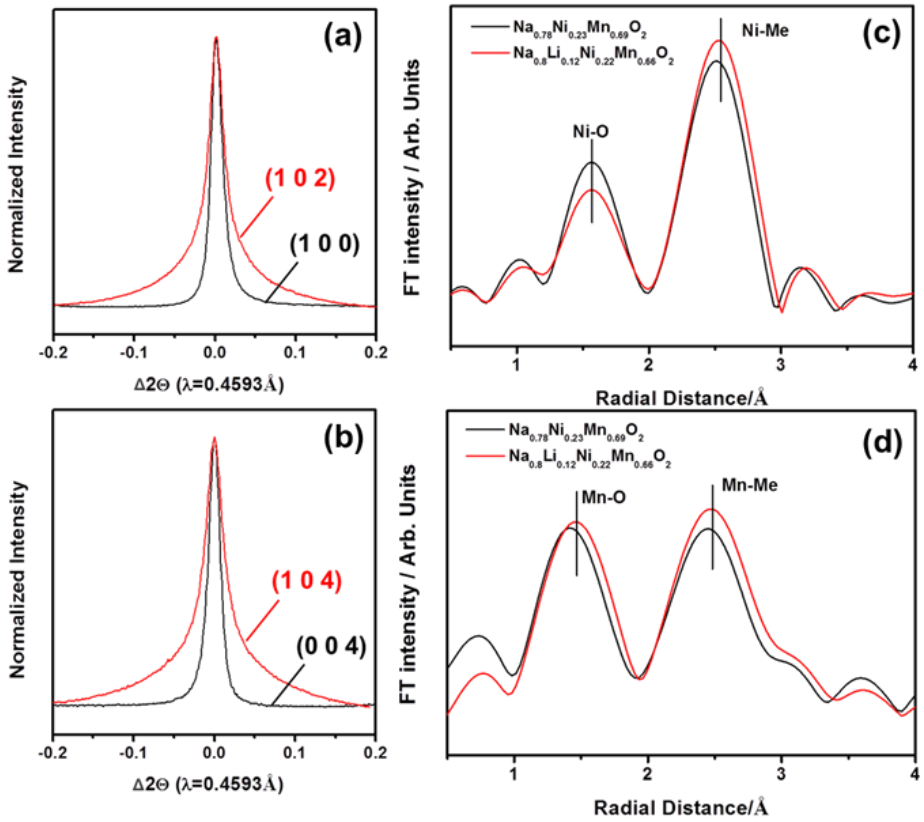

Figure 6.15. (a)(b) Enlarged comparison between the (*h* 0 0), (0 0 *l*) and (1 0 *l*) synchrotron XRD peaks of pristine $Na_{0.78}Ni_{0.23}Mn_{0.69}O_2$ sample. (c)(d) Ni, Mn K-edge EXAFS spectra of the pristine $Na_{0.78}Ni_{0.23}Mn_{0.69}O_2$ sample and pristine $Na_{0.8}Li_{0.12}Ni_{0.22}Mn_{0.66}O_2$ sample respectively.

Table 6.1. Fitting parameters for the equivalent circuit model shown in Figure 6.4 (b).

Voltage (V)	R_Ω	R_f	R_{ct}	Total (R_f + R_{ct})	Chi-Squared
3.5	1.20	9.532	175	184.5	6.02×10^{-4}
4.1	1.34	12.35	140.4	152.8	2.58×10^{-4}
4.5 (first cycle)	2.43	30.1	260	290.1	1.69×10^{-4}
4.5 (second cycle)	1.23	45.9	119.8	165.7	6.13×10^{-4}

Table 6.2. Analysis of the Ni and Mn K-edge EXAFS spectra for pristine $Na_{0.78}Ni_{0.23}Mn_{0.69}O_2$ sample.

X-Y Pair	R(Å)	S_0	N	$\sigma^2(10^{-3}Å^2)$	E_0	R-factor(%)
Ni-O	2.031(3)	1.00	6	5.6(9)	-5.9(5)	0.9
Mn-O	1.926(6)	1.00	6	5.7(7)	-7.1(1)	1.89
Ni-TM	2.866(1)	1.04	6	10.5(5)	-6.0(9)	0.9
Mn-TM	2.859(3)	0.94	6	11.0(6)	-10.0	1.89

Chapter 7. Improvement of the Cathode Electrolyte Interphase on P2-$Na_{2/3}Ni_{1/3}Mn_{2/3}O_2$ by Atomic Layer Deposition

Atomic layer deposition (ALD) is a commonly used coating technique for lithium ion battery electrodes. Recently, it has been applied to sodium ion battery anode materials. ALD is known to improve the cycling performance, coulombic efficiency of batteries, and maintain electrode integrity. Here, the electrochemical performance of uncoated P2-$Na_{2/3}Ni_{1/3}Mn_{2/3}O_2$ electrodes is compared to ALD coated Al_2O_3 P2-$Na_{2/3}Ni_{1/3}Mn_{2/3}O_2$ electrodes. Given that ALD coatings are in the early stage of development for NIB cathode materials, little is known on how ALD coatings, in particular aluminum oxide (Al_2O_3), affect the electrode-electrolyte interface. Therefore, full characterizations of its effects are presented in this work. For the first time, X-ray photoelectron spectroscopy (XPS) is used to elucidate the cathode electrolyte interphase (CEI) on ALD coated electrodes. It contains less carbonate species and more inorganic species, which allows for fast Na kinetics, resulting in significant increase in coulombic efficiency and decrease in cathode impedance. The effectiveness of Al_2O_3 ALD coating is also surprisingly reflected in the enhanced mechanical stability of the particle that prevents particle exfoliation.

7.1. Introduction

The commercialization of the rechargeable lithium ion battery (LIB) in the early 1990s[163] by Sony propelled the development of portable electronics. Technologies that once seemed impossible are now ingrained in modern society and have become a part of

everyday life. This is largely due to the components within the battery that allow lithium ions to intercalate/deintercalate between the carbon anode and transition metal oxide cathode through the electrolyte, making it a high gravimetric energy density system.[1,61,164] As consumers become more aware of the global climate change, the applications for LIBs are extended to power hybrid and plugin electric vehicles,[114] however, using LIBs as a ubiquitous energy storage and conversion system could increase the demand for lithium, causing exorbitant prices of Li resources.[165] Therefore, researchers have focused their efforts on finding alternative systems that could replace LIBs in specific applications. Sodium ion batteries (NIBs) research was first investigated in the mid 1970s, where the sodium analog to lithium transition metal oxides were first reported.[88,122] In the recent decade, NIB research has significantly increased given the above-mentioned concerns with LIBs. NIBs offer several advantages over its lithium counterpart, given that the demand for sodium is much lower than lithium and it is more abundant.[166] Overall, the cost of manufacturing NIBs can be lower than that for LIBs[165],which can be attributed to the ability to use aluminum as the current collector for both the anode and cathode—eliminating the use of Cu, a heavier and more expensive material.[167] Though NIBs will unlikely reach the energy density of LIBs because of sodium's increased atomic mass and reduced electrochemical potential of 2.71V (Li=3.01V), it could be an alternative for large grid storage applications where cost plays a more significant role.[115,120]

Within the last decade several advancements have been made on the anode for NIBs where hard carbon, sodium titanate, tin oxide, and tin sulfide (few of several anode chemistries) have been extensively studied.[9,168–170] Given that in a full cell the cathode

has higher mass fraction than the anode and operates at a higher potential–increasing the capacity in NIBs requires more exploration on high voltage cathode materials.[131] Layered transition metal cathode materials (Na_xTMO_2) are of particular interest because of their high operating voltage, specific capacity, and synthesis yield.[59,115,131] This class of cathode materials can be classified by their crystal structure stacking: P2, O2, P3, and O3.[171] The first letters "P" and "O" correspond to where the alkali metal lies within the crystal structure–either in the prismatic or octahedral site. The number is related to the number of repeating Na layers within the unit cell. Of these classes of materials, P2-$Na_{2/3}Ni_{1/3}Mn_{2/3}O_2$ has been extensively studied due to its high specific capacity (173 mAh/g) and high operating voltage (up to 4.5V). Lu et al. demonstrated that Na-ions can reversibly intercalate and deintercalate using in-situ X-ray diffraction (XRD), albeit, undergoing detrimental phase transformation concurrently.[172] Lee and Xu et al. determined via synchrotron XRD and first principles calculations that the long voltage plateau above 4.22V corresponds to a O2 phase transformation.[129] While the material has a Na content of 1/3 to 2/3, P2 phase is the lowest energy state but when the Na content falls to zero then O2 phase becomes the lowest, causing poor capacity retention[129,148] However, this can be combated by lowering the operating voltage from 4.5 to 4.1V, eliminating the phase transformation and increasing the rate capability (Capacity at 1C = 85% Capacity at C/20). This is not a perfect solution because it sacrifices a large amount of energy by lowering the specific capacity from 174 to 90 mAh/g. Researchers have used doping (Li, Mg, and Zn) to maintain the high operating voltage and capacity, while reducing and or eliminating the phase transformation.[35,173–175] However, the cathode operating potential may also cause the electrolyte to decompose forming the cathode

electrolyte interphase (CEI) which may also participate in the capacity degradation. Despite that doping improves the cycling stability of P2- $Na_{2/3}Ni_{1/3}Mn_{2/3}O_2$ class of materials, researchers have failed to address the carbonate based electrolyte instability above 4.2 V.[176]

Forming a protective layer that allows Na-ions to diffuse through the layer and reduce the electrolyte decomposition is one possible way to improve the electrolyte-electrode interface. Atomic layer deposition (ALD) is used in a variety of applications as a coating technique, in particular for battery electrodes. Several advantages in using ALD are: 1) conformal coating, it has the ability to coat various irregular materials, 2) controllable coating thickness down to angstroms or monolayers, and 3) apply to a wide range of coating materials (Al_2O_3, TiO_2, ZnO, HfO_2).[177] For this reason, ALD has largely been adopted for coating LIB electrodes and shown to improve cycling performance.[178–184] Considering the success on LIBs, researchers have adopted ALD coating for NIB anode materials. Zhao and coworkers have shown improved cycling performance of disodium terephthalate by Al_2O_3 ALD coating.[185] Recently, Han et al used ALD to coat Al_2O_3 on tin nanoparticles to elevate volume expansion in the anode.[186] Few reports have reported the use of ALD coatings as cathode materials for NIBs.[187] Liu et al demonstrated the effect of wet chemical Al_2O_3 coating on P2-$Na_{2/3}Ni_{1/3}Mn_{2/3}O_2$ cathode for NIBs.[188] The issues with wet chemistry coating are that it is not able to control the coating thickness, it is difficult to have a conformal coating, and it can introduce contamination during the process. Although there is an improvement in capacity retention with this method, it is challenging to determine what percentage it played in improving the cycling performance when the electrode was only cycled to 4.3V, which partially avoids the

phase transformation (full phase transformation occurs at 4.5V). Moreover, both coating works mainly focused on the electrochemistry to showcase the effect of ALD and wet chemical coating of Al_2O_3 on P2-cathode materials. Understanding the ALD coatings for P2-cathode materials for NIBs is still in its infancy; there is a need to understand how ALD coatings improve the cycling performance by investigating the electrode-electrolyte interface. Since NIB chemistry behaves differently than LIB chemistry, it is likely that the cathode electrolyte interphase can be composed of different components.

Herein, we compare uncoated P2-$Na_{2/3}Ni_{1/3}Mn_{2/3}O_2$ (NaNiMnO) composite electrode to an ultra-thin Al_2O_3 ALD coated electrode. Rigorous electrochemical characterization demonstrates the positive effect of ALD coating on the composite electrode. For the first time, X-ray photoelectron spectroscopy is used to elucidate to the factors that influence the chemical composition of the cathode electrolyte interphase (CEI) which enhances the coulombic efficiency and cycling performance (from 2-4.5V), by decreasing the impedance of the cycled P2-NaNiMnO cathode with ALD coating.

7.2. Experimental

The $Na_{2/3}Ni_{1/3}Mn_{2/3}O_2$ material was synthesized by co-precipitation method following our previous published work.[129] A stoichiometric amount of the precursors, $Mn(NO_3)_2$ $4H_2O$ and $Ni(NO_3)_2$ $6H_2O$, were dissolved in deionized water. The transition metal nitrate solutions were titrated into a stoichiometric NaOH solution using a peristaltic pump at rate of 10 ml/hr. The solution was stirred slowly to insure homogeneity. The co-precipitated solid $M(OH)_2$ was centrifuged and washed with deionized water (three times). The co-precipitated material was dried in the oven to

remove excess water and was ground with a stoichiometric amount of Na_2CO_3. The material was precalinated at 500 ℃ for 5 h and calcinated in a pellet form at 900 ℃ for 14 h in a 50 ml porcelain crucible. Electrodes were made by a slurry containing 80 wt% of active material (based on the total mass of the P2-$Na_{2/3}Ni_{1/3}Mn_{2/3}O_2$ composite), 10 wt% of polyvinylidene fluoride (PVDF), and 10 wt% acetylene carbon black in n-methyl-2-pyrrolidone. The slurry was casted on aluminum foil and dried in a vacuum oven at 80 ℃.

The electrode casted on aluminum foil was coated with aluminum oxide (Al_2O_3) using atomic layer deposition (Beneq TFS200). The deposition of Al_2O_3 required the use of trimethylaluminum (TMA) as precursor and water as reactor. The carrier gas was nitrogen in 300 mbar and the reaction temperature was 150 ℃. The deposition rate was 1.1A per cycle. The coating thickness on the electrodes was controlled through the number of cycles performed.

The uncoated and ALD coated P2-$Na_{2/3}Ni_{1/3}Mn_{2/3}O_2$ electrodes were assembled in 2032 coin cells using a glass fiber GF/F (Whatman) filter separator soaked in 1 M $NaPF_6$ in propylene carbonate electrolyte (PC). Battery assembly was carried out in an MBraun glovebox (H_2O < 0.1ppm). Galvanostatic discharge and charge at various current densities were performed using an Arbin BT2000 battery cycler. Additionally, electrochemical impedance spectroscopy (EIS) measurements were carried out with 10 mV perturbation and the AC frequencies from 0.01 to$1x10^6$ Hz on galvanostatic cycled electrodes at OCV, first cycle and 100 cycles. The electrodes were assembled in a three electrode Swagelok ® cell, where the active material was the working electrode and Na metal served as the counter and working electrode. The three electrode cells were then cycled using above mentioned conditions. This allows for proper isolation of working

electrode impedance. A Solatron 1287 Potentiostat was used to measure the impedance at different states of charge and discharge. After the EIS measurements were taken, an equivalent circuit model was fit to the data to analyze the reactions that took place using Z view software (v. 3.4a, Scribner Associates, Inc.).

The morphology of the as-synthesized material and post-electrochemical cycling was characterized by a Philips XL30 environmental scanning electron microscope (ESEM) equipped with an energy dispersive x-ray detector (EDX) operating at 10 kV. Transmission electron microscopy (TEM) images were taken with a FEI 200 kV Sphera Microscope. Samples for TEM were prepared by focused ion beam (FEI Scios DualBeam FIB/SEM), following the procedure from our previous work.[189] Samples were thinned within 100 nm. During FIB thinning process, only 5 kV voltage and 7 pA current were applied to the sample when the sample thickness is within 200 nm. This measure can minimize the beam-induced damaging within only within 10 nm.[190] A lift-out procedure with optimized FIB fabrication conditions was conducted on the coated ALD electrode and loaded on the Omni Probe grid (Ted Pella) which is needed to retain the electrochemical activity of the nanobattery. Image J was used to determine the ALD coating thickness on the entire electrode.

After electrochemical cycling, the cells were disassembled in the glovebox and washed with DEC to remove excess sodium salt. XPS was performed at the Laboratory for Electron and X-ray Instrumentation using a Kratos AXIS Supra. In order to avoid air exposure, the samples were prepared in the glovebox connected to the XPS. Samples were transferred from the glove box to the XPS from an argon atmosphere to an ultra-high vacuum greater than 10^8 torr. The XPS was operated using Al anode source at 15 kV.

All XPS measurements were collected with a 300 μm by 700 μm spot size without using a charge neutralizer during acquisition. Survey scans were collected with a 1.0 eV step size followed by high-resolution scans with a step size of 0.05 eV, for carbon 1s, oxygen 1s, sodium1s, fluorine 1s, nickel 2p, manganese 2p, aluminum 2p, and phosphorus 2p regions.

Fits of the XPS spectra were performed with CasaXPS software (version 2.3.15, Casa Software Ltd.) to estimate the atomic compositions and chemical species comprising the cathode electrode interphase. All species were fit using a Shirley background. The resulting spectra were then refit and all spectra were shifted relative to the binding energy of the carbon 1s sp^3 (assigned to 284.8 eV) to compensate for any off-set during the measurement.

7.3. Results and Discussion

7.3.1. Aluminum Oxide ALD Coating Characterization

Inspired by ALD cathode coatings on LIB cathode materials, we coated classical P2-$Na_{2/3}Ni_{1/3}Mn_{2/3}O_2$ (P2-NaNiMnO) cathode with aluminum oxide (Al_2O_3) by ALD. The phase pure crystalline P2-NaNiMnO material is validated by the rietveld refinement (Figure 7.1). It is widely accepted that both binder and conductive additive contribute to the surface reactions caused by the instability of the electrolyte at high voltages.[191] To combat these issues, ALD was used to coat Al_2O_3 on the P2-NaNiMnO composite electrode surface. The deposition temperature occurred at 150 ℃ to prevent the chemical decomposition of the PVDF binder, ensuring that a stable electrode is used. Figure 7.2 shows the SEM images of the as synthesized electrode material and the ALD coated

electrode. EDS mapping was used to show that Al_2O_3 coating is uniform throughout the electrode and did not affect the electrode morphology. Since the entire electrode was coated, it is important to distinguish the amorphous ALD coating from the amorphous conductive carbon. First, a section of the electrode was cut using focused-ion beam (FIB) to allow proper characterization of the top of the electrode. If FIB is not used and the coating thickness is characterized by scrapping the electrode and loading the material on the TEM grid for imaging, one is unable to distinguish the amorphous material, leading to improper ALD thickness characterization (Figure 7.3). Figure 7.4 shows a uniform ALD coating of 1nm on the P2-NaNiMnO particle. The higher resolution TEM image (Figure 7.4 (b)) gives a detailed view of the amorphous layer to the crystalline active material, a uniform ALD coating of 1nm on the P2-NaNiMnO particle.

7.3.2. Galvanostatic Cycling Comparison of Uncoated and Al_2O_3 ALD Coated P2-$Na_{2/3}Ni_{1/3}Mn_{2/3}O_2$

The uncoated and ALD coated P2-NaNiMnO electrodes were assembled into coin cells, then cycled in galvanostatic mode at C/20 rate. Figure 7.5 (a) highlights the materials first cycle voltage profiles, demonstrating the quintessential plateaus for this material.[129,192] The Al_2O_3 coated ALD electrode (blue), however, shows slight increase in the discharge capacity of 142.6 mAh/g compared to the uncoated electrode (134.6 mAh/g). More importantly, the P2-O2 phase transformation is evident in both electrodes in the charge state, demonstrating that ALD coating does not eliminate such a structure transformation. The differential capacity versus voltage profiles (Figure 7.5 (b)) shows five distinct dQ/dV peaks that correspond to the intercalation of Na-ions. The sharp peak

at 4.20V is due to the P2-O2 phase transformation associated with this class of materials.[129] This peak is less intense in the Al_2O_3 coated electrode, owing to the strong binding of the coating to the surface of the material thus slightly reducing the phase transformation and possibly forming the CEI. The coating does not eliminate the phase transformation but may aid in maintaining the particle integrity. Furthermore, a small peak at 2.98V (Figure 7.5 (b) insert) appears in the dQ / dV plots of the Al_2O_3 coated electrode, which is not shown for the uncoated sample in this work nor in the literature, it might be possible that this could be from the Al2O3 reacting during electrochemical cycling.

After repeated cycling, the material structure degrades as a result of the severe phase transformation (Figure 7.5 (c)). The ALD coated electrode still retains more of the structure properties at the 50^{th} cycle as demonstrated by the voltage plateaus. As shown, the coated electrode has a higher capacity of 92.3 mAh/g compared to the uncoated electrode capacity of 69.7 mAh/g. Given that the material has gone under repeated phase transformation, the dQ/dV of the 50^{th} cycle depicts that the peaks are no longer as sharp as they were in the first cycle. In Figure 7.5 (d), the peak at 2.98V persists after 50 cycles. Finally, it is obvious that Al_2O_3 ALD coating reduces the overall potential in the cell throughout electrochemical cycling. This is a common occurrence in Li-ion cathode electrodes when coated with an ALD type coating.[193,194] Though bulk Al_2O_3 is insulating in nature, the ultra-thin coating and amorphous nature reduce insulating effects at lower current density, allowing the transport of Na-ions through the film, yet its effects are still observed.

The electrochemical characterization of the uncoated and ALD coated P2-NaNiMnO electrodes are provided in Figure 7.6. The theoretical capacity of uncoated P2-NaNiMnO cathode material is 173 mAh/g due to the Ni redox reaction from Ni^{2+} to Ni^{4+} corresponding to the mole ratio of the Na-ions. Given that the coating is 1nm, which attributes to less than one percent of the total material weight, therefore, the coating weight is negligible. Both electrodes were cycled at constant current from 4.5 V to 2.3 V for 100 cycles. Figure 7.6 (a) demonstrates the capacity versus cycle plot for the ALD coated and uncoated electrodes. The ALD coated electrode improves the capacity retention of P2-NaNiMnO—after 100 cycles, the cell exhibits a capacity of 77.43 mAh/g while the uncoated electrode has a capacity of 52 mAh/g. As expected the thin Al_2O_3 coating did not bring about drastic improvement in capacity retention because of the severe phase transformation that occurs above 4.2V. However, the coating does improve the capacity retention and may aid in other aspects of the electrochemical performance. By observing the value of the x-axis of each half cycle (Figure 7.5 (a), (c)), one can estimate the storage capacity of each electrode. Ultimately, the ratio of the two capacities is known as the coulombic efficiency (CE). This is one way to quantify the irreversibility of each cycle, shown in Figure 7.6 (b). We note that the thin coating improves the CE of the active material throughout electrochemical cycling. The first cycle CE for the ALD coated electrode is 91.6% and quickly reaches 99% in the fifth cycle. Conversely, the uncoated electrode exhibits a first cycle efficiency of 83.8% and 95.2% CE by the fifth cycle. Throughout electrochemical cycling, the uncoated electrode has an unstable CE as shown in Figure 7.6 (b). The CE fluctuates significantly while the ALD coated P2-NaNiMnO electrode maintains a stable CE, demonstrated by the flat curve. Comparing

our previous work with the ALD coated LIB cathodes, we present similar effects.[195–197] Wise et al. demonstrated that an ultra-thin coating of Al_2O_3 can significantly improve the electrode-electrolyte interface, reducing the decomposition of the electrolyte on high voltage cathode materials.[198] The addition of the artificial Al_2O_3 CEI coating on P2-NaNiMnO active material enhances the interface by reducing the exposure of the electrolyte to the active material. The 1 nm Al_2O_3 ALD coating may help reduce the decomposition of the electrolyte by protecting the active material, PVDF binder, and conductive carbon from reacting with the electrolyte; therefore, improving the CE throughout electrochemical cycling.

The electrochemical rate performance test is a good way to measure the kinetic property of the material at various charge and discharge rates. Here, the material is put under various stresses implemented through incremental current increase every few cycles. Figure 7.6 (c) compares the rate capability of the uncoated P2-NaNiMnO and Al_2O_3 ALD coated electrode. The rate performance begins at C/20, increases to 1C then returns back to C/20 after a 25 cycles period. The uncoated P2-NaNiMnO electrode exhibits inferior rate capabilities when increasing the rate from C/20 to C/10 then to C/5, and finally to C/2 compared to the ALD coated electrode. The disparity capacity increases at C/2, where the coated electrode has an average specific capacity of 105.6 mAh/g compared to 78.5 mAh/g for the uncoated electrode. Thus far, the coated electrode has outperformed the uncoated P2-NaNiMnO. However, at 1C the ALD electrode retains less capacity. Comparing our work to ALD coatings on the cathode materials for LIBs, the effect of thin Al_2O_3 ALD coatings on high voltage LIB cathode materials differ significantly. In some cases, the Al_2O_3 substantially improves the rate

capability by preventing transition metal dissolution and reducing electrolyte decomposition.[194,196,197,199] Conversely, there are accounts that demonstrate the Al_2O_3 coating has lower capacity than the bare electrode at higher rates.[200] These effects are not ubiquitous with one type of active material; the high voltage lithium nickel manganese oxide, for example, has poor rate capability when coated with Al_2O_3.[195] Riley et al. clearly show that at higher rates from C/4 to 1C the ALD coated electrode has a lower capacity than the bare $Li(Ni_{1/3}Mn_{1/3}Co_{1/3})O_2$, which is attributed to the Al_2O_3 creating a barrier for ion mobility.[201] Although it is difficult to compare Al_2O_3 ALD coating on various cathode materials in LIB due to electrode configuration, the above-mentioned cases can be applied to NIB coated cathode materials.

There are few works that have used Al_2O_3 as a protective layer for SIB cathode materials.[187,188] Kaliyappan and coworkers investigated a series of ALD Al_2O_3 coated electrodes with discrete thicknesses on P2-$Na_{2/3}(Mn_{0.54}Ni_{0.13}Co_{0.13})O_2$ and the effects on rate performance. They determined that a thinner coating outperforms the bare cathode while a thicker coating hinders the rate capabilities due to the insulating properties of Al_2O_3.[187] Our work directly opposes the notion that a thinner coating is better, given that our ultra-thin coating has a lower capacity at higher rates. Both electrode materials have similar voltage ranges (2-4.5V) and were cycled at similar rates. However, it is commonly agreed upon that P2 cathodes suffer from severe phase transformations and that doping cobalt into the P2-NaNiMnO cathode enhances the cycling performance. Therefore, the improvement in rate capability for thin ALD coating in P2-$Na_{2/3}(Mn_{0.54}Ni_{0.13}Co_{0.13})O_2$ is not only due to the coating effect, but also the improved stability as a result of cobalt doping. Our material demonstrated the true effect of Al_2O_3 ALD coating

in a traditional P2-NaNiMnO without doping. Computation techniques are widely used to help validate experimental work or understand fundamental mechanisms that occur within a battery system during electrochemical cycling. Jung et al. used ab initio molecular dynamics calculations to investigate the sodiation through Al_2O_3 and compare it to Li-ions.[202] They conclude that Na-ion diffusion occurs much faster through Al_2O_3 compared to Li-ions even though the Na-ions are much larger, albeit the study was conducted through a crystalline Al_2O_3. However, the Al_2O_3 in our case is amorphous where we see that at fast rate (1C) the Al_2O_3 coated electrode has lower rate capability than the uncoated electrode, demonstrating that the diffusivity is subpar in the Al_2O_3 film.

7.3.3. Cathode Interfacial Resistance

Figure 7.7 shows the changes in the impedance spectra of the Al_2O_3 coated and uncoated P2-NaNiMnO electrodes cycled galvanostatically in a three electrode Swagelok® cell. Using a three electrode configuration allows us to hone in on the working electrode (P2-NaNiMnO cathode) impedance while eliminating the effects associated from the reference and working electrode (Na metal), demonstrated in Figure 7.8.[144] Previous reports failed to investigate the effect of the ALD coating on the cathode. They took into account the impedance of the sodium metal in addition to the coating which could lead to inaccurate impedance quantification.[187,188] Furthermore, there is a need to understand the effect of the Al_2O_3 coating. Figures 7.7 (a) and 7.7 (b) demonstrate the Nyquist plots for electrodes in the charged state after one cycle and 100 cycles. The Nyquist plots depicts the measured real versus imaginary impedance over a series of AC frequencies. We can quantitatively analyze the impedance spectra by a

model circuit generated by several reactions that occur in the cell during electrochemical cycling (Figure 7.7 (c)). The model accounts for the ohmic resistance of the electrolyte (R_Ω), the double layer capacitance of the electrode/electrolyte interface (CPE_{sf}), resistance due to the lithium ion diffusion through the surface reactions on the cathode (R_f), the double-layer capacitance (CPE_{dl}), and the charge transfer resistance (R_{ct}).[194,195,203,204] Finally, the model accounts for the Warburg impedance (Zw) known as the impedance according to solid state diffusion of the Na-ion through the bulk of the active material.[196]

Comparing the uncoated and Al_2O_3 coated electrodes after the first cycle (cycled at C/20), both the R_{sf} and R_{ct} are significantly lower in the coated electrode (Table 7.1). After one cycle the uncoated P2-NaNiMnO has a surface film resistance of 878.8 Ω while the Al_2O_3 coated P2-NaNiMnO has an R_{sf} value of 182 Ω. The R_{ct} associated with the Na-ion diffusion through the electrode-CEI interface is 3948 Ω for the uncoated electrode compared to 420 Ω for the coated electrode. After 100 cycles (cycled at C/20), the R_{sf} and R_{ct} increased significantly for the uncoated electrode compared to the coated electrode. The ultra-thin coating protects the surface of the electrode, reducing the effects that the binder and conductive additive have on electrolyte decomposition. Though Al_2O_3 is insulating in nature, the thin coating allows for Na-ions to diffuse through the coating film. Given that the surface film resistance increases slightly from the first cycle to the 100^{th} cycle, the Al_2O_3 coating reduces the electrolyte decomposition at high potentials, forming a better CEI.[184,201] From Table 7.1, the charge transfer resistance increases significantly compared to the coated P2-NaNiMnO. This implies that the active material structure has degraded significantly during electrochemical cycling, as shown in Figures

7.5 and 7.6. Therefore, the ALD coating helps suppressing the structure instabilities associated with sodiation and desodiation.[179] To validate the effect of Al_2O_3 ALD coating, post cycling characterization is required.

7.3.4. *Ex situ* Electrode Characterization

The above-mentioned electrochemistry has clearly demonstrated that the Al_2O_3 ALD coated electrode improves the cycling performance, CE, the surface film resistance, and charge transfer resistance. Part of the improvements can be attributed to particle stability; to examine this, SEM images were taken after 100 cycles at C/20 rate. The pristine electrode clearly shows the P2-NaNiMnO active material surrounded by acetylene black (Figure 7.9 (a)). After repeated slow cycling, the active material endures repeated sodiation and desodiation. As the Na-ions are extracted from the P2-NaNiMnO structure, the material compensates by the restructuring of the metal-oxide layer, causing the oxygen layer to glide to reduce the steric hindrance within the crystal structure.[59,129,173] Lu et al. proposed stacking faults occur as a result of the shift in oxygen-oxygen contact due to the instability of the metal oxide layer during sodium extraction.[205] Therefore, it is not surprising that the cycled uncoated P2-NaNiMnO demonstrated severe particle exfoliation. This is consistent with work done by Liu et al., where they investigated the failure mechanism of P2-NaNiMnO after 300 cycles at 1C using SEM and TEM.[188] Although this material undergoes an intercalation reaction mechanism, it can still exhibit stress and strain within the particle during electrochemical cycling. This is evident in our previous XRD study of the material, when the sodium concentration is less than 1/3, the oxygen layers are in direct contact leading to an

electrostatic repulsion which directly expands the c parameter.[129] Conversely, the ALD coated electrode significantly reduces particle exfoliation after 100 cycles and only few particles showed signs of particle degradation. The notion that ALD coating can be used to maintain particle integrity has been demonstrated in alloying anodes (Si and Sn) for LIBs by holding the particle together after 300% volume expansion during repeated lithiation.[181,206,207] In their case, a thick ALD coating can improve the integrity of the active material without forming a strong binding interaction between the coating and the active material. Since we applied an ultra-thin coating, it is speculated that the Al_2O_3 ALD coating forms Na-Al-O bonds to form a strong binding interaction that can reduce particle exfoliation. The detailed mechanism still requires more in-depth analysis. Having the ability to maintain electrode stability can be traced to the charge transfer resistance (Figure 7.7), which is the resistance associated with Na-ion diffusion through the surface of the active material through the SEI. To further understand how Na-ion kinetics is affected by ALD coating, it is needed to further investigate the effects of electrolyte decomposition on the P2-NaNiMnO particle surface both coated and uncoated.

The surface of each electrode was analyzed before cycling (uncycled, not exposed to electrolyte) in addition to after the first charge to 4.1V, 4.5V, 5 cycles, and 100 cycles— avoiding air exposure as described in the experimental section. The elemental atomic percentage of the cycled electrodes is shown in Figure 7.10, where we can see the elemental evolution of the SEI throughout electrochemical cycling. Figure 7.11 demonstrates that the cycled electrodes are largely dominated by acetylene black at 284.4 eV. Before cycling, the electrodes have the signature peaks of the PVDF polymer binder at 285.5 eV (CH_2), 290.5 eV, and 292.7 eV (CF_2). Once the electrodes are cycled to 4.1V,

the decomposition products of the PC electrolyte begin to evolve, forming CO, OCO, CO_3 moieties for both uncoated and Al_2O_3 coated. After the electrodes are cycled to 4.5V, the PVDF peak corresponding to C-F_2 broadens due to the formation of sodium carbonate species. Prolonged cycling causes all peaks to shift to higher binding energy and form more CO components in the in the coated electrode, which is largely associated with ethers, esters, and oligomeric species of polyethylene oxide $(CH_2\text{-}CH_2\text{-}O)_n$ [208] from the PC electrolyte decomposition. These functionalities can also be seen in the O1s spectra (Figure 7.12). For the uncoated P2-NaNiMNO electrode, peaks indicative of lattice oxygen (529.3 eV), surface oxygen (531.2 eV), CO from the interaction between the conductive additive and active material (532 eV), and Na auger (536 eV)[209] are clearly demonstrated. In the coated electrode, the Al-O (531.9 eV) peak corresponding to Al_2O_3 ALD coating as well as all of the above-mentioned peaks are shifted slightly to higher binding energy, due to the interaction with the coating (lattice oxygen at 529.6 eV, surface oxygen at 531.6 eV, CO at 532.6, and Na auger at 536.9 eV). As the electrolyte begins to decompose at 4.1V and 4.5V we begin to see organic decomposition products in Figure 7.12 and Figure 7.13 as well as oxidative species that result from the $NaPF_6$ salt ($Na_xPF_yO_z$ around 534 eV) for both coated and uncoated electrodes. However, for the Al_2O_3 coated electrode, the $Na_xPF_yO_z$ peak broadens and increases throughout electrochemical cycling. Moreover, the Al-O peak associated with the coating is present even after 100 cycles as shown in Figure 7.14. Both the O1s spectra and Al 2p spectra show a shift to higher binding energy as the cycle number increases. This could be due to the strong biding interaction that the ALD coating has with the electrode influencing the formation of a different CEI with respect to the uncoated electrode, consistent with the

shift in binding energies of the CEI functionalities and an increase in salt decomposition products. Furthermore, this demonstrates the robustness of the coating, also demonstrated in Figure 7.9, where the ALD coated electrode preserves the active material integrity even after repeated cycling. Consistent with the literature, we see that as we continue to cycle the electrodes, the surface oxygen peak decreases indicative of a thicker CEI formation.[208] Although it seems that the coated electrode has more CEI formation, the atomic percentage of carbon and oxygen in the surface is less than that of the uncoated P2-NaNiMnO (Figure 7.10). The dashed line in Figure 7.12, guides the peak shift that occurs throughout electrochemical cycling, which is more prevalent in the coated electrode. When peaks shift to higher binding energies it signifies that the binding environment is more electronegative which can be further investigated by F 1s (Figure 7.13 (a)), P 2p (Figure 7.13 (b)), and Na 1s (Figure 7.15).

Given that the electrode is composed of 80% active material, 10% PVDF binder, and 10% acetylene black, the uncycled electrodes have a large peak corresponding to the C-F bond of the binder (F 1s at 687 eV). This peak persists throughout cycling and continues to dominate the signal. Consistent with both the F 1s and Na 1s, a NaF peak at 684 eV for the uncoated P2-NaNiMnO and 685 eV for the Al_2O_3 coated electrode are observed. This is due to the interaction between the active material and the PVDF binder. The Na surface reacts with the PVDF to form NaF from the dehydroflurination, generating HF and reacting with Na, similar to the LIBs.[210–212] This is more prevalent in the Al_2O_3 coated electrode because it is needed to use the water as a precursor to form the aluminum oxide coating, which causes the PVDF binder to react with water forming more HF. Eventually, the formation of more NaF in the uncycled coated electrode maybe

one of the causes for prepping the electrode surface to promote the formation of a more inorganic CEI leading to higher initial CE and overall cycling performance compared to the uncoated electrode (Figure 7.6).

As we charge the electrodes to 4.1V, we begin to see the decomposition products form that result from the $NaPF_6$ salt. Similar to $LiPF_6$, the sodium salt is susceptible to a similar process (scheme 1-3)

$$NaPF_6 \leftrightarrow Na^+ + PF_6^- \quad (1)$$

$$PF_6^- + Na^+ \rightarrow NaF + PF_5 \quad (2)$$

$$PF_5 + H_2O_{(trace)} \rightarrow OPF_3 + 2HF \quad (3)$$

Contrary to the uncoated electrode, the ALD coated cycled electrode has an increase in NaF throughout prolonged cycling, exhibited in both Figure 7.13 (a) and Figure 7.15. NaF on its own is a highly resistive material and it can be assumed that this would hinder the CEI; however, Figure 7.7 and Table 7.1 indicates otherwise. As salt decomposes, it is likely that we are not generating a consistent NaF film, but rather discrete crystallites that allows for Na-ions to pass as seen in the case of LIB.[208,213] At 4.1V we begin to see the decomposition of the salt (Figure 7.13 (b)), which is largely dominated by $Na_xPF_yO_z$ moieties generated when sodium continues to react with the OPF products in scheme 3. Little Na_xPF_6 is found when the electrodes are charged to 4.1 and 4.5V; however, it was observed that the amount of Na_xPF_6 increases when the electrodes are cycled both 5 and 100 times. This is largely seen in the uncoated electrode which maybe one of the factors that increases the impedance of the electrode surface, as seen in Figure 7.7. The CEI generated from the coated electrodes is more inorganic causing the electrolyte decomposition functionalities to shift to a higher binding energy. Moreover, it

is widely accepted that coating cathode materials for LIBs improves the stability of the electrode-electrolyte interface. In our case, it is likely that the Al_2O_3 ALD coating tends to enhance the interface by protecting the electrode from HF formation (scheme 3).[214] Therefore, the electrode is less likely to form less unwanted byproducts as a result, boosting the coulombic efficiency.

7.4. Conclusion

The comparison of a P2-$Na_{2/3}Ni_{1/3}Mn_{2/3}O_2$ electrode and Al_2O_3 ALD coated P2-$Na_{2/3}Ni_{1/3}Mn_{2/3}O_2$electrode was presented. The ALD coating drastically improved the initial and overall coulombic efficiency and cathode resistivity. The cathode electrolyte interphase was investigated by XPS, which determined that each electrode generated a different surface film. The uncoated electrode contained more organic species such as carbonates, esters, and alkoxyl functionalities, retained more residual salt, and formed less NaF. Conversely, the coated electrode forms large CO moieties that are associated with polymeric species such as polyethylene oxide, which play a critical factor in forming a more flexible CEI that can reduce the exfoliation of the P2-NaNiMnO particle (Figure 7.9). Furthermore, the coated electrode forms more NaF throughout cycling, which plays a vital role in the overall CEI. The CEI generated on the coated P2-NaNiMnO electrode enhances the Na-ion kinetics from the bulk of the material through the electrode film versus the uncoated electrode. We demonstrated that optimizing the P2- NaNiMnO surface is a vital parameter in improving the electrode electrolyte interface which facilitates the cycling performance of this class of materials.

Chapter 7, in full, is currently being prepared for submission for publication of the material “Improvement of the Cathode Electrolyte Interphase on P2-$Na_{2/3}Ni_{1/3}Mn_{2/3}O_2$ by Atomic Layer Deposition”. The dissertation author was the co-primary investigator and author of this paper. The author conducted aluminum oxide ALD coating characterization and electrochemical test.

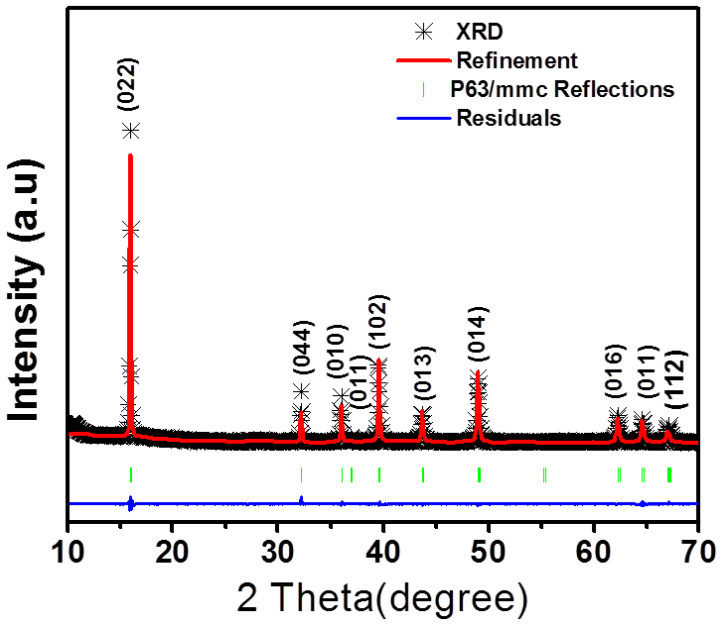

Lattice parameters: a=b=2.8878, c=11.1595 Rwp: 2.37 Rp: 6.07

Figure 7.1. XRD refinement results for the as-synthesized P2-$Na_{2/3}Ni_{1/3}Mn_{2/3}O_2$ (P2-NaNiMnO) cathode.

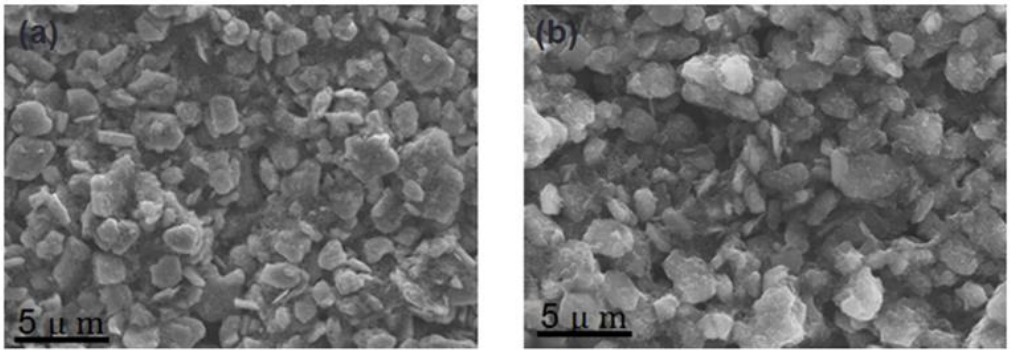

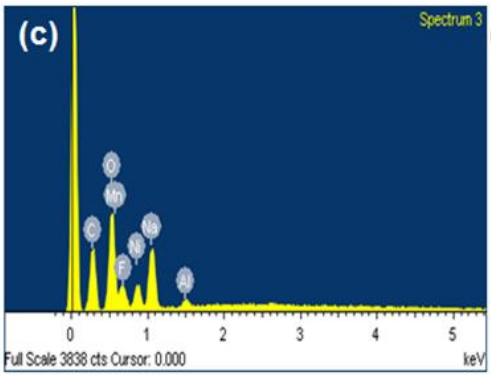

(d)

Element	Weight%	Atomic%
C	24.86	42.94
O	19.40	25.16
F	8.85	9.66
Na	8.83	7.97
Al	**0.56**	**0.43**
Mn	24.77	9.35
Ni	12.73	4.50
Totals	100.00	

Figure 7.2. (a) SEM image of ALD coated P2-NaNiMnO particle, and (b) SEM image coated P2-NaNiMnO electrode without conductive additive demonstrating the ALD coating thickness effectively. (c) (d) EDX results of the percentage of different elements.

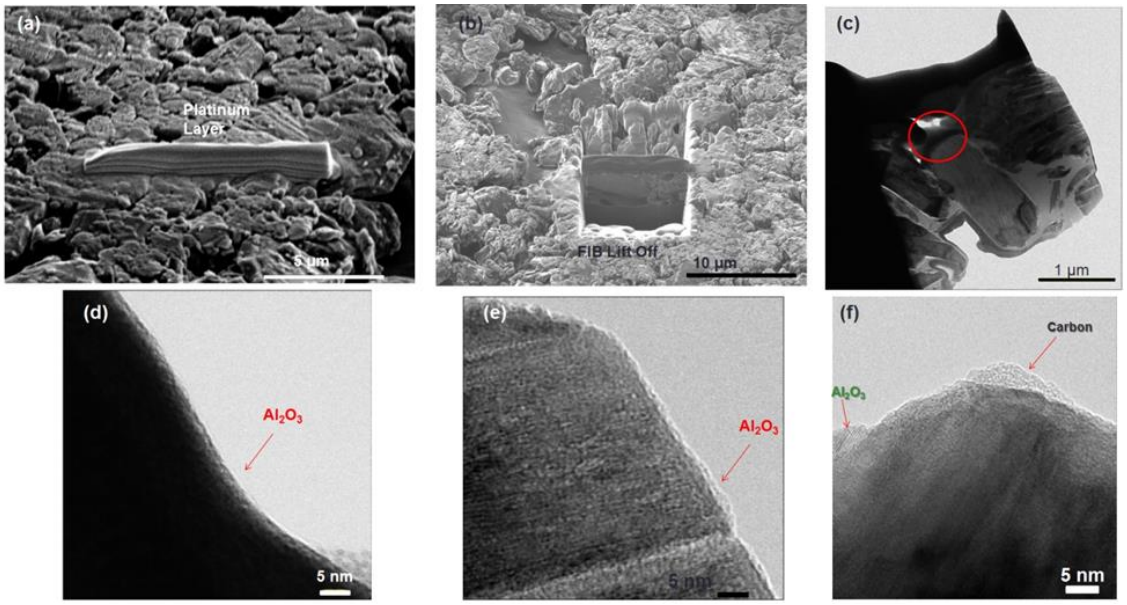

Figure 7.3. Preparation of electrode by Focused Ion Beam(FIB) (a)Platinum protecting layer deposited on P2-NaNiMnO electrode, (b) After Milling, (c) TEM picture of sample on Omni Probe, the red circle indicates where the TEM image are taken. (d) Dark field TEM image and (e) birght field TEM image of electrode. Image (f) demonstrates the TEM image without FIB preparation.

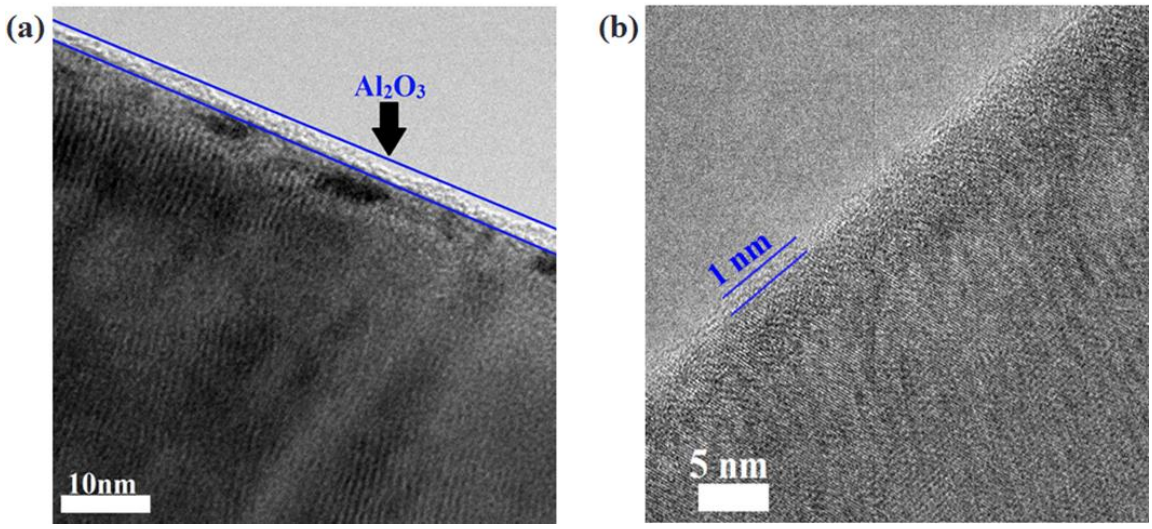

Figure 7.4. TEM images of the uncycled Al_2O_3 ALD coated $Na_{2/3}Ni_{1/3}Mn_{2/3}O_2$ composite electrode. (a) Low magnification image of coated pristine particle and (b) high magnification image determining the coating thickness of approximately 1 nm.

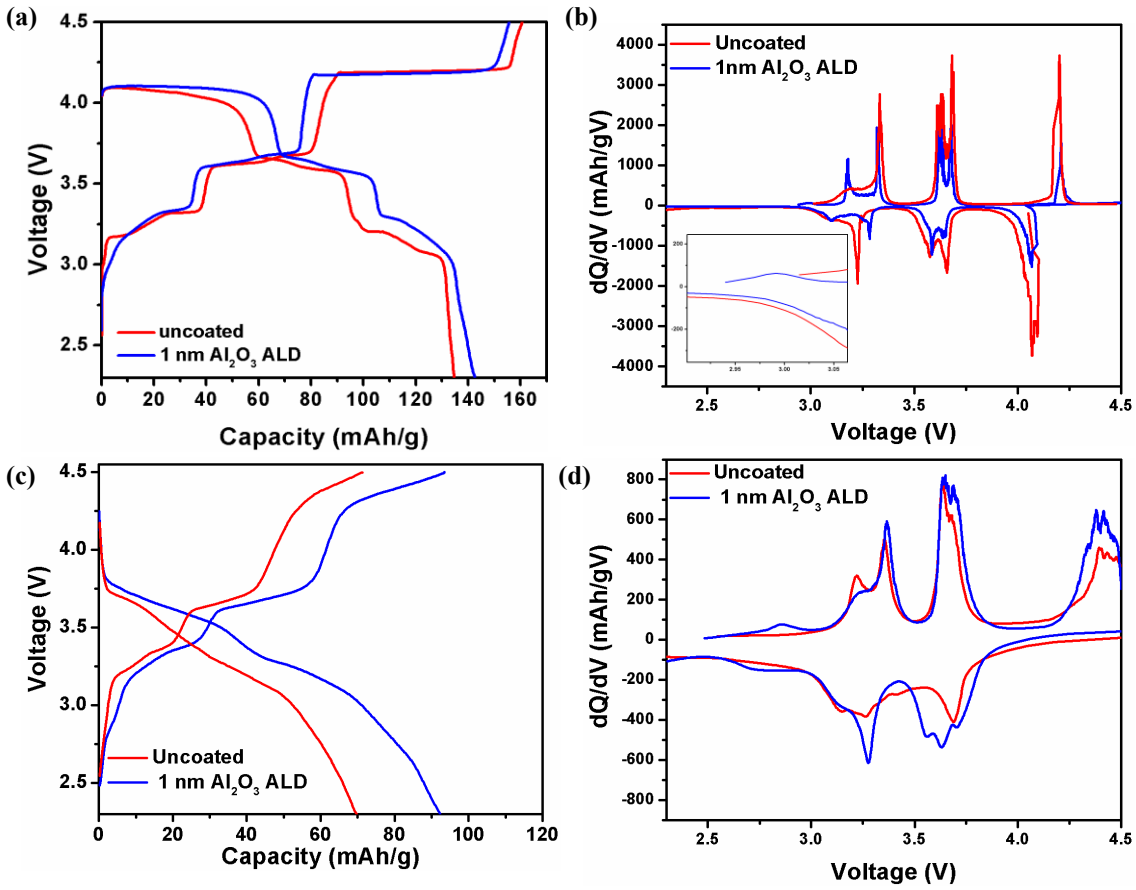

Figure 7.5. Voltage profiles and their corresponding differential voltage plots of uncoated and Al_2O_3 ALD coated electrodes at the (a, c) first cycle and (b, d) fiftieth cycle.

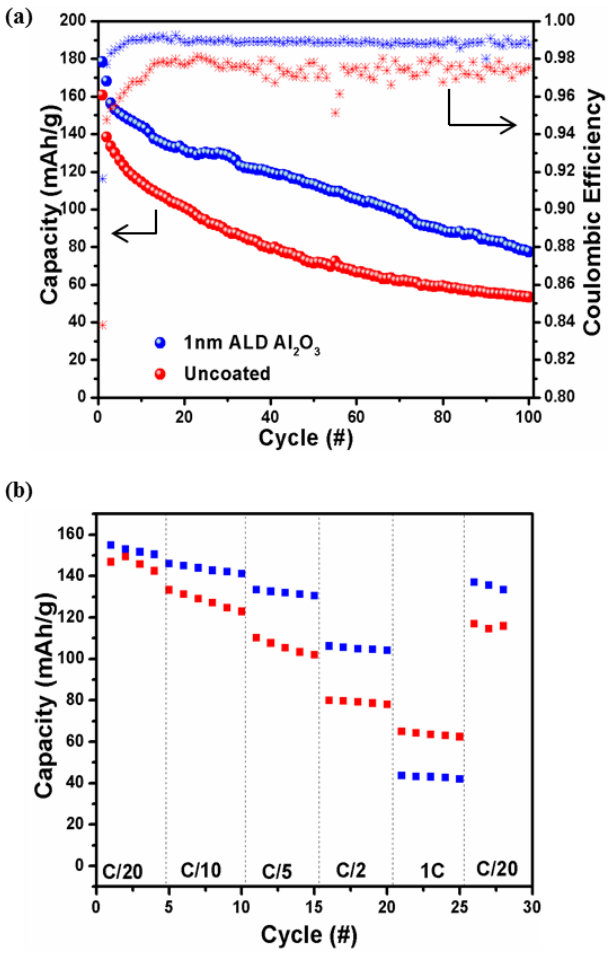

Figure 7.6. Galvanostatically cycled electrodes demonstrating (a)specific capacity versus cycle at C/20 rate and coulombic efficiency as a function of cycle number, and (b) rate capability plot for Al_2O_3 coated (blue) and uncoated (red).

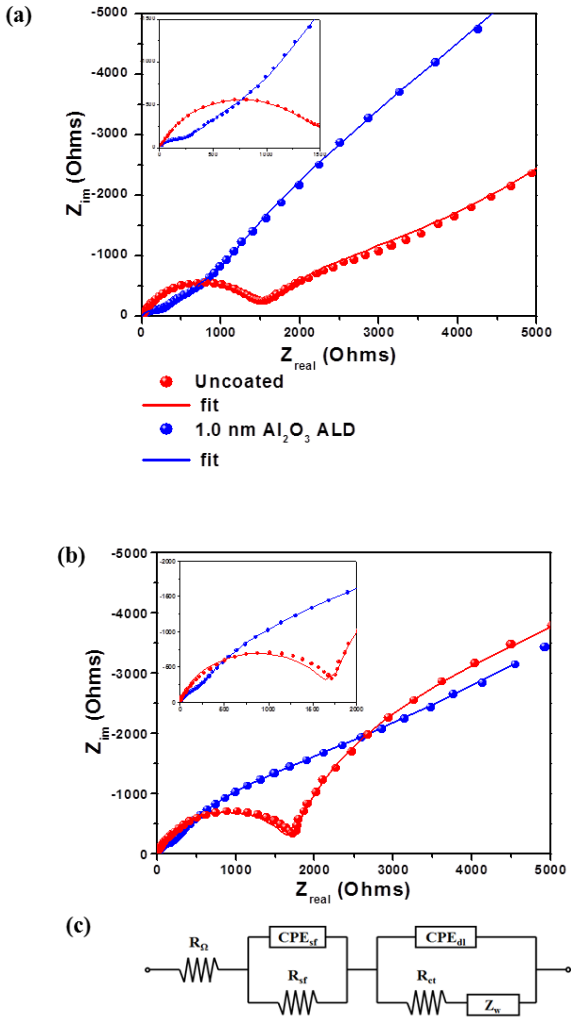

Figure 7.7. Nyquist plots of uncoated P2-NaNiMnO cycled electrodes (red) and Al_2O_3 coated cycled electrodes (blue) and uncoated (blue), at the (a) first cycle and (b) 100^{th} cycle. The data was fit based on the circuit shown in (c).

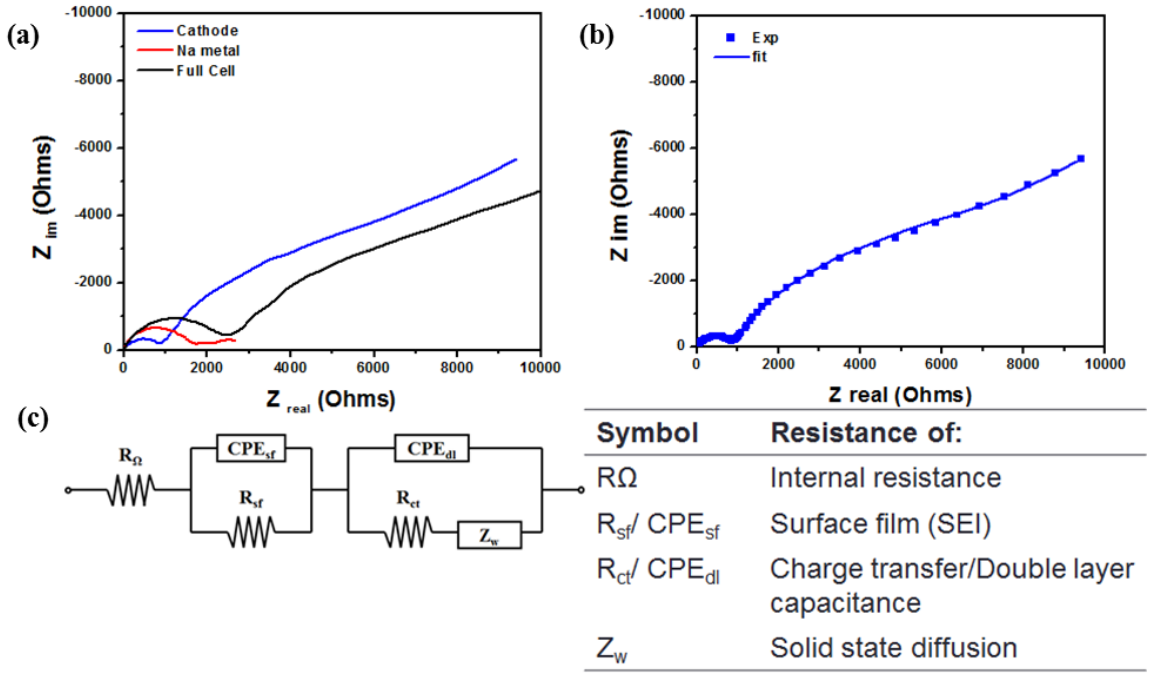

Symbol	Resistance of:
RΩ	Internal resistance
R_{sf}/ CPE_{sf}	Surface film (SEI)
R_{ct}/ CPE_{dl}	Charge transfer/Double layer capacitance
Z_w	Solid state diffusion

Figure 7.8. (a) EIS of the uncycled first cycle Nyquist plot of the full cell, cathode, Na metal. (b) Fitted Nyquist plot of the cathode using the equivalent circuit in (c). Equivalent circuit and table describes the symbol of the equivalent circuit.

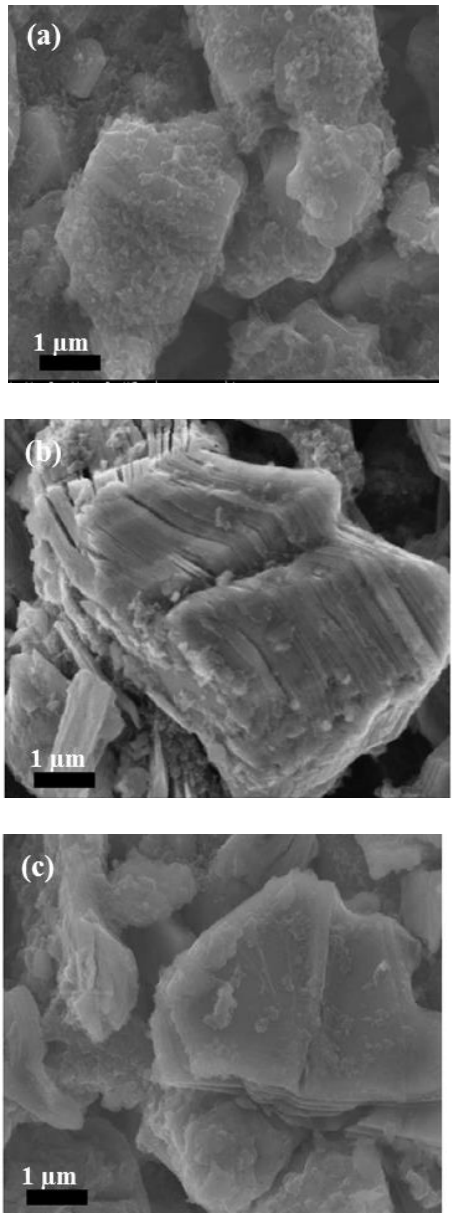

Figure 7.9. SEM images of (a) pristine uncoated and uncycled $Na_{2/3}Ni_{1/3}Mn_{2/3}O_2$ electrode, cycled electrodes after 100 cycles (b) uncoated and (c) Al_2O_3 ALD coated electrodes.

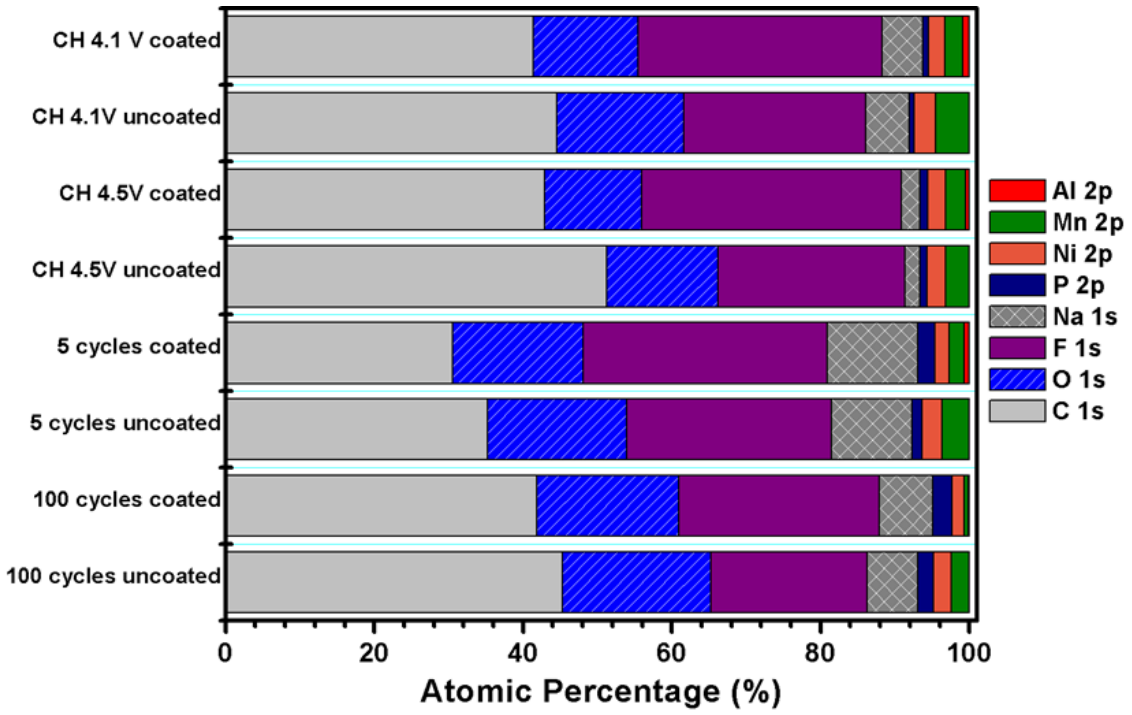

Figure 7.10. Elemental atomic percentage of the uncoated and ALD coated cycled electrodes at first charge 4.1V, 4.5V, 5 cycles, and 100 cycles.

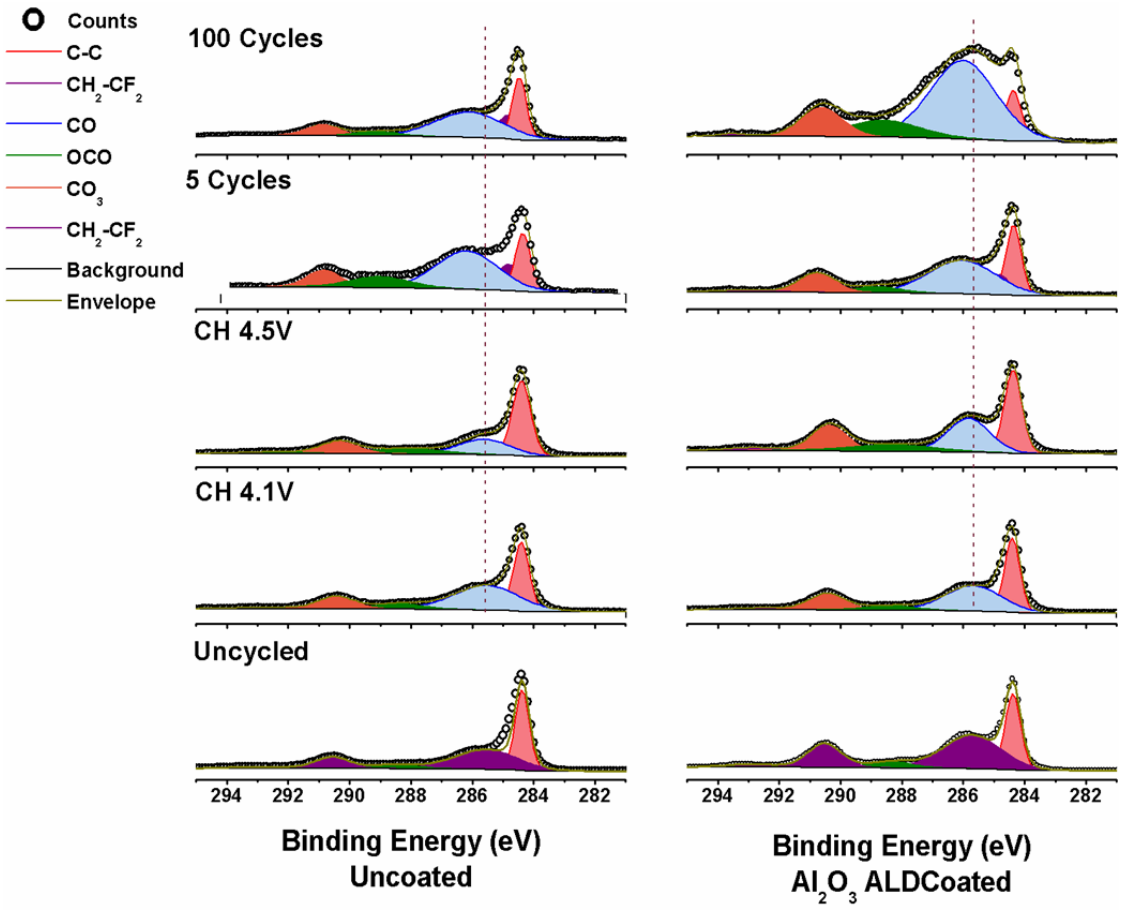

Figure 7.11. XPS C 1s regions of uncoated P2-NaNiMnO (left) and ALD Al_2O_3 coated (right) electrodes cycled to first charge 4.1V, 4.5V, 5 cycles, and 100 cycles.

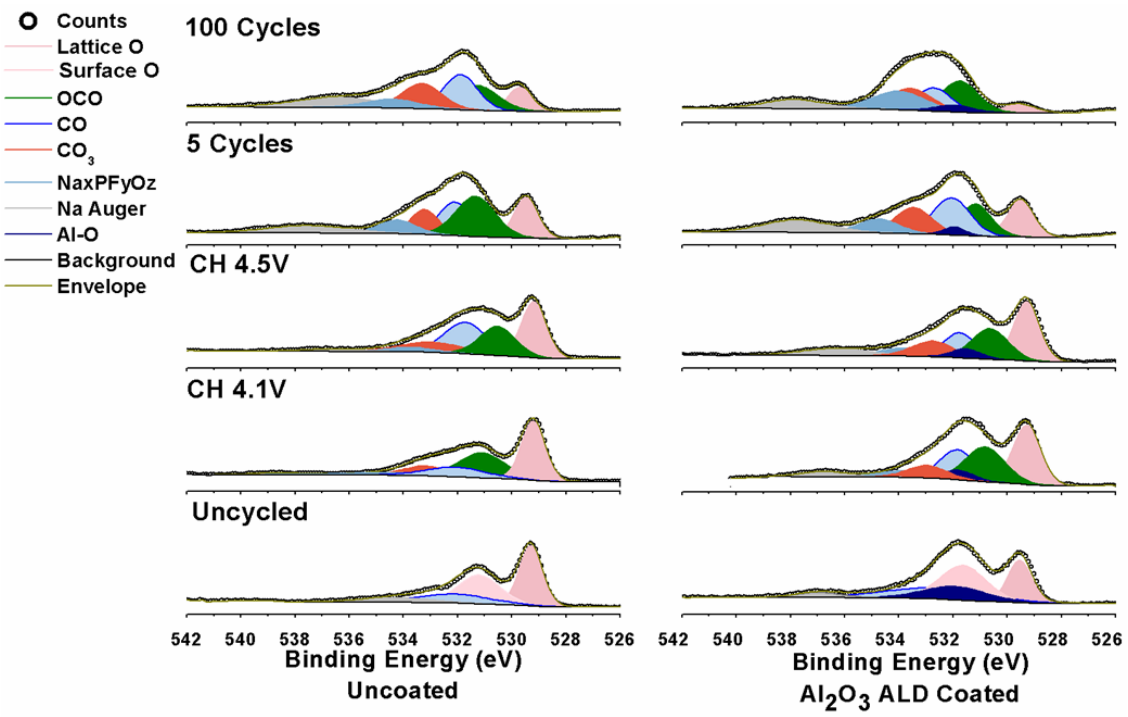

Figure 7.12. XPS O 1s regions of uncoated P2-NaNiMnO (left) and ALD Al_2O_3 coated (right) electrodes cycled.

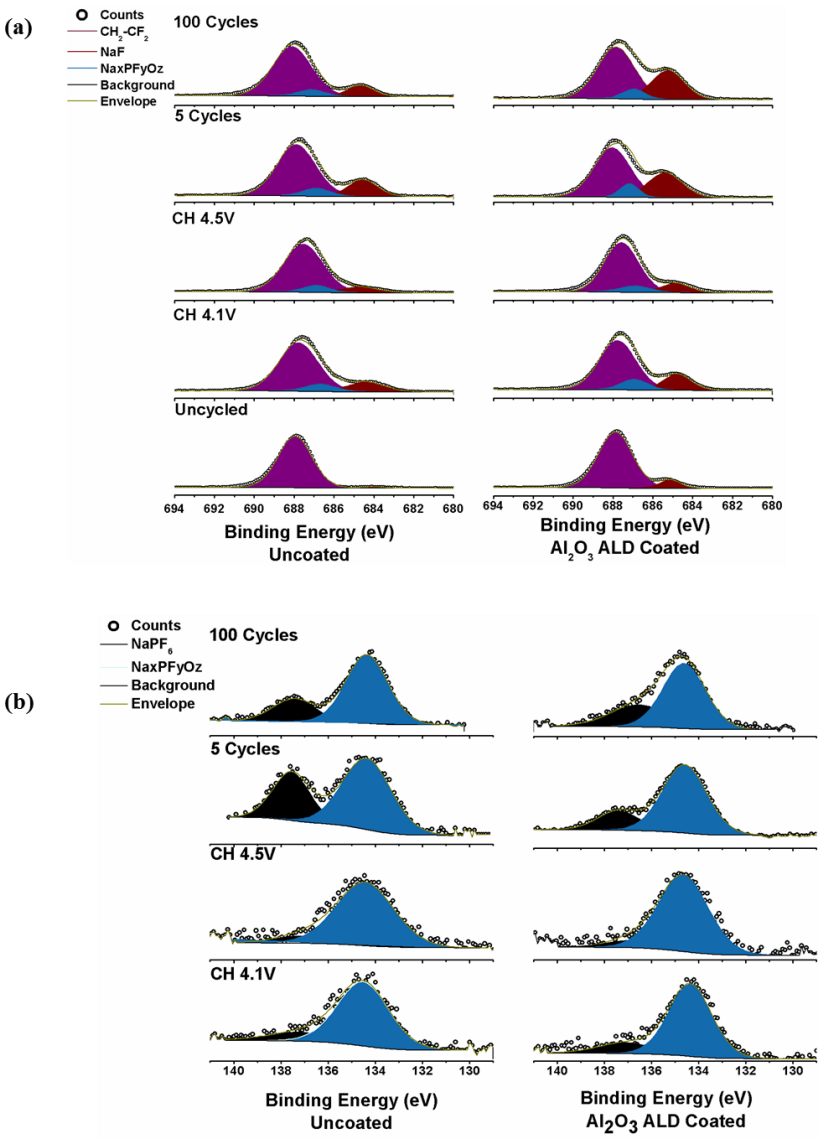

Figure 7.13. (a) XPS F 1s regions of uncoated P2-NaNiMnO (left) and ALD Al_2O_3 coated (right) electrodes cycled and (b) XPS P 2p region of ALD Al_2O_3 coated at to first charge 4.1V, 4.5V, 5 cycles, and 100 cycles.

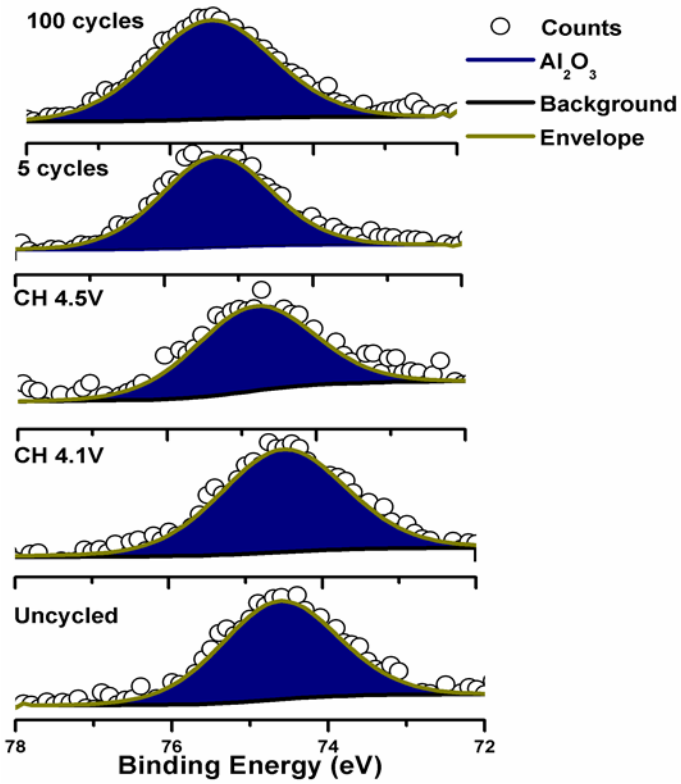

Figure 7.14. Elemental atomic percentage of the uncoated and ALD coated cycled electrodes at first charge 4.1V, 4.5V, 5 cycles, and 100 cycles.

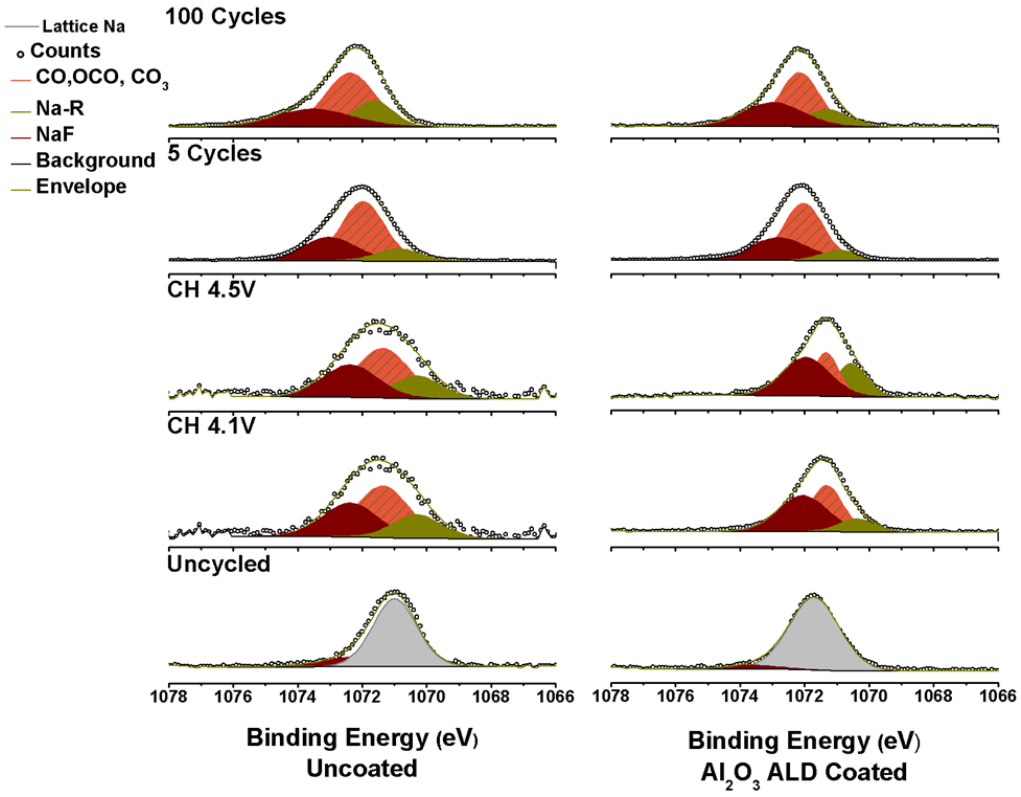

Figure 7.15. XPS Na 1s regions of uncoated P2-NaNiMnO (left) and ALD Al_2O_3 coated (right) electrodes cycled to first charge 4.1V, 4.5V, 5 cycles, and 100 cycles.

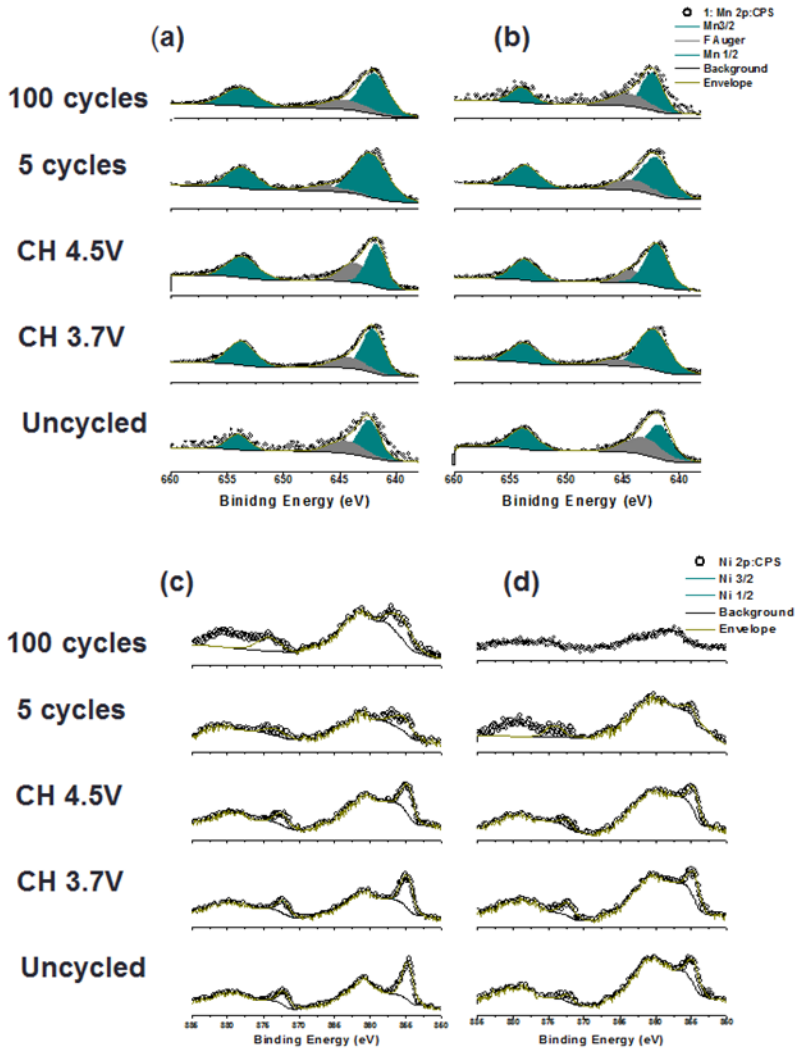

Figure 7.16. Nickel 2p region scan and fits of (a) uncoated P2_NaNiMnO and (b) ALD Al_2O_3 coated P2-NaNiMnO. Manganese 2p region scan and fits (c) uncoated and (d) coated electrode.

Table 7.1. Impedance measurement values for coated and uncoated cycled electrodes.

Symbol	**Uncoated first cycle**	**100 cycles uncoated**	**1.0 nm Al_2O_3 first cycle**	**1.0 nm Al_2O_3 100 cycles**
R_Ω	3.5332	1.3676	8.701	1.414
R_{sf}	878.8	1723	182	230.5
R_{ct}	3948	5043	420	1300

Chapter 8. Summary and Future Work

NIBs have gained massive attention due to the low cost of sodium resources, earth abundance, and similar chemical properties to its lithium counterpart. However, much larger ionic radius of Na-ions causes issues when finding optimum hosts for them. As a result, both cathode and anode materials should be better designed and optimized. The focus of my thesis is to explore novel electrode materials for Na-ion batteries and understand their physical/chemical properties with advanced characterization tools.

On the anode side, I have probed $Na_2Ti_3O_7$ as an anode for Na-ion batteries for a comprehensive understanding. The electrochemical performance is significantly enhanced with carbon coating, as a result of increased electronic conductivity and reduced solid electrolyte interphase formation. Ti^{4+} reduction upon discharge is demonstrated by *in situ* XAS. The self-relaxation behavior of the fully intercalated phase is explained for the first time due to its structural instability. These findings unravel the underlying relation between unique properties and battery performance of $Na_2Ti_3O_7$ anode, which should ultimately shed light on possible strategies for future improvement.

Moreover, I have investigated the tin sulfide–reduced graphene oxide (SnS_2-rGO) composite material as an advanced anode material for Na-ion batteries. It can deliver a reversible capacity of 630 mAh g^{-1} with negligible capacity loss and exhibits superb rate performance. The energy storage mechanism of this SnS_2-rGO anode and the critical mechanistic role of rGO are presented in detail. A synergistic mechanism involving conversion and alloying reactions is proposed based on SXRD and *in situ* XAS results. Contrary to what has been proposed in the literature, we determined that Na_2S_2

instead of Na_2S forms at the fully discharge state. The as-formed Na_2S_2 works as a matrix to relieve the strain from the huge volume expansion of the Na-Sn alloy reaction, shown in the high resolution transmission electron microscope. In addition, the Raman spectra results suggest that the rGO not only assists the material to have better electrochemical performance by preventing particle agglomeration of the active material, but also coordinates with Na-ions through electrostatic interaction during the first cycle. The unique reaction mechanism in SnS_2-rGO offers a well-balanced approach for sodium storage to deliver high capacity, long-cycle life, and superior rate capability.

On the cathode side, I have introduced a novel layered oxide material, $Na_{0.78}Ni_{0.23}Mn_{0.69}O_2$. This new compound provides a high reversible capacity of 138 mAh g^{-1} and an average potential of 3.25 V vs. Na^+/Na with a single smooth voltage profile. Its remarkable rate and cycling performance are attributed to the elimination of the P2-O2 phase transition upon cycling to 4.5 V. The first charge process yields an abnormally excess capacity which has yet to be observed in other P2 layered oxides. Metal K-edge XANES results show that the major charge compensation at the metal site during Na-ion deintercalation is achieved via the oxidation of nickel ions, whereas manganese ions remain in their Mn^{4+} state to a large extent. Interestingly, EELS and sXAS results show differences in electronic structures in the bulk and on the surface of electrochemically-cycled particles. On the surface, transition metal ions are in a lower valence state than in the bulk and the O K-edge pre-peak disappears. Based on previous reports on related Li-excess LIB cathodes, it is proposed that part of the charge compensation mechanism during the first cycle takes place at the lattice oxygen site, resulting in a surface to bulk transition metal gradient. We believe that by optimizing and

controlling oxygen activity, Na layered oxide materials with higher capacities can be designed.

In addition, surface modification and optimization are explored to enhance the electrochemical performance of the layered oxide cathode material. Atomic layer deposition is a commonly used coating technique for lithium ion battery electrodes. Recently, it has been applied to sodium ion battery anode materials. ALD is known to improve the cycling performance, coulombic efficiency of batteries, and maintain electrode integrity. The electrochemical performance of uncoated P2-$Na_{2/3}Ni_{1/3}Mn_{2/3}O_2$ electrodes is compared to ALD coated Al_2O_3 P2-$Na_{2/3}Ni_{1/3}Mn_{2/3}O_2$ electrodes. Given that ALD coatings are in the early stage of development for NIB cathode materials, little is known on how ALD coatings, in particular Al_2O_3, affect the electrode-electrolyte interface. Therefore, full characterizations of its effects are presented in this work. For the first time, XPS is used to elucidate the cathode electrolyte interphase on ALD coated electrodes. It contains less carbonate species and more inorganic species, which allows fast Na kinetics, resulting in a significant increase in coulombic efficiency and a decrease in cathode impedance. The effectiveness of Al_2O_3 ALD coating is also greatly reflected in the enhanced mechanical stability of the particle that prevents particle exfoliation.

Materials science emphasizes the study of the structure of materials and processing-structure-property relations in materials. To understand how the desired properties of a material can be modified, it is necessary to understand the relationship between a structure and properties. Moreover, how the structure can be changed and controlled by the various chemical, thermal, and mechanical, which a material is subjected during synthesis and use. This knowledge is still lacking in terms of the surface

modification and defect behavior for Na-ion cathode materials, which have generated tremendous interest in the recent five years for energy related research areas. Therefore, for the future work, I propose the functional oxides for NIBs to study mainly from two aspects.

The first part should focus on the surface modification of the ceramic materials for NIBs. Various types of surface modification including carbon coating, metal layer deposition coating, to just name a few should be conducted on existing oxide materials. Although similar studies have been widely reported in the lithium ion battery field, still very few studies have been conducted on NIBs so far. Given the intrinsic difference of Na-ion to Li-ion, the surface chemistry and kinetics will be significantly different. Surface characterization techniques including XPS, HRTEM, and STEM/EELS will be applied to investigate the changes of surface structure and chemistry on electrochemical performance.

In the second part, a system of $Na_wM_xM'_yM''_zO_2$ ($x+y+z \leq 1$) compounds should be synthesized and examined with the assistance of FP calculation. M, M' and M'' represent possible candidates of doping elements that mainly consist of TMs and some group IA, IIA, IIIA metal elements. Among them, the earth abundant and environmentally benign elements (Fe, Mn, Al, etc.) will be of particular interest. The effect of TM ordering, charging, and ordering on Na^+/vacancy ordering should be investigated in these compounds since they largely affect the Na-ion storage and transport capabilities. A systematic study of NawMxM'yM''zO2 compounds is important to obtain a universal principle of material design and engineering. Although the relationship between Na^+ and vacancy has been heavily discussed, the investigation of vacancy in

transition metal layer is seldom mentioned in NIBs studies. Thus, it is also worthwhile to bring in the concept of defect engineering in this group of $Na_wM_xM'_yM''_zO_2$ compounds.

Besides electrode materials, the investigation on the electrolyte should not be overlooked, because properties of electrolytes, especially the electrolyte-electrode-interface, are the essential for the proper function of any battery technologies. In any one of the battery systems, a good electrolyte should provide: (i) good ionic conductivity, (ii) a large voltage window (i.e., high and low onset potential for electrolyte decomposition through oxidation and reduction at high and low voltages, respectively), (iii) a large thermal stability window (i.e. melting point and boiling point lower and higher than the standard temperatures for the battery utilization, respectively), and (iv) no side reactions with other battery components. Finally, it should have as low toxicity as possible and meet cost requirements for the targeted applications. All these features are intrinsically dependent on the nature of the salt and the solvent(s) and the possible use of additives. Solid state electrolyte could be an excellent candidate to examine as well, but the interface issue can be the bottleneck of an all-solid-state battery.

References

(1) Tarascon, J.-M.; Armand, M. *Nature* **2001**, *414* (6861), 359.

(2) Ellis, B. L.; Nazar, L. F. *Curr. Opin. Solid State Mater. Sci.* **2012**, *16* (4), 168.

(3) Risacher, F.; Fritz, B. *Aquat. Geochemistry* **2009**, *15* (1–2), 123.

(4) Hong, S. Y.; Kim, Y.; Park, Y.; Choi, A.; Choi, N.-S.; Lee, K. T. *Energy Environ. Sci.* **2013**, *6* (7), 2067.

(5) Delmas, C.; Fouassier, C.; Hagenmuller, P. *Phys. B+C* **1980**, *99* (1–4), 81.

(6) Whittingham, M. S. *Chemistry of intercalation compounds: Metal guests in chalcogenide hosts*; 1978; Vol. 12.

(7) Stevens, D. a.; Dahn, J. R. *J. Electrochem. Soc.* **2000**, *147* (4), 1271.

(8) Stevens, D. A.; Dahn, J. R. *Journal of The Electrochemical Society*. 2001, p A803.

(9) Komaba, S.; Murata, W.; Ishikawa, T.; Yabuuchi, N.; Ozeki, T.; Nakayama, T.; Ogata, A.; Gotoh, K.; Fujiwara, K. *Adv. Funct. Mater.* **2011**, *21* (20), 3859.

(10) Wen, Y.; He, K.; Zhu, Y.; Han, F.; Xu, Y.; Matsuda, I.; Ishii, Y.; Cumings, J.; Wang, C. *Nat. Commun.* **2014**, *5* (May), 1.

(11) Park, S. Il; Gocheva, I.; Okada, S.; Yamaki, J. *J. Electrochem. Soc.* **2011**, *158* (10), A1067.

(12) Kim, H.; Hong, J.; Park, K. Y.; Kim, H.; Kim, S. W.; Kang, K. *Chem. Rev.* **2014**, *114* (23), 11788.

(13) Senguttuvan, P.; Palac ń, M. R. *Chem. Mater.* **2012**, 4109.

(14) Chevrier, V. L.; Ceder, G. *J. Electrochem. Soc.* **2011**, *158* (9), A1011.

(15) Komaba, S.; Matsuura, Y.; Ishikawa, T.; Yabuuchi, N.; Murata, W.; Kuze, S. *Electrochem. commun.* **2012**, *21* (1), 65.

(16) Wang, J. W.; Liu, X. H.; Mao, S. X.; Huang, J. Y. *Nano Lett.* **2012**, *12* (11), 5897.

(17) Du, Z.; Dunlap, R. A.; Obrovac, M. N. *J. Alloys Compd.* **2014**, *617*, 271.

(18) Darwiche, A.; Marino, C.; Sougrati, M. T.; Fraisse, B.; Stievano, L.; Monconduit, L. *J. Am. Chem. Soc.* **2012**, *134* (51), 20805.

(19) Qian, J.; Wu, X.; Cao, Y.; Ai, X.; Yang, H. *Angew. Chemie - Int. Ed.* **2013**, *52* (17), 4633.

(20) Ding, J. J.; Zhou, Y. N.; Sun, Q.; Yu, X. Q.; Yang, X. Q.; Fu, Z. W. *Electrochim. Acta* **2013**, *87*, 388.

(21) Rai, A. K.; Anh, L. T.; Gim, J.; Mathew, V.; Kim, J. *Ceram. Int.* **2014**, *40* (1 PART B), 2411.

(22) Billaud, J.; Clément, R. J.; Armstrong, a. R.; Canales-Vázquez, J.; Rozier, P.; Grey, C. P.; Bruce, P. G. *J. Am. Chem. Soc.* **2014**, *136* (49), 17243.

(23) Guo, S.; Yu, H.; Jian, Z.; Liu, P.; Zhu, Y.; Guo, X.; Chen, M.; Ishida, M.; Zhou, H. *ChemSusChem* **2014**, *7* (8), 2115.

(24) Su, D.; Wang, C.; Ahn, H. J.; Wang, G. *Chem. - A Eur. J.* **2013**, *19* (33), 10884.

(25) Ma, X.; Chen, H.; Ceder, G. *J. Electrochem. Soc.* **2011**, *158* (12), A1307.

(26) Zhao, J.; Zhao, L.; Dimov, N.; Okada, S.; Nishida, T. *J. Electrochem. Soc.* **2013**, *160* (5), A3077.

(27) Santamaria, J.; Tornero, J. D.; Menendez, N.; Blesa, M. C.; Moran, E.; Leon, C. *Solid State Ionics* **1999**, *126*, 81.

(28) Yabuuchi, N.; Yoshida, H.; Komaba, S. *Electrochemistry* **2012**, *80* (10), 716.

(29) Komaba, S.; Yabuuchi, N.; Nakayama, T.; Ogata, A.; Ishikawa, T.; Nakai, I. *Inorg. Chem.* **2012**, *51* (11), 6211.

(30) Yabuuchi, N.; Yano, M.; Yoshida, H.; Kuze, S.; Komaba, S. *J. Electrochem. Soc.* **2013**, *160* (5), A3131.

(31) Yuan, D. D.; Wang, Y. X.; Cao, Y. L.; Ai, X. P.; Yang, H. X. *ACS Appl. Mater. Interfaces* **2015**, *7* (16), 8585.

(32) Yabuuchi, N.; Kajiyama, M.; Iwatate, J.; Nishikawa, H.; Hitomi, S.; Okuyama, R.; Usui, R.; Yamada, Y.; Komaba, S. *Nat. Mater.* **2012**, *11* (6), 512.

(33) Pang, W. K.; Kalluri, S.; Peterson, V. K.; Sharma, N.; Kimpton, J.; Johannessen, B.; Liu, H. K.; Dou, S. X.; Guo, Z. *Chem. Mater.* **2015**, 150417143305004.

(34) Kim, D.; Kang, S. H.; Slater, M.; Rood, S.; Vaughey, J. T.; Karan, N.; Balasubramanian, M.; Johnson, C. S. *Adv. Energy Mater.* **2011**, *1* (3), 333.

(35) Xu, J.; Lee, D. H.; Clément, R. J.; Yu, X.; Leskes, M.; Pell, A. J.; Pintacuda, G.; Yang, X.-Q.; Grey, C. P.; Meng, Y. S. *Chem. Mater.* **2014**, *26* (2), 1260.

(36) Jian, Z.; Yu, H.; Zhou, H. *Electrochem. commun.* **2013**, *34*, 215.

(37) Kataoka, R.; Mukai, T.; Yoshizawa, A.; Sakai, T. *J. Electrochem. Soc.* **2013**, *160* (6), A933.

(38) Koleva, V.; Boyadzhieva, T.; Zhecheva, E.; Nihtianova, D.; Simova, S.; Tyuliev, G.; Stoyanova, R. *CrystEngComm* **2013**, *15* (44), 9080.

(39) Casas-Cabanas, M.; Roddatis, V. V.; Saurel, D.; Kubiak, P.; Carretero-Gonz âez, J.; Palomares, V.; Serras, P.; Rojo, T. *J. Mater. Chem.* **2012**, *22* (34), 17421.

(40) Oh, S. M.; Myung, S. T.; Hassoun, J.; Scrosati, B.; Sun, Y. K. *Electrochem. commun.* **2012**, *22* (1), 149.

(41) Jian, Z.; Yuan, C.; Han, W.; Lu, X.; Gu, L.; Xi, X.; Hu, Y.-S.; Li, H.; Chen, W.; Chen, D.; Ikuhara, Y.; Chen, L. *Adv. Funct. Mater.* **2014**, *24* (27), 4265.

(42) Plashnitsa, L. S.; Kobayashi, E.; Noguchi, Y.; Okada, S.; Yamaki, J. *J. Electrochem. Soc.* **2010**, *157* (4), A536.

(43) Wang, Q.; Zhao, B.; Zhang, S.; Gao, X.; Deng, C. *J. Mater. Chem. A* **2015**, *3* (15), 7732.

(44) Shen, W.; Wang, C.; Liu, H.; Yang, W. *Chem. - A Eur. J.* **2013**, *19* (43), 14712.

(45) Yang, J.; Han, D.-W.; Jo, M. R.; Song, K.; Kim, Y.-I.; Chou, S.-L.; Liu, H.-K.; Kang, Y.-M. *J. Mater. Chem. A* **2014**, *3* (3), 1005.

(46) Kang, J.; Baek, S.; Mathew, V.; Gim, J.; Song, J.; Park, H.; Chae, E.; Rai, A. K.; Kim, J. *J. Mater. Chem.* **2012**, *22* (39), 20857.

(47) Li, S.; Dong, Y.; Xu, L.; Xu, X.; He, L.; Mai, L. *Adv. Mater.* **2014**, *26* (21), 3545.

(48) Aragon, M. J.; Lavela, P.; Ortiz, G. F.; Tirado, J. L. *J. Electrochem. Soc.* **2015**, *162* (2), A3077.

(49) Pan, H.; Hu, Y.-S.; Chen, L. *Energy Environ. Sci.* **2013**, *6* (8), 2338.

(50) Kim, H.; Kim, H.; Ding, Z.; Lee, M. H.; Lim, K.; Yoon, G.; Kang, K. *Adv. Energy Mater.* **2016**, *6* (19), 1600943.

(51) Yabuuchi, N.; Komaba, S. *Sci. Technol. Adv. Mater.* **2014**, *15* (4), 43501.

(52) Lin, F.; Nordlund, D.; Markus, I.; Weng, T.-C.; Xin, H. L.; Doeff, M. *Energy Environ. Sci.* **2014**, *7*, 3077.

(53) Yoon, W.-S.; Balasubramanian, M.; Chung, K. Y.; Yang, X.-Q.; McBreen, J.; Grey, C. P.; Fischer, D. A. *J. Am. Chem. Soc.* **2005**, *127* (1), 17479.

(54) Liu, X.; Wang, D.; Liu, G.; Srinivasan, V.; Liu, Z.; Hussain, Z.; Yang, W. *Nat. Commun.* **2013**, *4*, 2568.

(55) Tarascon, J.-M. *Philos. Trans. A. Math. Phys. Eng. Sci.* **2010**, *368* (1923), 3227.

(56) Ong, S. P.; Chevrier, V. L.; Hautier, G.; Jain, A.; Moore, C.; Kim, S.; Ma, X.; Ceder, G. *Energy Environ. Sci.* **2011**, *4* (9), 3680.

(57) Palomares, V.; Casas-Cabanas, M.; Castillo-Martínez, E.; Han, M. H.; Rojo, T. *Energy Environ. Sci.* **2013**, *6* (8), 2312.

(58) Valvo, M.; Lindgren, F.; Lafont, U.; Björefors, F.; Edström, K. *J. Power Sources* **2014**, *245*, 967.

(59) Xu, J.; Lee, D. a E. H. O. E.; Meng, Y. S. *Funct. Mater. Lett.* **2013**, *6* (1), 1330001.

(60) Palacín, M. R. *Chem. Soc. Rev.* **2009**, *38* (9), 2565.

(61) Kim, S.-W. W.; Seo, D.-H. H.; Ma, X.; Ceder, G.; Kang, K. *Adv. Energy Mater.* **2012**, *2* (7), 710.

(62) Slater, M. D.; Kim, D.; Lee, E.; Johnson, C. S. *Adv. Funct. Mater.* **2013**, *23* (8), 947.

(63) Ge, P.; Fouletier, M. *Solid State Ionics* **1988**, *28–30*, 1172.

(64) Stevens, D. A.; Dahn, J. R. *J. Electrochem. Soc.* **2000**, *147* (12), 4428.

(65) Alcántara, R.; Jiménez-Mateos, J. M.; Lavela, P.; Tirado, J. L. *Electrochem. commun.* **2001**, *3* (11), 639.

(66) Xu, Y.; Zhu, Y.; Liu, Y.; Wang, C. *Adv. Energy Mater.* **2013**, *3* (1), 128.

(67) Wu, L.; Hu, X.; Qian, J.; Pei, F.; Wu, F.; Mao, R.; Ai, X.; Yang, H.; Cao, Y. *J. Mater. Chem. A* **2013**, *1* (24), 7181.

(68) Wu, L.; Pei, F.; Mao, R.; Wu, F.; Wu, Y.; Qian, J.; Cao, Y.; Ai, X.; Yang, H. *Electrochim. Acta* **2013**, *87*, 41.

(69) Shimizu, M.; Usui, H.; Sakaguchi, H. *J. Power Sources* **2014**, *248*, 378.

(70) Didier, C.; Guignard, M.; Denage, C.; Szajwaj, O.; Ito, S.; Saadoune, I.; Darriet, J.; Delmas, C. *Electrochem. Solid-State Lett.* **2011**, *14* (5), A75.

(71) Ferg, E.; Gummow, R. J.; Kock, A. De. **1994**, *141* (11), 9.

(72) Ohzuku, T.; Ueda, A.; Yamamoto, N. *J. Electrochem. Soc.* **1995**, *142* (5), 1431.

(73) Shirpour, M.; Cabana, J.; Doeff, M. *Energy Environ. Sci.* **2013**, *6* (8), 2538.

(74) Xiong, H.; Slater, M. D.; Balasubramanian, M.; Johnson, C. S.; Rajh, T. *J. Phys. Chem. Lett.* **2011**, *2* (20), 2560.

(75) Rudola, A.; Saravanan, K.; Devaraj, S.; Gong, H.; Balaya, P. *Chem. Commun.* **2013**, *49* (67), 7451.

(76) Senguttuvan, P.; Rousse, G.; Arroyo Y De Dompablo, M. E.; Vezin, H.; Tarascon, J. M.; Palac ń, M. R. *J. Am. Chem. Soc.* **2013**, *135* (10), 3897.

(77) Rousse, G.; M. Elena Arroyo-de Dompablo; Premkumar Senguttuvan; Alexandre Ponrouch; Jean-Marie Tarascon; M. Rosa Palac ń. *Chem. Mater.* **2013**, *25* (24), 4946.

(78) Ravel, B.; Newville, M. *J. Synchrotron Radiat.* **2005**, *12* (4), 537.

(79) Kresse, G.; Joubert, D. *Phys. Rev. B* **1999**, *59* (3), 1758.

(80) Kresse, G.; Furthm üller, J. *Comput. Mater. Sci.* **1996**, *6* (1), 15.

(81) John P. Perdew; Kieron Burke; Wang, Y. *Phys. Rev. B* **1998**, *57* (23), 14999.

(82) Lee, S.; Cho, Y.; Song, H. K.; Lee, K. T.; Cho, J. *Angew. Chemie - Int. Ed.* **2012**, *51* (35), 8748.

(83) Aydinol, M.; Kohan, a.; Ceder, G.; Cho, K.; Joannopoulos, J. *Phys. Rev. B* **1997**, *56* (3), 1354.

(84) Ra, W.; Nakayama, M.; Cho, W.; Wakihara, M.; Uchimoto, Y. *Phys. Chem. Chem. Phys.* **2006**, *8*, 882.

(85) Shiro, Y.; Sato, F.; Suzuki, T.; Iizuka, T.; Matsushita, T.; Oyanagi, H. *J. Am. Chem. Soc.* **1990**, *112* (8), 2921.

(86) Venkateswarlu, M.; Chen, C. H.; Do, J. S.; Lin, C. W.; Chou, T. C.; Hwang, B. J. *J. Power Sources* **2005**, *146* (1–2), 204.

(87) Ra, W.; Nakayama, M.; Ikuta, H.; Uchimoto, Y.; Wakihara, M. *Appl. Phys. Lett.* **2004**, *84* (22), 4364.

(88) Fouassier, C.; Delmas, C.; Hagenmuller, P. *Materials Research Bulletin*. 1975, pp 443–449.

(89) Ohzuku, T. *Journal of The Electrochemical Society*. 1993, p 2490.

(90) Jache, B.; Adelhelm, P. *Angew. Chemie - Int. Ed.* **2014**, 10169.

(91) Ellis, L. D.; Hatchard, T. D.; Obrovac, M. N. *J. Electrochem. Soc.* **2012**, *159* (11), A1801.

(92) Xiao, L.; Cao, Y.; Xiao, J.; Wang, W.; Kovarik, L.; Nie, Z.; Liu, J. *Chem. Commun.* **2012**, *48* (27), 3321.

(93) Liu, Y.; Xu, Y.; Zhu, Y.; Culver, J. N.; Lundgren, C. a.; Xu, K.; Wang, C. *ACS Nano* **2013**, *7* (4), 3627.

(94) Su, D.; Ahn, H.-J.; Wang, G. *Chem. Commun. (Camb).* **2013**, *49* (30), 3131.

(95) Su, D.; Xie, X.; Wang, G. *Chem. - A Eur. J.* **2014**, *20* (11), 3192.

(96) Kim, Y. Y.; Kim, Y. Y.; Choi, A.; Woo, S.; Mok, D.; Choi, N. S.; Jung, Y. S.; Ryu, J. H.; Oh, S. M.; Lee, K. T. *Adv. Mater.* **2014**, *26* (24), 4139.

(97) Qian, J.; Xiong, Y.; Cao, Y.; Ai, X.; Yang, H. *Nano Lett.* **2014**, *14* (4), 1865.

(98) Qu, B.; Ma, C.; Ji, G.; Xu, C.; Xu, J.; Meng, Y. S.; Wang, T.; Lee, J. Y. *Adv. Mater.* **2014**, *26* (23), 3854.

(99) William S. Hummers, J.; Offeman, R. E. *J. Am. Chem. Soc* **1958**, *80*, 1339.

(100) Wu, Q.; Jiao, L.; Du, J.; Yang, J.; Guo, L.; Liu, Y.; Wang, Y.; Yuan, H. *J. Power Sources* **2013**, *239*, 89.

(101) Patterson, A. L. *Phys. Rev.* **1939**, *56* (10), 978.

(102) Seo, J. W.; Jang, J. T.; Park, S. W.; Kim, C.; Park, B.; Cheon, J. *Adv. Mater.* **2008**, *20* (22), 4269.

(103) Baker, H.; Okamoto, H. *ASM Int.* **1992**.

(104) Hu, M.; Jiang, Y.; Sun, W.; Wang, H.; Jin, C.; Yan, M. *ACS Appl. Mater. Interfaces* **2014**, *6* (21), 19449.

(105) Mansour, a N.; Mukerjee, S.; Yang, X. Q.; McBreen, J. *J. Synchrotron Radiat.* **1999**, *6* (Pt 3), 596.

(106) Baggetto, L.; Bridges, C. a.; Jumas, J.-C.; Mullins, D. R.; Carroll, K. J.; Meisner, R. a.; Crumlin, E. J.; Liu, X.; Yang, W.; Veith, G. M. *J. Mater. Chem. A* **2014**, *2* (44), 18959.

(107) Smith, A. J.; Meek, P. E.; Liang, W. Y. *J. Phys. Chem. C* **1977**, *1321* (10), 1321.

(108) Wang, C.; Tang, K.; Aa, Q. Y.; Qian, Y. *Chem. Phys. Lett.* **2002**, *357* (5–6), 371.

(109) Radovsky, G.; Popovitz-Biro, R.; Staiger, M.; Gartsman, K.; Thomsen, C.; Lorenz, T.; Seifert, G.; Tenne, R. *Angew. Chemie - Int. Ed.* **2011**, *50* (51), 12316.

(110) Mei, L.; Xu, C.; Yang, T.; Ma, J.; Chen, L.; Li, Q.; Wang, T. *J. Mater. Chem. A* **2013**, *1* (30), 8658.

(111) Luo, B.; Fang, Y.; Wang, B.; Zhou, J.; Song, H.; Zhi, L. *Energy & Environmental Science*. 2012, p 5226.

(112) Schwan, J.; Ulrich, S.; Batori, V.; Ehrhardt, H.; Silva, S. R. P. *J. Appl. Phys.* **1996**, *80* (1), 440.

(113) Wang, G.; Wang, B.; Wang, X.; Park, J.; Dou, S.; Ahn, H.; Kim, K. *Journal of Materials Chemistry*. 2009, p 8378.

(114) Armand, M.; Tarascon, J.-M. J.-M. *Nature* **2008**, *451* (7179), 652.

(115) Han, M. H.; Gonzalo, E.; Singh, G.; Rojo, T. *Energy Environ. Sci.* **2015**, *8* (1), 81.

(116) Maazaz, A.; Delmas, C.; Hagenmuller, P. *J. Incl. Phenom.* **1983**, *1* (1), 45.

(117) Komaba, S.; Takei, C.; Nakayama, T.; Ogata, A.; Yabuuchi, N. *Electrochem. commun.* **2010**, *12* (3), 355.

(118) Miyazaki, S.; Kikkawa, S.; Koizumi, M. *Synth. Met.* **1983**, *6* (C), 211.

(119) Lu, Z.; Dahn, J. R. *J. Electrochem. Soc.* **2001**, *148* (11), A1225.

(120) Kundu, D.; Talaie, E.; Duffort, V.; Nazar, L. F. *Angew Chem Int Ed Engl* **2015**, *54* (11), 3431.

(121) Hamani, D.; Ati, M.; Tarascon, J. M.; Rozier, P. *Electrochem. commun.* **2011**, *13* (9), 938.

(122) Parant, J. P.; Olazcuaga, R.; Devalette, M.; Fouassier, C.; Hagenmuller, P. *J. Solid State Chem.* **1971**, *3* (1), 1.

(123) Molenda, J.; Stoklosa, A. *Solid State Ionics* **1990**, *38* (1–2), 1.

(124) Yuan, D.; Hu, X.; Qian, J.; Pei, F.; Wu, F.; Mao, R.; Ai, X.; Yang, H.; Cao, Y. *Electrochim. Acta* **2014**, *116*, 300.

(125) Sathiya, M.; Hemalatha, K.; Ramesha, K.; Tarascon, J.-M.; Prakash, A. S. *Chem. Mater.* **2012**, *24*, 1846−1853.

(126) Billaud, J.; Clément, R. J.; Armstrong, A. R.; Canales-Vázquez, J.; Rozier, P.; Grey, C. P.; Bruce, P. G. *J. Am. Chem. Soc.* **2014**, *136* (49), 17243.

(127) Takeda, Y.; Akagi, J.; Edagawa, A.; Inagaki, M.; Naka, S. *Mater. Res. Bull.* **1980**, *15* (8), 1167.

(128) Kubota, K.; Yabuuchi, N.; Yoshida, H.; Dahbi, M.; Komaba, S. *MRS Bull.* **2014**, *39* (5), 416.

(129) Lee, D. H.; Xu, J.; Meng, Y. S. *Phys. Chem. Chem. Phys.* **2013**, *15* (9), 3304.

(130) Talaie, E.; Duffort, V.; Smith, H. L.; Fultz, B.; Nazar, L. F. *Energy Environ. Sci.* **2015**, *8* (8), 2512.

(131) Xiang, X.; Zhang, K.; Chen, J. *Adv. Mater.* **2015**, *27* (36), 5343.

(132) Hy, S.; Liu, H.; Qian, D.; Zhang, M.; Hwang, B. J.; Meng, Y. S. *Energy Environ. Sci.* **2016**, *2*, 1931.

(133) Sathiya, M.; Rousse, G.; Ramesha, K.; Laisa, C. P.; Vezin, H.; Sougrati, M. T.; Doublet, M.-L.; Foix, D.; Gonbeau, D.; Walker, W.; Prakash, A. S.; Ben Hassine, M.; Dupont, L.; Tarascon, J.-M. *Nat. Mater.* **2013**, *12* (9), 827.

(134) Ohzuku, T.; Nagayama, M.; Tsuji, K.; Ariyoshi, K. *J. Mater. Chem.* **2011**, *21* (27), 10179.

(135) Oishi, M.; Yogi, C.; Watanabe, I.; Ohta, T.; Orikasa, Y.; Uchimoto, Y.; Ogumi, Z. *J. Power Sources* **2015**, *276*, 89.

(136) Luo, K.; Roberts, M. R.; Hao, R.; Guerrini, N.; Pickup, D. M.; Liu, Y.-S.; Edström, K.; Guo, J.; Chadwick, A. V.; Duda, L. C.; Bruce, P. G. *Nat. Chem.* **2016**, *8*, 684.

(137) Seo, D.; Lee, J.; Urban, A.; Malik, R.; Kang, S.; Ceder, G. *Nat. Chem.* **2016**, *8*, 692.

(138) de la Llave, E.; Talaie, E.; Levi, E.; Nayak, P. K.; Dixit, M.; Rao, P. T.; Hartmann, P.; Chesneau, F.; Major, D. T.; Greenstein, M.; Aurbach, D.; Nazar, L. F. *Chem. Mater.* **2016**, *28* (24), 9064.

(139) Yabuuchi, N.; Hara, R.; Kajiyama, M.; Kubota, K.; Ishigaki, T.; Hoshikawa, A.; Komaba, S. *Adv. Energy Mater.* **2014**, *4* (13), 1301453.

(140) Yabuuchi, N.; Hara, R.; Kubota, K.; Paulsen, J.; Kumakura, S.; Komaba, S. *J. Mater. Chem. A* **2014**, *2* (40), 16851.

(141) Nanba, Y.; Iwao, T.; De Boisse, B. M.; Zhao, W.; Hosono, E.; Asakura, D.; Niwa, H.; Kiuchi, H.; Miyawaki, J.; Harada, Y.; Okubo, M.; Yamada, A. *Chem. Mater.* **2016**, *28* (4), 1058.

(142) Mccalla, E.; Rowe, A. W.; Camardese, J.; Dahn, J. R. *Chem. Mater.* **2013**, *25* (13), 2716.

(143) Wang, Z. L.; Yin, J. S.; Jiang, Y. D. *Micron* **2000**, *31* (5), 571.

(144) Ender, M.; Weber, A.; Ivers-Tiffée, E. *J. Electrochem. Soc.* **2012**, *159* (2), A128.

(145) Cho, H.-M.; Meng, Y. S. *J. Electrochem. Soc.* **2013**, *160* (9), A1482.

(146) Yu, H.; Wang, Y.; Asakura, D.; Hosono, E.; Zhang, T.; Zhou, H. *RSC Adv.* **2012**, *2* (23), 8797.

(147) Xu, B.; Fell, C. R.; Chi, M.; Meng, Y. S. *Energy Environ. Sci.* **2011**, *4* (6), 2223.

(148) Clément, R. J.; Xu, J.; Middlemiss, D. S.; Alvarado, J.; Ma, C.; Meng, Y. S.; Grey, C. P. *J. Mater. Chem. A* **2017**, *5*, 4129.

(149) Lu, Z.; Dahn, J. R. *Chem. Mater.* **2001**, *13* (4), 1252.

(150) Mendiboure, A.; Delmas, C.; Hagenmuller, P. *J. Solid State Chem.* **1985**, *57* (3), 323.

(151) Yabuuchi, N.; Yoshii, K.; Myung, S.-T.; Nakai, I.; Komaba, S. *J. Am. Chem. Soc.* **2011**, *133* (12), 4404.

(152) Yu, H.; Zhou, H. *J. Phys. Chem. Lett.* **2013**, *4* (8), 1268.

(153) Qian, D.; Xu, B.; Chi, M.; Meng, Y. S. *Phys. Chem. Chem. Phys.* **2014**, *16* (28), 14665.

(154) Carroll, K. J.; Qian, D.; Fell, C.; Calvin, S.; Veith, G. M.; Chi, M.; Baggetto, L.; Meng, Y. S. *Phys. Chem. Chem. Phys.* **2013**, *15*, 11128.

(155) Armstrong, A. R.; Holzapfel, M.; Novák, P.; Johnson, C. S.; Kang, S. H.; Thackeray, M. M.; Bruce, P. G. *J. Am. Chem. Soc.* **2006**, *128* (26), 8694.

(156) Soriano, L.; Gutiérrez, A.; Preda, I.; Palacín, S.; Sanz, J. M.; Abbate, M.; Trigo, J. F.; Vollmer, A.; Bressler, P. R. *Phys. Rev. B - Condens. Matter Mater. Phys.* **2006**, *74* (19), 3.

(157) Qiao, R.; Wray, L. A.; Kim, J. H.; Pieczonka, N. P. W.; Harris, S. J.; Yang, W. *J. Phys. Chem. C* **2015**, *119* (49), 27228.

(158) Jiang, M.; Key, B.; Meng, Y. S.; Grey, C. P. *Chem. Mater.* **2009**, *21* (13), 2733.

(159) Oishi, M.; Fujimoto, T.; Takanashi, Y.; Orikasa, Y.; Kawamura, A.; Ina, T.; Yamashige, H.; Takamatsu, D.; Sato, K.; Murayama, H.; Tanida, H.; Arai, H.; Ishii,

H.; Yogi, C.; Watanabe, I.; Ohta, T.; Mineshige, A.; Uchimoto, Y.; Ogumi, Z. *J. Power Sources* **2013**, *222*, 45.

(160) Hy, S.; Su, W.-N.; Chen, J.-M.; Hwang, B.-J. *J. Phys. Chem. C* **2012**, *116* (48), 25242.

(161) De Groot, F. M. F.; Grioni, M.; Fuggle, J. C.; Ghijsen, J.; Sawatzky, G. A.; Petersen, H. *Phys. Rev. B* **1989**, *40* (8), 5715.

(162) Qiao, R.; Chuang, Y. De; Yan, S.; Yang, W. *PLoS One* **2012**, *7* (11), 3.

(163) Ozawa, K. *Solid State Ionics* **1994**, *69* (3), 212.

(164) Dunn, B.; Kamath, H.; Tarascon, J.-M. *Science (80-.).* **2011**, *334* (Li), 928.

(165) Yabuuchi, N.; Kubota, K.; Dahbi, M.; Komaba, S. **2014**.

(166) Xu, J.; Liu, H.; Meng, Y. S. *Electrochem. commun.* **2015**, *60*, 13.

(167) Bucher, N.; Hartung, S.; Franklin, J. B.; Wise, A. M.; Lim, L. Y.; Chen, H.-Y.; Weker, J. N.; Toney, M. F.; Srinivasan, M. *Chem. Mater.* **2016**, *28* (7), 2041.

(168) Xu, J.; Ma, C.; Balasubramanian, M.; Meng, Y. S. *Chem. Commun.* **2014**, *50* (83), 12564.

(169) Lu, Y. C.; Ma, C.; Alvarado, J.; Kidera, T.; Dimov, N.; Meng, Y. S.; Okada, S. *J. Power Sources* **2015**, *284*, 287.

(170) Lu, Y. C. Y. C.; Ma, C.; Alvarado, J.; Dimov, N.; Meng, Y. S. Y. S.; Okada, S. *J. Mater. Chem. A* **2015**, *0* (33), 1.

(171) J. M. Paulsen; R. A. Donaberger, † and; Dahn*, J. R. **2000**.

(172) Lu, Z.; Dahn, J. R. *J. Electrochem. Soc.* **2001**, *148* (11), A1225.

(173) Cl ément, R. J.; Bruce, P. G.; Grey, C. P. *J. Electrochem. Soc.* **2015**, *162* (14), A2589.

(174) Wu, X.; Guo, J.; Wang, D.; Zhong, G.; McDonald, M. J.; Yang, Y. *J. Power Sources* **2015**, *281*, 18.

(175) Wu, X.; Xu, G.-L.; Zhong, G.; Gong, Z.; McDonald, M. J.; Zheng, S.; Fu, R.; Chen, Z.; Amine, K.; Yang, Y. *ACS Appl. Mater. Interfaces* **2016**, *8* (34), 22227.

(176) Xu, K. *Chem. Rev.* **2014**, *114* (23), 11503.

(177) George, S. M. *Chem. Rev.* **2010**, 111.

(178) Memarzadeh Lotfabad, E.; Kalisvaart, P.; Cui, K.; Kohandehghan, A.; Kupsta, M.; Olsen, B.; Mitlin, D. *Phys. Chem. Chem. Phys.* **2013**, *15* (32), 13646.

(179) Jung, Y. S.; Cavanagh, A. S.; Dillon, A. C.; Groner, M. D.; George, S. M.; Lee, S.-H. *J. Electrochem. Soc.* **2010**, *157* (1), A75.

(180) Cheng, H.-M.; Wang, F.-M.; Chu, J. P.; Santhanam, R.; Rick, J.; Lo, S.-C. *J. Phys. Chem. C* **2012**, *116*, 7629.

(181) Lee, J. H.; Hon, M. H.; Chung, Y. W.; Leu, I. C. *Appl. Phys. A Mater. Sci. Process.* **2011**, *102* (3), 545.

(182) Zhao, J.; Qu, G.; Flake, J. C.; Wang, Y. *Chem. Commun.* **2012**, *48* (65), 8108.

(183) Liu, J.; Li, X.; Cai, M.; Li, R.; Sun, X. *Electrochim. Acta* **2013**, *93*, 195.

(184) Li, C.; Zhang, H. P.; Fu, L. J.; Liu, H.; Wu, Y. P.; Rahm, E.; Holze, R.; Wu, H. Q. *Electrochim. Acta* **2006**, *51* (19), 3872.

(185) Zhao, L.; Zhao, J.; Hu, Y.-S.; Li, H.; Zhou, Z.; Armand, M.; Chen, L. *Adv. Energy Mater.* **2012**, *2* (8), 962.

(186) Han, X.; Liu, Y.; Jia, Z.; Chen, Y.-C.; Wan, J.; Weadock, N.; Gaskell, K. J.; Li, T.; Hu, L. *Nano Lett.* **2014**, *14* (1), 139.

(187) Kaliyappan, K.; Liu, J.; Lushington, A.; Li, R.; Sun, X. *ChemSusChem* **2015**, *3* (15), n/a.

(188) Liu, Y.; Fang, X.; Zhang, A.; Shen, C.; Liu, Q.; Enaya, H. A.; Zhou, C. *Nano Energy* **2016**, *27*, 27.

(189) Wang, S.; Sina, M.; Parikh, P.; Uekert, T.; Shahbazian, B.; Devaraj, A.; Meng, Y. S. *Nano Lett.* **2016**, *16* (9), 5594.

(190) Kim, S.; Park, M. J.; Balsara, N. P.; Liu, G.; Minor, A. M. *Ultramicroscopy* **2010**, *111*, 191.

(191) Malmgren, S.; Ciosek, K.; Hahlin, M.; Gustafsson, T.; Gorgoi, M.; Rensmo, H.; Edström, K. *Electrochim. Acta* **2013**, *97*, 23.

(192) Lu, Z.; Dahn, J. R. *J. Electrochem. Soc.* **2001**, *148* (11), A1225.

(193) Mueller, S.; Tuth, R.; Fischer, D.; Wille-Haussmann, B.; Wittwer, C. *Energy Technol.* **2014**, *2* (1), 83.

(194) Cho, H.-M.; Chen, M. V.; MacRae, A. C.; Meng, Y. S. *ACS Appl. Mater. Interfaces* **2015**, *7* (30), 16231.

(195) Kim, J. W.; Kim, D. H.; Oh, D. Y.; Lee, H.; Kim, J. H.; Lee, J. H.; Jung, Y. S. *J. Power Sources* **2015**, *274*, 1254.

(196) Su, Y.; Cui, S.; Zhuo, Z.; Yang, W.; Wang, X.; Pan, F. .

(197) Park, J. S.; Meng, X.; Elam, J. W.; Hao, S.; Wolverton, C.; Kim, C.; Cabana, J. *Chem. Mater.* **2014**, *26* (10), 3128.

(198) Wise, A. M.; Ban, C.; Weker, J. N.; Misra, S.; Cavanagh, A. S.; Wu, Z.; Li, Z.; Whittingham, M. S.; Xu, K.; George, S. M.; Toney, M. F. *Chem. Mater.* **2015**, *27* (17), 6146.

(199) Liu, J.; Manthiram, A. *Chem. Mater.* **2009**, *21* (7), 1695.

(200) Li, X.; Liu, J.; Meng, X.; Tang, Y.; Banis, M. N.; Yang, J.; Hu, Y.; Li, R.; Cai, M.; Sun, X. *J. Power Sources* **2014**, *247*, 57.

(201) Riley, L. A.; Van Atta, S.; Cavanagh, A. S.; Yan, Y.; George, S. M.; Liu, P.; Dillon, A. C.; Lee, S.-H. *J. Power Sources* **2011**, *196* (6), 3317.

(202) Jung, S. C.; Kim, H. J.; Choi, J. W.; Han, Y. K. *Nano Lett.* **2014**, *14* (11), 6559.

(203) Schroder, K.; Alvarado, J.; Yersak, T. A.; Li, J.; Dudney, N.; Webb, L. J.; Meng, Y. S.; Stevenson, K. J. *Chem. Mater.* **2015**, *27* (16), 5531.

(204) Chan, C. K.; Ruffo, R.; Hong, S. S.; Cui, Y. *J. Power Sources* **2009**, *189* (2), 1132.

(205) Lu, Z.; Dahn, J. R. *J. Electrochem. Soc.* **2001**, *148* (7), A710.

(206) Guan, C.; Wang, X.; Zhang, Q.; Fan, Z.; Zhang, H.; Fan, H. J. *Nano Lett.* **2014**, *14* (8), 4852.

(207) He, Y.; Yu, X.; Wang, Y.; Li, H.; Huang, X. *Adv. Mater.* **2011**, *23* (42), 4938.

(208) Verdier, S.; El Ouatani, L.; Dedryvère, R.; Bonhomme, F.; Biensan, P.; Gonbeau, D. *J. Electrochem. Soc.* **2007**, *154* (12), A1088.

(209) Fleutot, S.; Dupin, J.-C.; Renaudin, G.; Martinez, H. *Phys. Chem. Chem. Phys.* **2011**, *13* (39), 17564.

(210) Quinlan, R. A.; Lu, Y.-C.; Kwabi, D.; Shao-Horn, Y.; Mansour, A. N. *J. Electrochem. Soc.* **2016**, *163* (2), A300.

(211) Verde, M. G.; Liu, H.; Carroll, K. J.; Baggetto, L.; Veith, G. M.; Meng, Y. S. *ACS Appl. Mater. Interfaces* **2014**, *6* (21), 18868.

(212) Edström, K.; Gustafsson, T.; Thomas, J. O. *Electrochim. Acta* **2004**, *50* (2–3), 397.

(213) Andersson, A. M.; Edström, K. *J. Electrochem. Soc.* **2001**, *148* (10), A1100.

(214) Gauthier, M.; Carney, T. J.; Grimaud, A.; Giordano, L.; Pour, N.; Chang, H.-H.; Fenning, D. P.; Lux, S. F.; Paschos, O.; Bauer, C.; Maglia, F.; Lupart, S.; Lamp, P.; Shao-Horn, Y. *J. Phys. Chem. Lett.* **2015**, *6* (22), 4653.